Astronomy Reports, Vol. 48, No. 7, 2004, pp. 525–533. Translated from Astronomicheskiĭ Zhurnal, Vol. 81, No. 7, 2004, pp. 579–588.

Einstein–Rosen Bridges and the Characteristic Properties of Gravitational Lensing by Them

A. A. Shatskiĭ

Astro Space Center, Lebedev Physical Institute, Russian Academy of Sciences, Profsoyuznaya ul. 84/32, Moscow, 117810 Russia

Received November 5, 2003; in final form, January 9, 2004

Abstract—It is shown that Einstein–Rosen bridges (wormholes)—hypothetical objects that topologically connect separate locations in the Universe—can be static solutions of the Einstein equations. The corresponding equations for bridges are reduced to a form convenient for their analysis and numerical solution. The matter forming the bridge must have a sufficiently hard and anisotropic equation of state. Our results are compared with a previously known analytic solution for a bridge, which is a special case of the general solution in the framework of general relativity. The deflection of photons by the bridge (gravitational lensing) is studied. © *2004 MAIK "Nauka/Interperiodica"*.

1. INTRODUCTION

In recent years, there have been an increasing number of publications in relativistic astrophysics devoted to so-called "wormholes." Another term for these objects proposed by Einstein and Rosen [1] in 1935 is "bridge."

There are several different definitions of bridges, depending on the presence or absence of event horizons in them. A common feature of all these definitions is that the bridge connects two asymptotically flat spatial regions. The location of such a connection is the bridge, and its central part is called the bridge's throat (Fig. 1). Spacetime is strongly curved near the throat. We shall consider here only traversable Lorentzian wormholes, i.e., those through which physical bodies can pass. Consequently, there must be no event horizons in such bridges.

As was proved long ago [2], bridges can be constructed in general relativity only from matter with exotic equations of state (for more details, see below). Such matter has not been found in the Universe thus far. Therefore, bridge solutions were first sought in alternative theories of gravity, such as the Brans–Dicke theory and theories involving quantum-gravitational effects.

Despite all these problems, bridges have been attracting increasing interest. This is due, in our view, to the following four factors.

(1) The existence of dark matter, which may obey an unusual equation of state.

(2) Bridges could be real and observable astrophysical objects, such as black holes, whose existence was likewise long rejected by many scientists.

(3) Huge progress in computer modeling of multidimensional structures has made it possible to solve numerically many problems in relativistic astrophysics. Most of these problems cannot be solved using analytic methods because of their extreme complexity.

(4) There have been serious discussions of solutions of the equations of general relativity containing time loops, which imply the existence of time machines (see, for example, [3]).

We shall not discuss here speculations based on the fourth factor. Our aim is to present the basic ideas of the physics of bridges and their direct relationship to the theory of gravity and black-hole physics. The bridges will be considered in a general-relativistic treatment.

2. SPHERICALLY SYMMETRIC SYSTEMS

Analytic studies can be carried out most easily for spherically symmetric systems, for which all quantities depend only on time and radius. The form of the solutions of the equations of general relativity does not depend only on the symmetry of the system. Nevertheless, even in cases with the simplest central symmetry, exact solutions have been obtained for only a few cases. These are the case of dust matter (the pressure is equal to zero) and of the vacuum condensate (the pressure is the negative of the energy density). It is assumed in inflationary cosmological models that this latter equation of state was dominant for matter in the initial stage of development of the Universe after the Big Bang (a de Sitter universe) [4].

In more realistic cases, for example, when the pressure is proportional to the energy density with a

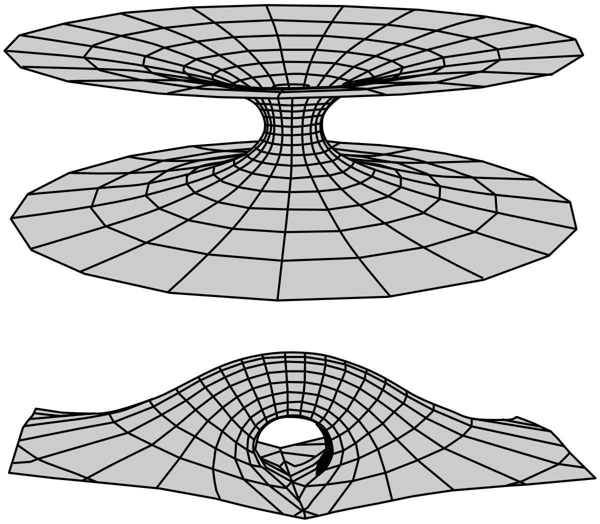

Fig. 1. Spherically symmetric bridge connecting two parts of the Universe (top panel) and a nonspherically symmetric "door-handle" bridge connecting two distant parts of the same Universe (bottom panel).

positive coefficient (in particular, an ideal photon gas is described by the equation of state with a coefficient of 1/3), we have no exact solutions, and only numerical solutions are available. Moreover, even for the simplest models in which all quantities depend only on radius, exact solutions have been found for only a few cases.

An illustrative example of static solutions are ordinary stars and planets. However, in reality, they obey a fairly sophisticated nonlinear equation of state. As a result, only numerical solutions can be obtained for these objects in a general-relativitistic treatment.

The spherically symmetric metric in general relativity can be written as

$$ds^2 = \exp(\nu)dt^2 - \exp(\lambda)dr^2 - r^2 d\Omega^2. \quad (1)$$

Here, $\nu = 2\phi$ is twice the red (or violet) shift; $\phi = (\Delta f)/f$; f is the photon frequency at infinity, near the source; and $d\Omega^2$ is an element of solid angle.

In the general case, the energy–momentum tensor in comoving matter with a spherically symmetric distribution has the form[1]

$$4\pi T_0^0 = \varepsilon, \quad 4\pi T_1^1 = -P_{||}, \quad (2)$$
$$4\pi T_2^2 = 4\pi T_3^3 = -P_\perp.$$

It is convenient to describe motion in the spherically symmetric field using the function V^2, which is the square of the invariant velocity of the particle with respect to the spheres $r =$ const:

$$V^2 = \left(\frac{dr}{dt}\right)^2 e^{\lambda-\nu}. \quad (3)$$

A more detailed definition of V^2 is presented in [5]. When a falling particle reaches an event horizon, the velocity V reaches unity. The corresponding element of the interval ds is zero, so that V^2 is an invariant at the horizon; i.e., it does not depend on the choice of coordinate system. In the case of free fall (along geodetic trajectories), $V^2 = 1 - e^{\nu}$const. In the nonrelativistic limit, the definition of V^2 coincides with the usual definition of the velocity.

For the collapse of dust matter or a Schwarzschild black hole ($P_{||} = P_\perp = 0$), we obtain

$$ds^2 = (1 - r_g/r)^{+1}dt^2 \quad (4)$$
$$- (1 - r_g/r)^{-1}dr^2 - r^2 d\Omega^2,$$
$$V^2 = [(R_0/r) - 1] \,/\, [(R_0/r_g) - 1].$$

Here and below, R_0 is the initial value of the r coordinate for the falling particle and the event horizon is defined by $V = 1$.

For an inflating de Sitter universe ($P_{||} = P_\perp = -\varepsilon$), we obtain

$$ds^2 = (1 - r^2/a_H^2)^{+1}dt^2 \quad (5)$$
$$- (1 - r^2/a_H^2)^{-1}dr^2 - r^2 d\Omega^2,$$
$$V^2 = \left[(r/R_0)^2 - 1\right] \,/\, \left[(a_H/R_0)^2 - 1\right].$$

Here, $H \equiv 1/a_H$ is the Hubble constant.

3. BRIDGES

The relation between the circumference of a circle and its radius is violated in curved space. Therefore, to avoid misunderstanding, let us introduce the following new coordinates. Let us choose some point in space as a central point. Next, we draw rays from this point in all directions. Distance along the rays will be measured by the coordinate l, and distance in the perpendicular direction, by the coordinate r. Therefore, the circumference will be (by definition) $2\pi r$, while the distance from the center of the circle to its boundary will be (by definition) l.

In such coordinates, expression (1) for a static case takes the form

$$ds^2 = \exp(2\phi)dt^2 - dl^2 - r^2 d\Omega^2. \quad (6)$$

In a curved space, $r \neq l$. To illustrate this fact, let us put a small mass (for example, a planet such as the Earth) at the center of the system. Here, "small mass" implies a body whose Newtonian gravitational potential at its surface is much less than the square of

---

[1] We use the theoretical system of units in which the speed of light is $c = 1$ and the gravitational constant is $G = 1$.

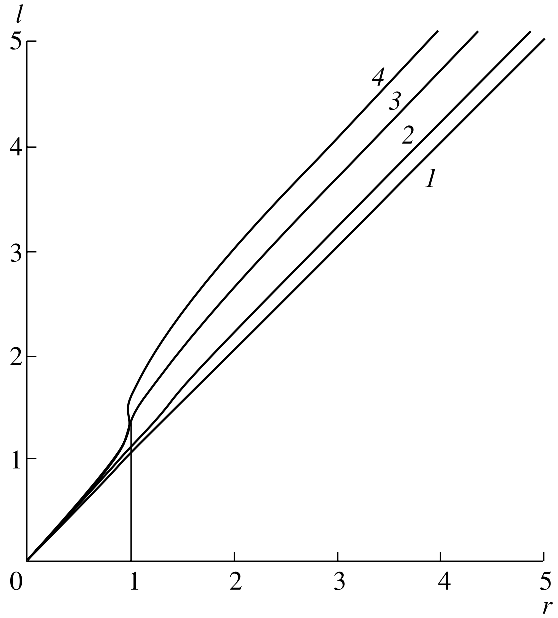

Fig. 2. The dependence of l on r for various values of the Newtonian potential φ_g at the surface of a body ($r = 1$): (*1*) $\varphi_g = 0.1$ (nearly coincident with the straight line $l = r$ corresponding to $\varphi_g = 0$), (*2*) $\varphi_g = 0.5$, (*3*) $\varphi_g = 0.9$, and (*4*) $\varphi_g = 0.99$.

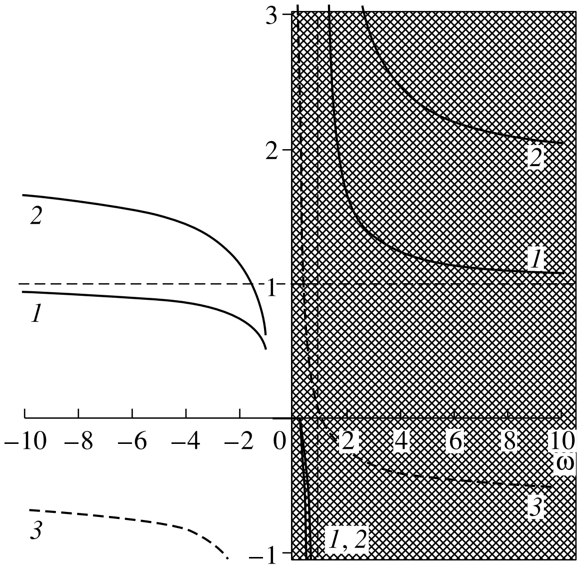

Fig. 3. Dependence of the following quantities for bridges on the equation of state (namely, on $w = w_{||} = -w_{\perp}$): (*1*) r_0/r_g, (*2*) r_l/r_g, (*3*) $\phi_{\max}$. The left-hand (unshaded) side of the plots corresponds to the physical region $\varepsilon > 0$, and the right-hand (shaded) side, to the unphysical region $\varepsilon < 0$.

the speed of light. For the Earth, this potential is $\varphi_g \sim 10^{-9}$; for the Sun, $\varphi_g \sim 10^{-5}$; and for a pulsar, $\varphi_g \sim 0.5$. The dependence of l on r is illustrated by the plots in Fig. 2. This curving of spacetime by gravitating matter was predicted by Einstein and subsequently confirmed by numerous experiments.

As the central body becomes heavier, it curves space more strongly and stretches it along the radii. When a certain limit is achieved, the space is curved so strongly that a black hole is formed. What are the limiting objects just before the formation of black holes, and are black holes always formed?

One well-known limit is a neutron star (pulsar), whose mass is of the order of a solar mass and whose radius is about ten kilometers; the average density of matter in the neutron star is approximately equal to the density of an atomic nucleus, $\sim 10^{13}$ g/cm^3.

The aforementioned curvature of the space is negligible for normal stars and planets and is important only for neutron stars (see curve *2* in Fig. 3).

The limiting curvature occurs when the inclination of the curve $l(r)$ with respect to the r axis increases from 45° (the uncurved geometry) to 90° (the most curved geometry). In this case, we obtain a zero increment in r for a nonzero increment in l. In Fig. 2, curve *4* with $\varphi_g = 0.99$ is closest to this situation (as follows from calculations, this limit is not actually reached: the star collapses before this occurs, when $\varphi_g \sim 0.5$). After the collapse of a star to a black hole, l becomes imaginary after it passes the singularity indicated above. This is not a physical but a coordinate singularity at the black-hole event horizon, which can be avoided by an appropriate coordinate transformation. The condition $V = 1$ can serve as the invariant definition of the horizon [see (3)].

There is also an alternative to the curving of physical space by a black hole. Above, a decrease in l was accompanied by a decrease in r. If there is a black hole at the center of the system, the coordinate l becomes imaginary at its event horizon. However, there are static solutions in general relativity in which, after passage of the singularity, r again begins to increase as l is decreased. Such solutions can correspond to bridges.

Let us present here the definition of a bridge that has been adopted in a number of studies (for example, [6, 7]):

(1) A bridge must have a region where r reaches a local minimum, r_0. This region is called the throat of the bridge, and r_0, the throat radius (Fig. 1). This is the main difference between a bridge and any other body.

(2) There must be no event horizons in the bridge; i.e., bodies falling into the bridge must not reach the speed of light ($V < 1$) and, consequently, they should be observable for an external observer.

(3) Bodies can pass through the bridge throat in both directions.

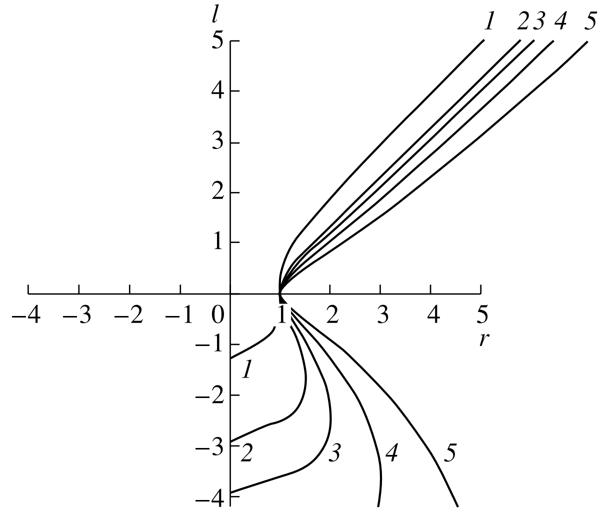

Fig. 4. Probable dependence of r on l in a bridge during its detachment. The numbers *1* to *5* correspond to successive times in the bridge's evolution.

Geometry can be different on the opposite sides of the bridge throat. We shall consider from here on only spherically symmetric static solutions for bridges obeying the equation of state

$$P_{||} = w_{||}\varepsilon, \qquad P_{\perp} = w_{\perp}\varepsilon. \tag{7}$$

Here, $w_{||}$ and $w_{\perp}$ are constant parameters, and the energy density ε must not be negative. Such matter is, of course, idealized, but it enables us to study analytically many important features of bridges.

The matter forming such bridges should have exotic properties, since the allowed range of $w_{||}$ and $w_{\perp}$ is restricted by the inequality (see Appendix 1)

$$\varepsilon > 0, \qquad -2w_{\perp} < w_{||} < -1. \tag{8}$$

We can see that, in order for a bridge to exist, the signs of $w_{||}$ and $w_{\perp}$ must be opposite. Therefore, the equation of state must be substantially hard and anisotropic.

The mass m and gravitational radius r_g of a bridge are defined in the same way as for any other body, via the field asymptotics at infinity:

$$\lim_{r\to\infty} \exp(-\lambda) = 1 - r_g/r, \qquad m = r_g/2. \tag{9}$$

In addition to its mass, a bridge is characterized by two dimensions: its length and width. The bridge width can be identified with the size of its throat r_0. The bridge length can be reasonably related to the physical characteristics of a body passing through the bridge, for example, the change in the red (or violet) shift of the signal received from this body. Therefore, let us define the bridge length r_l to be the distance between the points at which the red (or violet) shift from a body at rest is half its maximum value. In the spherically symmetric case, the ratios r_0/r_g and r_l/r_g depend only on the equation of state of the bridge. Figure 3 presents the dependences of the ratios r_0/r_g and r_l/r_g on $w = w_{||} = -w_{\perp}$ obtained numerically (see Appendix 1). The first diagram in this figure clearly shows why bridges exist only when $w < -1$: the function r_0/r_g tends to zero as $w \to -1$. Therefore, the radius of the throat decreases to zero, and passage to another part of the Universe is no longer possible.

4. FORMATION AND EXISTENCE OF BRIDGES

The question of the formation (and, in general, the existence) of bridges remain open, and two scenarios are possible.

1. The trivial scenario: bridges were formed during the birth of our part of the Universe and still exist, preserving the global topology (geometry) of the Universe. This is the only way to form bridges connecting two different parts of our Universe (like a door handle), since the modern geometrical theorems of general relativity forbid the disruption of such a topology [7]. We cannot currently answer the question of how this topology was created, since Einsteinian gravitational theory cannot be applied to the birth of the Universe (quantum gravity, which remains incompletely developed, must be used).

2. The dynamic scenario: bridges could be formed instead of black holes as "branches" in the process of evolution of the Universe. This process of detachment is drawn schematically in Fig. 4. First, the matter (accumulated due to self-gravity) curves space. Next, the amount of matter becomes sufficient to curve the geometry to the limiting value at some radius (Fig. 2). The matter then begins to inflate the space behind this radius, similar to the inflation of space by the vacuum condensate in the observed expanding Universe (as a consequence of negative pressure). There must be no event horizons anywhere. The resulting branch evolves by itself, expands, and forms a new part of the Universe, connected to our part of the Universe by the throat of the bridge.

5. OBSERVATION OF BRIDGES

The simplest way to detect a bridge is to observe some objects (e.g., stars) through its throat. If the geometry of the Universe is different on the opposite sides of the throat (see Appendix 2), the rate of flow of time will also be different. As a result, photons passing the bridge's throat will experience a red (or violet) shift. An important problem with this method is to discriminate such shifts from Doppler shifts due to the source motion.

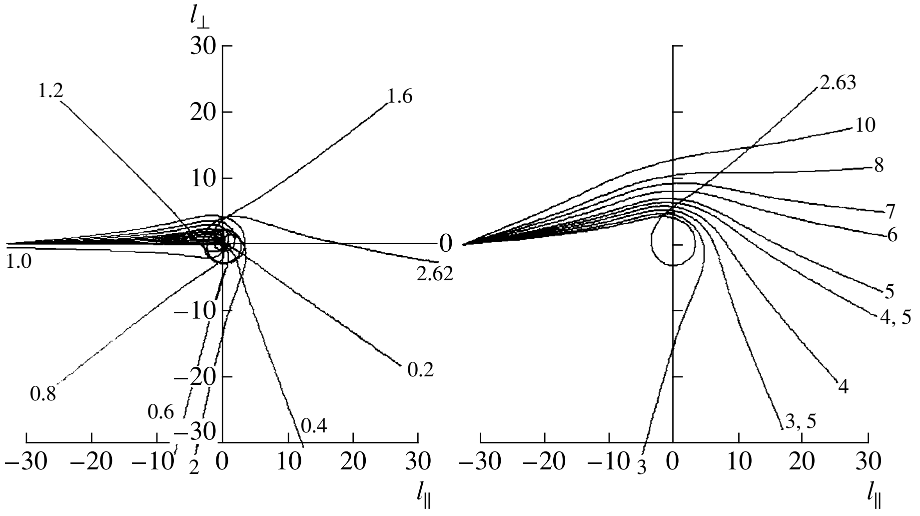

Fig. 5. Deflection of photons by a bridge with $w = -2$. The trajectories of photons deflected through an angle $\Delta\varphi$ from the initial direction are plotted. The trajectories start at $l = -32r_0, \varphi = -\pi$. Trajectories passing through the throat at small impact parameters ($h < h_{cr} \approx 2.621r_0$) and terminating at $l \to +\infty$ are shown in the left-hand panel. Trajectories not passing through the throat ($h > h_{cr}$) and terminating at $l \to -\infty$ are shown in the right-hand panel. The numbers near the ends of the curves indicate the impact parameters (in units of r_0). The coordinates $l_\parallel, l_\perp$ denote the equatorial plane of the photon scattering ($l_\parallel = |l| \cos\varphi, \quad l_\perp = -|l| \sin\varphi$).

Another method is based on the idea that the photons in light signals passing through the throat of a bridge should experience a deflection; i.e., they should undergo lensing by the curved geometry of the space (see, for example, [9]). Let us define the impact parameter h for a photon deflected by a bridge to be $h = L/E$, the ratio of the angular momentum and energy of the photon at infinity.

There are two type of lensing (see Appendix 3).

1. The photon does not pass through the throat, and so always remains in the same part of the Universe. This situation takes place for photons that have sufficiently large impact parameters (in comparison with the throat radius) and are deflected by the gravitational lens.

2. The photon passes through the throat to another part of the Universe. This situation takes place for photons having sufficiently small impact parameters (compared to the throat radius). One characteristic feature of this effect is that the deflection of the photons is given by the formula for a thin converging lens whose focal distance is approximately equal to the throat radius. In the case of other gravitating centers, these photons would be absorbed by the surface of the body.

The calculated photon trajectories for a bridge with $w = -2$ are presented in Fig. 5. If the impact parameter is close to the critical value h_{cr}, the photons can be deflected through large angles (greater than 2π) by the bridge. Note that photons passing through the throat inevitably intersect the center of the bridge; i.e., the point $l = 0$. There is no singularity at this point, since the value $l = 0$ corresponds to a sphere of finite radius r_0.

Since the photon impact parameter does not change and corresponds to a location in the bridge's throat (relative to its center) from which we can observe the light of a star from another part of the Universe, the impact parameter can be used to determine the deflection angle of the photon on its way to the observer. In fact, this is a method to determine the coordinates of stars in that part of the Universe.

6. DISCUSSION

Not only photons but also physical bodies can pass through a bridge. The main obstacles to this are tidal forces, which disrupt bodies inside black holes and in the orbits of compact stars (such as neutron stars). The tidal forces depend on the curvature of space and the size of the body. Therefore, they coincide in order of magnitude with the corresponding forces in black holes of the same mass. The tidal forces affecting a body of mass μ and size d are proportional to the derivative of the gravitational forces. For black holes, the tidal forces are equal to $\mu c^2 d/r_g^2$ at the event horizon. In order of magnitude, the same forces should act in bridges. If a bridge possesses a sufficiently large mass, then not only macroscopic objects but also stars, such as the Sun, can pass through its throat without disruption. This should be the case for bridges with masses of a few billion solar masses (as in some quasars). A person would not feel the passage through such a bridge, because the tidal forces would be extremely small.

7. CONCLUSIONS

Our main conclusion is that bridges can be real objects which are described by Einstein gravitational theory in a self-consistent way and can be distinguished from other celestial bodies by observations.

The equation of state of the matter in traversable bridges described by general relativity must be substantially hard and anisotropic [see (8)].

Gravitational lensing by bridges is fundamentally different from lensing by other bodies, and precisely these differences can be used to identify bridges and study their properties (as well as the properties of the part of the Universe on the opposite side of the bridge).

ACKNOWLEDGMENTS

I am grateful to I.D. Novikov and N.S. Kardashev for their help and participation in my preparation of this article. This work was supported by the Program "Nonstationary Phenomena in Astronomy," the Program of Support for Leading Scientific Schools (project NSh-1653-2003.2), and the Russian Foundation for Basic Research (project nos. 01-02-16812, 01-02-17829, and 00-15-96698).

Appendices

1. NUMERICAL SOLUTION

The Einstein equations corresponding to (6) and (7) are [9]

$$2\varepsilon r^2 = -2r''r + (1 - r'^2), \tag{10}$$

$$2w_{||}\varepsilon r^2 = 2r\phi' r' - (1 - r'^2), \tag{11}$$

$$2w_{\perp}\varepsilon = \phi'' + \phi'^2 + (\phi' r' + r'')/r. \tag{12}$$

These equations lead to the following expression (which can be derived most easily from the equality $T^k_{l;k} \equiv 0$):

$$w_{||}(\ln\varepsilon)' = (w_{\perp} - w_{||})(\ln r^2)' - (1 + w_{||})\phi'. \tag{13}$$

Here, a prime denotes a derivative with respect to l, which is related to r as

$$dl = \pm\sqrt{\exp(\lambda)}dr, \tag{14}$$

$$l(r) = \pm\int\limits_{r_0}^{r} \sqrt{\exp(\lambda)}dr,$$

$$r(l) = r_0 \pm \int\limits_{0}^{l} \sqrt{\exp(-\lambda)}dl.$$

Here and below, the upper and lower signs correspond to positive and negative values of l, respectively. The new constant r_0 appearing here is defined as the minimum of the function $r(l)$: $r'(0) \equiv 0$.

Let us introduce the new functions

$$a(l) \equiv r(1 - e^{\nu}), \tag{15}$$

$$b(l) \equiv r_0 + \int\limits_{0}^{l} 2\varepsilon r^2 r' dl,$$

in which case (10) can be rewritten as

$$b' \equiv 2\varepsilon r^2 r' = \Big[r(1 - r'^2)\Big]'. \tag{16}$$

Definitions (14) can be rewritten as

$$(r')^2 = \exp(-\lambda) = 1 - b/r, \tag{17}$$

$$l = \pm\int\limits_{r_0}^{r} (1 - b/r)^{-1/2}\, dr.$$

Consequently, metric (6) will take the form

$$ds^2 = (1 - a/r)dt^2 - (1 - b/r)^{-1}dr^2 - r^2 d\Omega^2. \tag{18}$$

Equation (11) can be rewritten as

$$w_{||}b' \equiv 2w_{||}\varepsilon r^2 r' = 2(r - b)\phi' - r'b/r. \tag{19}$$

In order for the quantities a and b (corresponding to twice the mass of the system) to be limited, the energy density $\varepsilon(r)$ must tend to zero at infinity faster than const/r^3. The left-hand side of (19) then tends to zero as $r \to \infty$ faster than the right-hand side and can, therefore, be neglected. In this limit, $\phi' \to ar'/(2r^2)$. Consequently, a and b tend to the same limit, which is twice the mass of the system or its gravitational radius:

$$\lim_{r\to\infty} a = \lim_{r\to\infty} b = 2m = r_g. \tag{20}$$

Since $b(l = 0) = b_0 = r_0$ and $\lim\limits_{r\to r_0}(r') \propto \sqrt{r - b}$, Eq. (19) gives

$$\varepsilon_0 = -\frac{1}{2w_{||}r_0^2}. \tag{21}$$

Further, we can exclude the variable l from (13), (15), and (19) by substituting r. Using the new variables

$$x = r/r_0, \qquad y = b/b_0, \qquad (22)$$
$$\xi = \varepsilon/\varepsilon_0,$$

the resulting equations can be reduced to the integral form

$$y(x) = 1 - \frac{1}{w_{||}}\int\limits_1^x \xi x^2 dx, \qquad (23)$$

$$\xi'(x) = \xi\left[\left(\frac{w_\perp}{w_{||}} - 1\right)\frac{2}{x} + \frac{1}{2}\left(\frac{1}{w_{||}} + 1\right)\frac{\xi x - y/x^2}{1 - y/x}\right], \qquad (24)$$

$$\xi(x) = 1 + \int\limits_1^x \xi' dx, \qquad (25)$$

$$\exp(\phi) = \exp(\phi_0)\xi^{-\frac{1}{1/w_{||}+1}} x^{2\frac{w_\perp/w_{||}-1}{1/w_{||}+1}}. \qquad (26)$$

The factor $\exp(\phi_0)$ can be derived from the equality $\exp(\phi(+\infty)) = 1$. These equations are closed and very convenient for numerical integration.

The parameters $w_{||}$ and $w_\perp$ must satisfy two requirements. The first was already noted before: the restriction on the total mass of the system. This condition leads to the inequality $x\xi'/\xi < 3$ and, as can easily be derived from (24),

$$2w_\perp/w_{||} < -1. \qquad (27)$$

The second requirement is associated with the integrability of Eq. (17) for l: the absence of an event horizon in the system. Since $y(1) = 1$, the inequality $[y(x)/x]' \leq 0$ must be satisfied at the point $x = 1$. This leads to the second condition[2]:

$$1/w_{||} < -1. \qquad (28)$$

Conditions (27) and (28) taken together lead to the two possible cases for the range of $w_{||}$ and $w_\perp$.

The first case is physical and is represented by inequality (8).

The second case is

$$\varepsilon < 0, \qquad 0 < w_{||} < -2w_\perp. \qquad (29)$$

This case is of less practical interest, since it supposes the existence of matter with negative energy density.

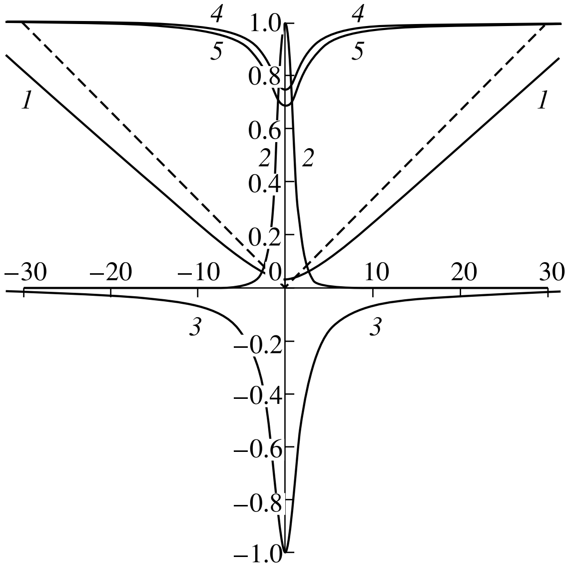

Fig. 6. Numerical solution for a bridge with $w_{||} = -w_\perp = -2$, $l_{\max} = 30r_0$: *(1)* $r(l)/l_{\max}$, *(2)* $\xi(l) = \varepsilon(l)/|\varepsilon_0|$, *(3)* $\phi(l)/|\phi_{\max}|$, *(4)* $b(l)/r_g$, and *(5)* $a(l)/r_g$. The lines $|l|/l_{\max}$ are shown dashed.

However, we were able to obtain an analytic solution for a bridge when $w_{||} = -w_\perp = 1$ (see below).

It has not yet been possible to find an analytical solution for a bridge in the first case, but solutions have been obtained numerically (for example, for $w_{||} = -w_\perp = -2$, Fig. 6). This case is of the most interest, since a positive energy density corresponds to positive masses. (It is quite unclear what negative mass is and to what type of matter it corresponds.)

Equations (23)–(25) can be transformed from integral to differential form. This is the most convenient form when $w = w_{||} = -w_\perp$. Equations (23)–(25) are transformed to the single nonlinear equation for $y(x)$

$$2(x - y)(xy'' + 2y') + (1 + w)(xy'^2 + yy'/w) = 0. \qquad (30)$$

The solution of this equation that is finite at infinity can be written as the series

$$y(x) = \sum_{n=0}^{\infty} C_n/x^n, \qquad \sum_{n=0}^{\infty} C_n = 1. \qquad (31)$$

This expression yields the following three exact solutions for the static equations of general relativity.

1. The Schwarzschild solution for a black hole:

$$w \text{ is arbitrary, because } \varepsilon = 0, \quad y = 1 \quad \text{or} \qquad (32)$$
$$b = r_g = r_0.$$

2. The Reissner–Nordstrom solution for an electrically charged black hole [11, 12]:

$$w = -1, \quad y = C_0 + C_1/x \quad \text{or} \qquad (33)$$

---

[2] In general, the exact equality also corresponds to a static solution, but, in this case, it follows from (19) that this solution possesses an event horizon, $2\phi = \ln(1 - b/r)$; i.e., it cannot represent a bridge.

$$b = r_g - Q^2/r,$$

where Q is the electric charge.

These solutions can easily be verified using formulas (17)–(19).

3. The exact analytic solution for a bridge in the case $w = 1$ takes the form

$$w = +1, \quad y_{w=1} = 1/x \quad \text{or} \quad b = r_0^2/r. \tag{34}$$

This solution is described in detail in the next Appendix.

2. ANALYTIC SOLUTION

The metric of the well-known solution for a stable macroscopic bridge [6] is ($w = w_{||} = -w_{\perp} = +1$)

$$ds^2 = (1 - 2\eta/R)^{m/\eta} dt^2 - (1 - 2\eta/R)^{-m/\eta} dR^2 \tag{35}$$
$$- (1 - 2\eta/R)^{1-m/\eta} R^2 d\Omega^2.$$

Here, $\eta^2 = m^2 + q^2$ are the mass and charge of the bridge. The metric (35) reduces to the Schwarzschild metric if the charge is zero.

By substituting for the coordinate R, this metric can be reduced to real form in the entire space for $\eta^2 < 0$:

$$ds^2 = \exp(-2m/\tilde{R}) dt^2 \tag{36}$$
$$- \exp(2m/\tilde{R}) \left[dR^2 + (|\eta|^2 + R^2) d\Omega^2 \right].$$

Here, $\cos^2(|\eta|/\tilde{R}) = R^2/(|\eta|^2 + R^2)$.

Using the coordinate transformation $r^2 = (|\eta|^2 + R^2) \times \exp(2m/\tilde{R})$, the metric can be expressed in terms of the coordinate r:

$$ds^2 = \frac{|\eta|^2 + R^2}{r^2} dt^2 - \frac{|\eta|^2 + R^2}{(R - m)^2} dr^2 - r^2 d\Omega^2. \tag{37}$$

The corresponding derivative takes the form

$$\frac{dr}{dR} = \frac{(r/|\eta|)(R/|\eta| - m/|\eta|)}{1 + R^2/|\eta|^2}. \tag{38}$$

We can now find a relation between R and l:

$$l = R - m \text{ at } r = r_{\min}. \tag{39}$$

The corresponding right-hand sides of the Einstein equations take the form

$$2\varepsilon = 2P_{||} = -2P_{\perp} = \frac{q^2}{r^2(R^2 - \eta^2)} < 0. \tag{40}$$

If η is imaginary, the coordinate r has a minimum, corresponding to the bridge's throat. The bridge is completely defined by the quantities

$$r = |\eta| \sqrt{1 + R^2/|\eta|^2} \tag{41}$$
$$\times \exp\left\{ (m/|\eta|) \left[\pi/2 - \arctan(R/|\eta|) \right] \right\},$$
$$\phi = (-m/|\eta|) \left[\pi/2 - \arctan(R/|\eta|) \right],$$
$$b/r = \left(1 + 2mR/|\eta|^2 - m^2/|\eta^2| \right) / (1 + R^2/|\eta|^2),$$
$$V^2 = 1 - \exp\{ (2m/|\eta|) [\arctan(R/|\eta|)$$
$$- \arctan(R_0/|\eta|)] \}.$$

We can see that this solution is symmetric about the throat only in the case of zero mass m (Fig. 7). In this case, the expression for b coincides with (34).

3. DEFLECTION OF PHOTONS BY THE FIELD OF THE BRIDGE

To calculate a photon trajectory in the gravitational field of a bridge, we use the theory described in [10, § 101]. A photon eikonal in the equatorial plane of a centrally symmetric field will take the form

$$\Psi = -Et + L\varphi + \Psi_l, \tag{42}$$

where E and L are the conserved energy and angular momentum of the photon, $\Psi_l(l)$ is the radial part of the eikonal, and φ is the azimuthal angle in the equatorial plane. The Hamilton–Jacobi equation for this eikonal is

$$e^{-\nu} (\partial_t \Psi)^2 - (\partial_l \Psi)^2 - (\partial_\varphi \Psi)^2 / r^2 = 0. \tag{43}$$

We thus obtain

$$\Psi_l = \int \sqrt{E^2/(1 - a/r) - L^2/r^2} dl, \tag{44}$$

$$t - t_0 = \int_{l_0}^{l} \frac{E/(1 - a/r) dl}{\sqrt{E^2/(1 - a/r) - L^2/r^2}}, \tag{45}$$

$$\varphi - \varphi_0 = \int_{l_0}^{l} \frac{(L/r^2) dl}{\sqrt{E^2/(1 - a/r) - L^2/r^2}}. \tag{46}$$

Let the photons be emitted in that part of the Universe characterized by negative values of l. Then, these photons enter our part of the Universe (with positive values of l) when they pass through the bridge. We obtain from the previous three expressions

$$\partial_t l = \pm \sqrt{(1 - a/r) - (1 - a/r)^2 h^2/r^2}, \tag{47}$$
$$\partial_t \varphi = h(1 - a/r)/r^2,$$
$$\partial_t r = \mp (1 - a/r) \sqrt{(1 - b/r)((1 - a/r)^{-1} - h^2/r^2)}.$$

Particular attention should be paid here to the signs ±.

The equation for the trajectory $\varphi(r)$ is obtained by integrating over the radius r. The sign of the integrand changes together with the changing sign in (47) when the point of minimum radius is passed. In

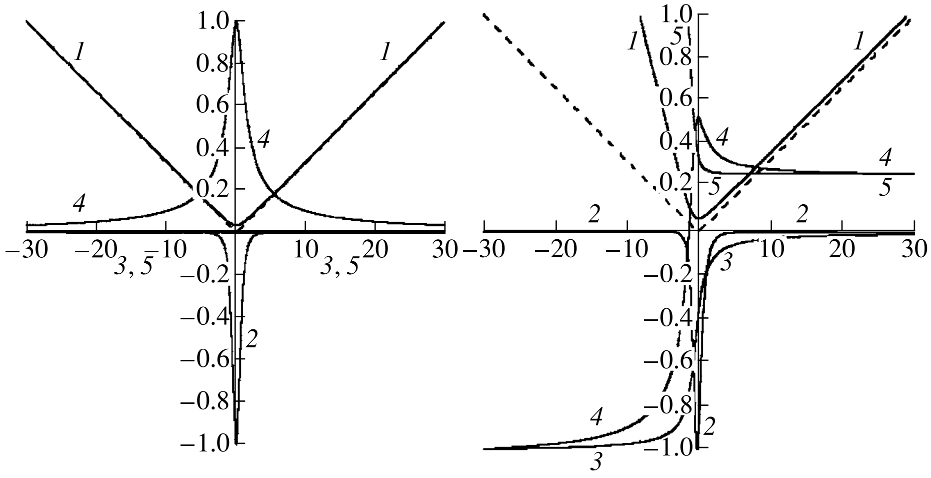

Fig. 7. Analytic solution for a bridge with $w_{||} = -w_{\perp} = +1$ at $l_{\max} = 30r_0$: (*1*) $r(l)/l_{\max}$, (*2*) $\varepsilon(l)/|\varepsilon_{\max}|$, (*3*) $\phi(l)/|\phi_{\max}|$, (*4*) $b(l)/|b_{\max}| \to r_g/|b_{\max}|$, and (*5*) $a(l)\mathrm{const} \to r_g/|b_{\max}|$. The lines $|l|/l_{\max}$ are shown dashed. The left-hand panel represents the symmetric solution for $m = 0$, and the right-hand panel, the asymmetric solution for $m = 0.2|\eta|$.

the limiting case of infinite initial and final radii, the change of the angle φ is

$$\Delta\varphi \quad (48)$$

$$= 2\int\limits_{r_{\min}}^{\infty} \frac{h}{r^2\sqrt{(1-b/r)((1-a/r)^{-1}-h^2/r^2)}}dr.$$

This expression can be integrated in explicit form in two important limiting cases:

(1) $h \ll r_0$, $h \ll a$, $h \ll b$ is the case when the impact parameter is sufficiently small that the photon can pass through the throat. In this case, $r_{\min} = r_0$ and the h^2/r^2 term in the denominator of (48) can be neglected. Assuming that a and b are constant, we obtain

$$\Delta\varphi_{I} = \frac{2h}{b}\Bigg\{1 - \sqrt{\left(\frac{b}{r_0}-1\right)\left(\frac{a}{r_0}-1\right)} \quad (49)$$

$$+ \frac{b-a}{2\sqrt{ab}}$$

$$\times \ln\left[\frac{(\sqrt{b(a-r_0)}+\sqrt{a(b-r_0)})(\sqrt{b}-\sqrt{a})}{(\sqrt{b(a-r_0)}-\sqrt{a(b-r_0)})(\sqrt{b}+\sqrt{a})}\right]\Bigg\}.$$

This formula is analogous to that for a converging thin lens.

(2) $h \gg r_0$, $h \gg a$, $h \gg b$ is the case when the impact parameter is sufficiently large that the photon does not pass through the throat. In this case, $a \approx b \approx r_g$ is a constant and $r_{\min}$ is determined by the equation $r_{\min}^2 + ar_{\min} - h^2 = 0$. Neglecting terms quadratic in a/h and b/h and substituting the variable $z = r - b/2$, we obtain $z_{\min} \approx h - (a+b)/2$,

$$\Delta\varphi_{II} = \pi + \frac{a+b}{h}. \quad (50)$$

This expression coincides with the usual formula for the gravitational lensing of photons when $a = b = r_g$.

When a photon trajectory corresponds to the first or second cases depends on the value of the impact parameter compared to the critical value defined by the equation

$$re^{-\phi} = h_{cr} = \min \quad \text{or} \quad 1 - r_{cr}\phi'(r_{cr}) = 0. \quad (51)$$

For example, for a bridge with $w = -2$, one can find numerically that $h_{cr} \approx 2.621r_0$.

REFERENCES

1. A. Einstein and N. Rosen, Phys. Rev. **48**, 73 (1935).
2. M. Morris and K. Thorne, Am. J. Phys. **56**, 395 (1988).
3. A. Carlini, V. P. Frolov, M. B. Mensky, *et al.*, gr-qc/9506087.
4. A. D. Linde, *Elementary Particles Physics and Inflation Cosmology* (Nauka, Moscow, 1990) [in Russian].
5. A. A. Shatskiĭ and A. Yu. Andreev, Zh. Éksp. Teor. Fiz. **116** (8), 353 (1999) [JETP **89**, 189 (1999)].
6. C. Armendariz-Picon, gr-qc/0201027.
7. M. Safonova, astro-ph/0401542.
8. Matt Visser, *Lorentzian Wormholes from Einstein to Hawking* (United Book, Baltimore, USA, 1996).
9. M. B. Bogdanov and A. M. Cherepashchuk, Astron. Zh. **79**, 1109 (2002) [Astron. Rep. **46**, 996 (2002)].
10. L. D. Landau and E. M. Lifshits, *Field Theory* (Nauka, Moscow, 1988) [in Russian].
11. I. D. Novikov and V. P. Frolov, *Black-Holes Physics* (Nauka, Moscow, 1986) [in Russian].
12. C. W. Misner, K. S. Thorne, and J. A. Wheeler, *Gravitation* (Freeman, San Francisco, 1973; Mir, Moscow, 1977), Vols. 1–3.

Translated by Yu. Dumin

Astronomy Reports, Vol. 48, No. 7, 2004, pp. 534–549. Translated from Astronomicheskiĭ Zhurnal, Vol. 81, No. 7, 2004, pp. 589–605.
Original Russian Text Copyright © 2004 by Tutukov, Fedorova.

The Evolutionary Status of Ultraluminous X-ray Sources

A. V. Tutukov and A. V. Fedorova
Institute of Astronomy, Moscow, Russia

Received January 5, 2004; in final form, January 9, 2004

Abstract—We analyze models for quasi-stationary, ultraluminous X-ray sources (ULXs) with luminosities 10^{38}–10^{40} erg/s exceeding the Eddington limit for a $\sim 1.4\ M_\odot$ neutron star. With the exception of relatively rare stationary ULXs that are associated with supernova remnants or background quasars, most ULXs are close binary systems containing a massive stellar black hole (BH) that accretes matter donated by a stellar companion. To explain the observed luminosities of $\sim 10^{40}$ erg/s, the mass of the BH must be $\sim 40\ M_\odot$ if the accreted matter is helium and $\sim 60\ M_\odot$ if the accreted matter has the solar chemical composition. We consider donors in the form of main-sequence stars, red giants, red supergiants, degenerate helium dwarfs, heavy disks that are the remnants of disrupted degenerate dwarfs, helium nondegenerate stars, and Wolf–Rayet stars. The most common ULXs in galaxies with active star formation are BHs with Roche-lobe-filling main-sequence companions with masses $\sim 7\ M_\odot$ or close Wolf–Rayet companions, which support the required mass-exchange rate via their strong stellar winds. The most probable candidate ULXs in old galaxies are BHs surrounded by massive disks and close binaries containing a BH and degenerate helium-dwarf, red-giant, or red-supergiant donor. © *2004 MAIK “Nauka/Interperiodica”*.

1. INTRODUCTION

The discovery of ultraluminous ($L_x \gtrsim 2 \times 10^{38}$ erg/s) X-ray sources (ULXs) has raised the question of their evolutionary status [1–3]. If their emission is isotropic, the inferred luminosities of some reach $\sim 10^{41}$ erg/s [3, 4]. If this luminosity is due to accretion onto a black hole (BH), the accretion rates must be $\sim 10^{-5}\ M_\odot$/yr, and the BH masses, up to $10^3\ M_\odot$.

Two important features of most ULXs are their compact size (less than half an arcsecond) and the variability of their X-ray flux by factors of up to two to three [3]. Long (~ 155 h) series of observations of two ULXs in the spiral galaxy IC 342 revealed periodic variations of the intensity of the 7–10 keV emission of one of the sources with an amplitude of $\sim 5\%$ and a period of 30–40 h [5]. A ULX with a luminosity of $\sim 2 \times 10^{39}$ erg/s in the galaxy M51 displays variations of its X-ray flux with $f_{max}/f_{min} \approx 4$ and a period close to 2 h [6]. The ULX HF 16 in NGC 6946 was also suspected of being a binary [7]. This suggests that at least some, and perhaps a substantial fraction, of ULXs are binaries. In addition, the rapid variability of some ULXs rules out their identification with supernova remnants that expand into a dense interstellar medium with speeds of several thousands of km/s.

The observed luminosity function of X-ray sources [8] suggests that a large fraction of the X-ray flux from galaxies is due to ULXs, since they provide the main input to the total flux. The ratio of the X-ray and optical luminosities of massive spiral galaxies is $\sim 10^{-4}$–10^{-2} [9–11]. This ratio probably decreases with decreasing mass of the galaxy [8, 9]. However, note that the luminosity ratio for a specified optical luminosity of the galaxy has a large scatter. This probably reflects a strong dependence of the X-ray luminosity of these galaxies on the luminosity of several brightest ULXs.

It is natural to suppose that some ULXs may be in distant active galactic nuclei (supermassive BHs in AGN) that overlap by chance with nearby galaxies on the celestial sphere [12]. However, the positions of most ULXs are clearly concentrated toward the host galaxies in the sky, suggesting that most ULXs do belong to these galaxies [7]. However, some ULXs are indeed background sources [13], and this must be borne in mind when interpreting data for particular ULXs.

Detailed studies of galactic populations reveals an additional class of potential ULXs: black holes with intermediate masses (10^3–$10^4\ M_\odot$ [14, 15]), as have been discovered in the cores of globular clusters. The role of such objects is not clear, since the few known ULXs with $L_x \sim 10^{41}$ erg/s can be explained by the collimation of emission from accretion disks around stellar-mass BHs [16] or by the chance projection of distant quasars onto nearby galaxies.

2. MAIN OBSERVATIONAL FEATURES OF ULXs

Important information about the nature of ULXs is provided by their distribution in the host galaxies. The presence of ULXs in colliding galaxies with vigorous star formation demonstrates that most ULXs are located in giant complexes of ionized hydrogen that trace regions of active star formation. This implies that most ULXs in galaxies with active star formation are produced by massive, short-lived, and probably close binary systems. However, ULXs are abundant in elliptical as well as spiral galaxies (Figs. 1a, 1b), with their luminosities in ellipticals (10^{39}–10^{41} erg/s) being nearly the same as in spirals [3]. Some ULXs have been detected in globular clusters [11, 17]. Moreover, the ULXs in the bulge of M31 are brighter than those in its disk, with its active star formation [18]. The integrated X-ray luminosity of early-type galaxies is correlated with the number of globular clusters in them [19]. This suggests that the ULXs in these galaxies are formed predominantly in globular clusters. It follows that there exists at least one family of ULXs that are related to long-living close binary systems. The accretors in these sources are BHs that formed in the distant past, while the donors are either low-mass (e.g., solar-mass) stars or massive gaseous disks produced via the tidal disruption of a companion.

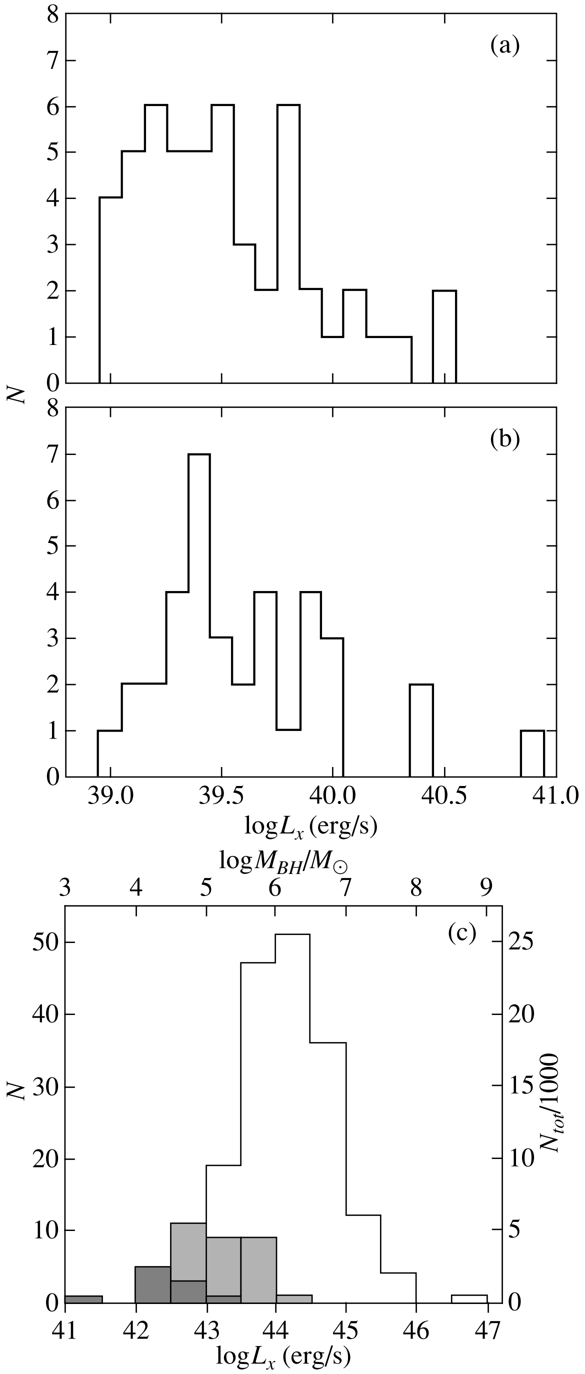

Fig. 1. X-ray luminosity distribution of observed ultraluminous sources in (a) spiral and (b) elliptical galaxies (data from [3]) and (c) the same distribution for AGN (data from [20]). Histogram (c) shows nearby galaxies with $z < 0.05$ in dark and galaxies with $z < 0.10$ in light gray.

Figure 1c shows the distribution of X-ray luminosities for 220 AGNs in a region of sky covering 81 square degrees [20] and gives an estimate of the total number of these objects over the celestial sphere, N_{tot}. The masses of the central BHs in these galaxies M_{BH} can be estimated if we assume that the luminosity is restricted by the Eddington limit. To estimate the obvious selection effects, we show separately distributions for nearby and distant AGNs ($R < 3 \times 10^8$ pc and $R < 7 \times 10^8$ pc). Comparison of Figs. 1a, 1b, and 1c reveals a "gap" between BHs with masses of $10^2\ M_\odot$ and $10^4\ M_\odot$. However, as a rule, this gap may be due to the absence of sources of fuel for intermediate-mass BHs; as a result, the average distance to ULXs is $\sim 10^7$ pc, while the average distance to quasars is $\sim 10^9$ pc. Figure 1c clearly shows that the typical luminosity (mass) of the BHs decreases with decreasing distance. Figure 1c can also be used to estimate the power-law index of the BH mass function in the range 10^4–$10^7\ M_\odot$. Comparison of the number of BHs with $z < 0.05$ and the total number of BHs with $M \gtrsim 10^4\ M_\odot$ from the catalog [13] gives $dN(\text{Mpc}^{-3}) \approx 7 \times 10^{-3} M_{BH}^{-1.6\pm0.2} dM_{BH}$. Thus, BH mass function can be used to estimate the number of nearby BHs (within 20 Mpc), which is close to the number of observed ULXs listed in the catalog [3]. This coincidence may underscore the possibility that ULXs and AGN are related objects.

Figure 1c also enables us to construct the X-ray luminosity function for quasars. The limiting distances to quasars with $z = 0.05$, 0.1, and 0.35 are, respectively, 3.2×10^8, 6×10^8, and 1.6×10^9 pc. If we assume a luminosity function of the form $dN \sim aL_x^{-b}dL_x$, we find from Fig. 1c that $b \approx 1.6 \pm 0.2$ and $a \approx 5 \times 10^{-18}$ pc^{-3}. This relation is valid for $L_x \gtrsim 10^8 L_\odot$ and $M_{BH} \gtrsim 10^4 M_\odot$, since the input catalog [20] contains only such sources. It is interesting that the slope of the latter distribution nearly coincides with the slope of the luminosity distribution of Galactic X-ray sources [13, 21], although the latter have luminosities of 10^{35}–10^{40} erg/s and masses below $\sim 100 M_\odot$.

The birth of a ULX requires a source of matter for accretion, and it is obvious that BHs spend only part of their lifetime as ULXs. For instance, the BH in the nucleus of our Galaxy, with a mass of $\sim 3 \times 10^6$ $M_\odot$ [22], would be transformed into an ordinary quasar (Fig. 1c) if it accreted at a rate of $\sim 3 \times 10^{-2}$ $M_\odot$/yr; this, obviously, does not happen, at least not at present. Thus, in most cases, BHs are dormant and it is accretion that activates them. Tidal disruption of individual stars probably cannot be the main source of matter for the BHs in quasars, since the timescale for continuous activity in quasars exceeds 2×10^4 yr [23], requiring the consumption of more than $\sim 200 M_\odot$. The activation of BHs in quasars is probably a consequence of collisions of gas-rich galaxies, which sharply enhance the rate of accretion by the central BHs of the colliding galaxies via the action of spiral shocks that form in the gaseous medium. It is possible that the swallowing of a globular cluster by a galactic nucleus is also able to activate accretion. An additional possibility for “feeding” quasars is the gradual disruption of stars that pass through the circumnuclear gaseous accretion disk.

The aim of the present paper is a comprehensive investigation of the possibilities provided by the modern theory of the evolution of close binaries to explain the evolutionary status of ULXs. In this model, the formation of a binary with the necessary properties requires that two main conditions be fulfilled. First, a BH with the maximum possible mass must be formed. Second, to provide a high luminosity, the conditions in the binary must enable a prolonged stage of intense mass exchange between the components. The first requirement is connected with the evolution of the most massive stars and estimation of the masses of the BHs produced at its endpoint.

The Hertzsprung–Russell diagrams for our Galaxy [24] and other nearby galaxies clearly show the existence of ~ 150–200 $M_\odot$ stars. Studies of star formation in the nucleus of M51 [25] confirm the presence of young stars with similar masses there. The presence of very massive stars is especially probable when the abundance of heavy elements is low [25–27]. No empirical relation between the initial mass of a star and the mass of the BH it produces is known. The highest mass of a BH in a close binary with known parameters is $\sim 14 \pm 4$ $M_\odot$ [28]. This may be far lower than the maximum masses of BHs produced by massive stars due to the small number of BHs with known masses. In addition, the shape of the initial mass function clearly shows that BHs should be concentrated toward lower masses, ~ 5–10 $M_\odot$, as is observed [29].

A theoretical estimate of the maximum mass of a stellar BH can be obtained as follows. The evolution of the most massive stars is determined mainly by mass loss via their stellar wind [11, 30–35]. To a first approximation, the strength of the wind is proportional to the abundance of heavy elements Z in the interval $Z = (0.01{-}1)Z_\odot$ [36–39]. It is obvious that the most massive BHs should have been produced by the first stars formed in the Galaxy, for which we can neglect the influence of the stellar wind because of their low Z values. Theoretical models of the evolution of massive stars lead to the relation between the initial masses of the stars and the masses of their helium cores $M_{\rm He}/M_\odot \approx 0.1(M_0/M_\odot)^{1.4}$ [30, 40–42]. Assuming that the maximum initial mass of a star is ~150 $M_\odot$ [24–27], we find that the mass of the corresponding helium remnant (Wolf–Rayet star) is ~100 $M_\odot$. The fact that binary systems survive the supernova explosions that accompany the transformation of Wolf–Rayet stars into BHs places a limit on the mass lost in the explosion—half of the initial mass [38]. Assuming that the initial mass is ~100 $M_\odot$, we thus find for the minimum mass of the resulting BH ~ 50 $M_\odot$. This value can be doubled, since the components of very close binary BHs will merge due to gravitational-wave radiation. The rate of such mergers in our Galaxy is $\sim 10^{-5}$/yr [43]. In the cores of globular clusters, where the rate of stellar collisions is high [44], such BHs can acquire close companions due to exchanges or tidal captures and become ULXs with the onset of mass exchange.

Thus, the evolution of single and close binary stars can result in the formation of BHs with masses of 50–100 $M_\odot$. If the donor transfers matter sufficiently efficiently, a ULX appears, whose maximum X-ray luminosity L_x can be estimated by the relation

$$L_x \approx \frac{2.5 \times 10^{38}}{1+X}\left(\frac{M_{BH}}{M_\odot}\right) \text{ erg/s}, \qquad (1)$$

where X is the abundance of hydrogen in the accreted matter. According to this relation, if the BH mass is $M_{BH} \approx 50$–100 $M_\odot$, the accretion of helium can support a ULX luminosity of $\sim 10^{40}$ erg/s. The discovery of brighter ULXs either implies collimation of the radiation of the accretion disk, marks the position of a dense cluster of ULXs (e.g., related to a compact cluster of young OB and Wolf–Rayet stars), or provides evidence for the presence of an intermediate-mass ($\sim 10^3$–10^4 $M_\odot$) BH that may be the core of a globular cluster or dwarf spheroidal galaxy. Several such sources with luminosities up to 8×10^{40} erg/s are known [3, 45]. Here, we assume in our numerical study of the evolution of typical ULXs in close binaries with $L_x \sim 10^{38}$–10^{40} erg/s that the BHs have masses of 30 $M_\odot$.

To estimate the relation between the accretion rate and luminosity, we assume that $\sim 10^{20}$ erg is released per gram of matter accreted by the BH. However, three-dimensional hydrodynamic modeling of accretion onto a BH with a poloidal magnetic field shows that the efficiency of the transformation of the accreted rest mass into energy may be even higher than 50% [46]. This makes the relation between the accretion rate and X-ray luminosity of the system uncertain. An additional uncertainty is introduced if we allow for the possibility that the radiation is collimated. We adopt here the relation

$$L_x(\text{ erg/s}) = 6.3 \times 10^{45} \dot{M}_{acc}(M_\odot/\text{yr}) \qquad (2)$$

$$\approx 1.5 \times 10^{12} L_\odot \dot{M}_{acc}(M_\odot/\text{yr}),$$

assuming that the efficiency of the transformation of rest mass into energy is ~ 0.1. However, if there is a poloidal magnetic field in the accreted gas [46], the same X-ray luminosity may correspond to accretion rates that are almost an order of magnitude lower.

The integrated X-ray luminosity of massive Galactic binaries are $\sim 3 \times 10^{38}$ erg/s, while X-ray binaries with low-mass donors have luminosty of $\sim 3 \times 10^{39}$ erg/s [21]. These estimates correspond to integrated accretion rates of 5×10^{-8} and 5×10^{-7} $M_\odot$/yr for high- and low-mass X-ray sources, respectively.

A number of the models that we consider here assume that the X-ray emission of BHs arises during the gravitational capture of matter from the donor stellar wind in the Bondi–Hoyle regime [47]. Probably the best example of systems of this kind are symbiotic stars [48]. The capture radius is found from the energy-conservation law: $R = GM_{BH}/V_w^2$, where G is the gravitational constant and V_w is the wind speed, which is close to the escape speed at the donor surface: $V_w \approx (GM_d/R_d)^{1/2}$, where M_d and R_d are the mass and radius of the donor. As a result, we obtain the following estimate for the accretion rate:

$$\dot{M}_{BH} \approx \frac{1}{4}\left(\frac{M_{BH}}{M_d}\right)^2 \left(\frac{R_d}{A}\right)^2 \dot{M}_w, \qquad (3)$$

where A is the semimajor orbital axis and $\dot{M}_w$ is the mass-loss rate of the donor. Three-dimensional hydrodynamic numerical studies of accretion in symbiotic stars (which are analogs of the systems under consideration) confirm the validity of this relation [49, 50].

To estimate the number of ULXs produced via various scenarios, we must know the distributions of the mass of the primary (more massive) components M_{10}, semimajor orbital axes A_0, and component-mass ratios q of close binaries. We adopt the distribution from [51]:

$$d^3\nu(\text{ yr}^{-1}) = 0.2 d\log\left(\frac{A_0}{R_\odot}\right)\left(\frac{dM_{10}}{M_{10}^{2.5}}\right) dq, \qquad (4)$$

where M_{10} is in $M_\odot$ and $q = M_{20}/M_{10}$. Note that this expression is derived for our Galaxy. Let us now estimate the number of observed ULXs in the Galaxy. For ordinary spiral galaxies, $L_x/L_{opt} \approx 10^{-3}$ [9]. If we assume for the Galaxy $L_x = 2 \times 10^7 L_\odot$ and $dN/dL_x \sim L_x^{1.6}$ [8], then N_{ULX} (the number of ULXs in the Galaxy with luminosities ranging from $2.5 \times 10^4 L_\odot$ to $2.5 \times 10^6 L_\odot$) is ~ 100. If we take into account the observed dispersion of L_x/L_{opt}, this estimate of N_{ULX} is uncertain by about a factor of three. We must have an estimate of N_{ULX} in order to estimate the roles of various channels for the formation of ULXs in the Galaxy.

3. MODELS OF ULTRALUMINOUS X-RAY SOURCES

3.1. Accumulative Instability

In general, high mass-exchange rates ($\sim 10^{-8}$–10^{-6} $M_\odot$/yr) between the components of close binaries are not necessary to explain the observed high luminosities of ULXs. If the instability of the accretion disk has an accumulative nature, the average mass-flow rate into the disk can be lower than the rate noted above, as happens in cataclysmic variables [52]. The transient X-ray source XTE J1859+226 [53] shows that accumulative instability is also relevant for systems that contain a BH and solar-mass main-sequence dwarf. The orbital period of XTE J1859+226 is ~ 9.16 h [53]. As we show below, such a period does not imply a high mass-exchange rate. However, during its 1999–2000 outburst, the luminosity of the source became close to the Eddington limit for an accreting BH. Currently, 15 similar transients with quiescent-state luminosities of $\sim 10^{-2} L_\odot$ are known [54]. Thus, X-ray transients show that the ULX phenomenon is also possible in systems with relatively low average accretion rates.

3.2. *Formation of a Planetary Nebula in the Vicinity of a Black Hole*

The formation of a planetary nebula (PN) at the end of the evolution of a 0.8–8 $M_\odot$ star is accompanied by a superwind phase in the red-supergiant stage. This wind forms the envelope of the planetary nebula. The rate of mass loss in the superwind is $\sim 10^{-4}$ $M_\odot$/yr. When estimating the efficiency of this channel for the formation of ULXs, we must take into account the fact that a binary must be wide in order for a planetary nebula to form; i.e., its components must not overfill their Roche lobes and the semimajor axis of the orbit must exceed $\sim 2 \times 10^3 R_\odot$. As follows from (3), to obtain $\dot{M}_{BH} \approx 10^{-8}$–$10^{-6}$ $M_\odot$/yr for $M_d/M_{BH} \approx 0.1$, it is necessary to have $A \approx (10^5$–$10^6)R_\odot$. The distribution of wide binary systems over component-mass ratio in the range of interest (0.01–0.1) is virtually unknown because of obvious selection effects [51]. For our estimates, we shall assume that the fraction of systems with secondary masses of 1–8 $M_\odot$ and primary masses exceeding 50 $M_\odot$ is 0.1. Relation (4) can then be used to estimate the rate of formation for such systems: $\nu \approx 2 \times 10^{-5}$/yr. The superwind phase lasts for $\sim 10^4$ yr; this gives ~ 1 ULX produced via this planetary-nebula scenario. We conclude that this scenario is unimportant for the production of the observed ULXs.

3.3. *Accreting Single BHs in Dense Molecular Clouds*

Black holes are products of the evolution of stars with initial masses exceeding ~ 25 $M_\odot$ [29]. Relation (4) provides a lower limit for their total number in the Galaxy, $N_{BH} \sim 10^8$, since the rate of star formation was higher in the past [55]. As BHs travel through the Galaxy, some end up inside dense clouds of interstellar molecular hydrogen with densities $n_{\rm H} \sim 10^4$ cm^{-3}. The rate of accretion of this matter by a BH with speed V_{BH} is specified by the Bondi–Hoyle formula [47]: $\dot{M} = \pi\rho G^2 M_{BH}^2/V_{BH}^3$, where ρ is the density of the gas in the molecular cloud. We will assume that the fractional volume of molecular clouds is inversely proportional to $n_{\rm H}$. The resulting expression for the X-ray luminosity is $L_x/L_\odot \approx 10^{-3} n_{\rm H}(M_{BH}/M_\odot)^2 V_6^{-3}$, where V_6 is the BH speed in units of 10^6 cm/s. To estimate the minimum speed of the BHs, we shall assume that their speed distribution is Maxwellian with $\bar{V}_{BH}$ given by $n \sim N_{BH}(V/\bar{V}_{BH})^3$. A BH with the lowest spatial speed in the densest cloud should then have luminosity $L_x/L_\odot \approx 10^5 (M_{BH}/M_\odot)^2 (10^6/\bar{V}_{BH})^3$. It is evident that, if $\bar{V}_{BH} \lesssim 100$ km/s, some single BHs can attain the high luminosities typical for ULXs. This mechanism would also be able to explain the concentration of ULXs in spiral arms, which harbor most of the molecular clouds in a spiral galaxy.

3.4. *Accretion from Massive Disks around BHs*

During the evolution of close binaries with massive BHs, there are at least two situations when a Roche-lobe filling companion to a BH can be disrupted over the orbital time scale: when the companion to the BH is a convective main-sequence star with $M \lesssim 0.5$ $M_\odot$ [56] or a degenerate dwarf. Stars of these two types expand in response to rapid mass loss. If angular momentum is rapidly and efficiently exchanged between the rotational and orbital motion, the increase in the semimajor axis of the orbit is compensated for by expansion of the donor, supporting stable mass exchange. However, when the rate of angular-momentum exchange is low, disruption of the donor over the orbital time scale becomes inevitable. As a result, a single BH surrounded by a massive gaseous disk appears. The absence of W UMa stars with $q \lesssim 0.1$ [57] may provide evidence for such disruption of BH companions.

Little is known about the further evolution of such objects. X-ray emission will be absent in the absence of accretion viscosity. Otherwise, the rate of formation of such objects, $\sim 10^{-4}$/yr [43], and the mass of the disks, ~ 0.5 $M_\odot$, provide an estimate of the total X-ray luminosity of the Galaxy due to these objects: $L_x \approx 10^8 L_\odot$. The optical luminosity of the Galaxy is $L_{opt} \approx 3 \times 10^{10} L_\odot$, so that $L_x/L_{opt} \approx 1/300$. This ratio does not contradict observational estimates, $L_x/L_{opt} \approx 10^{-4}$–$10^{-2}$ [9, 58, 59]. If we allow for the inevitable evaporation of some fraction of the disk material, the theoretical estimate will be decreased, while remaining within the limits given by observations.

3.5. *Supernova Remnants in a Dense Interstellar Medium*

The deceleration of supernova envelopes in a dense interstellar medium generates shocks and strongly heats the gas. For an expansion speed of several thousands of km/s, the energies of the photons cooling the gas reach several keV [60], and the corresponding luminosities reach 10^{41} erg/s [61, 62]. The Crab nebula demonstrates a realization of this scenario. If the average kinetic energy of supernova envelopes is $\sim 10^{50}$ erg and their luminosities are $\sim 10^{39}$–10^{40} erg/s [63–65] (typical for bright ULXs), the lifetimes of associated ULXs should be 300–3000 yr. For the supernova rate in our Galaxy, $\nu \sim 10^{-2}$/yr, the implied number of ULXs is 3–30. However, it is clear that only supernovas that exploded in dense molecular clouds could be manifest as ULXs. This is possible for type II supernovae, but it is more likely that type Ia supernovae will be in a hot interstellar medium, where the energy is spent on accelerating the Galactic wind [66]. Another distinctive property of ULXs associated with supernovae would be constancy of their brightness. However, most observed ULXs are variable [3], so that this model can be ruled out, at least for variable ULXs.

3.6. Intermediate-mass BHs ($M_{BH} \approx 10^2$–$10^5\ M_\odot$)

It is well known that there is a gap between stellar-mass BHs (5–14 $M_\odot$) and the BHs in the nuclei of galaxies (10^4–$10^{10}\ M_\odot$) [20, 67]. This gap can be partially filled by BHs originating from stars with masses as high as $\sim$100 $M_\odot$, which have not yet been observed because of their scarcity. The first information on BHs in the cores of globular clusters has recently became available [14, 15, 68]. The existence of such BHs makes possible high X-ray luminosities for the cores of globular clusters if the accretion is sufficiently efficient. It is interesting that the ULXs in the bulge of M31 are brighter than those in its disk, consistent with this possibility. Another possible origin for the high luminosity of ULXs in the spherical component of the galaxy may be high masses for BHs formed from low-metallicity stars with relatively weak stellar winds.

Intermediate-mass BHs in globular clusters probably form via a two-stage mechanism for the deceleration of stellar-mass (10–100 $M_\odot$) BHs that are produced by the most massive stars of the clusters. In the first stage, the BHs "sink" into the central regions of the cluster, to the vicinity of the central BH, due to dynamical friction. This process concentrates the X-ray sources in globular clusters in their central regions [44]. In the second stage, gravitational radiation by the "stellar BH + central BH" pair results in their merger, increasing the mass of the central BH by up to $\sim 10^{-3}$ of the total mass of the globular cluster [31, 69]. ULXs are, in fact, observed in globular clusters [17, 70]. An efficient donor is required to support the high luminosity of an intermediate-mass BH. A nearby planetary nebula, red supergiant, or degenerate dwarf could serve as such a donor. Note that dynamical deceleration of globular clusters in their galaxies may be one reason for the appearance of supermassive (10^4–$10^6\ M_\odot$) BHs in the nuclei of galaxies.

3.7. BHs in Close Binaries with Degenerate Donors

The evolution of massive close binaries with large initial component-mass ratios can lead to the formation of semidetached systems with degenerate donors via the action of gravitational radiation. The BHs can have helium, carbon–oxygen, or even oxygen–neon white-dwarf companions [71]. The Galactic rate of formation of systems with helium-dwarf companions can be estimated from (4) to be $\sim 3 \times 10^{-4}$/yr, while the estimated rate of formation of systems with carbon–oxygen companions is $\sim 3 \times 10^{-5}$/yr [43]. The estimated number of such systems in the Galaxy (300–3000) is certainly higher than the number of observed ULXs. The most probable way to avoid "overproduction" of the X-ray luminosity of ULXs associated with these systems is disruption of the degenerate dwarfs and their transformation into massive disks. The formation of common envelopes or intense stellar winds driven by super-Eddington radiation may also appreciably reduce theoretical estimates of the X-ray luminosity and number of such systems [72].

To illustrate this model, we computed the evolution of a binary system with a degenerate helium donor with an initial mass of 0.3 $M_\odot$ and a 30 $M_\odot$ BH accretor (as in all other tracks). The method used to carry out the evolutionary computations of a close binary with an induced stellar wind (ISW) from the donor and our evolutionary code are described in detail in [56, 73]. The ISW is a result of the irradiation of the donor by hard radiation from the accreting neutron star or black hole. When the ISW is taken into account, mass exchange becomes possible in detached systems in which the donor does not fill its Roche lobe.

Parameters of all the tracks are listed in the table. The track for the system indicated above in a plot of orbital period versus mass-loss rate is shown in Fig. 2. This figure clearly shows that, in the initial stage of the evolution, the excess of the donor mass-loss rate over the Eddington limit is high and can result in the formation of a common envelope and disruption of the donor. The ISW leaves the evolution of systems with degenerate donors nearly unaffected.

3.8. BHs with Nondegenerate Low-mass 0.4–1 $M_\odot$ Helium Companions

If the initial mass of the secondary in a massive close binary is $M = 3$–$10\ M_\odot$, a nondegenerate helium star with a mass of $0.06(M/M_\odot)^{1.57}\ M_\odot$ [74] is formed after the common-envelope stage. For helium stars with masses of 0.4–1 $M_\odot$ and $A = 0.4$–$0.8\ R_\odot$, the rate of mass exchange in semidetached systems driven by gravitational radiation can reach

Parameters of computed tracks for binaries with 30 $M_\odot$ accretors

Track number	Mass-exchange regime	$(M_2)_0$, $M_\odot$	D	P_0, day	τ(ULX), yr	M_{acc}, $M_\odot$	$(M_2)_f$, $M_\odot$	m_{He}	m_{CO}	P_f, day	t_f, 10^9 yr
1	with ISW	1.0	1.00	0.32	2.2×10^6	0.49	0.44	–	–	2.08	15.0
2	with ISW	1.0	0.30	1.93	–	0.13	0.63	–	–	2.92	15.0
3	with ISW	1.0	0.20	3.55	–	0.07	0.69	–	–	4.48	15.0
4	with ISW	1.0	0.10	10.1	–	0.51	0.31	0.99	–	173	12.5
5	with ISW	1.0	0.05	28.6	–	0.52	0.40	0.98	–	338	12.6
6	with ISW	1.0	0.03	61.5	3.4×10^6	0.48	0.45	0.94	–	533	12.7
7	with ISW	1.0	0.01	319	8.9×10^5	0.18	0.80	0.57	–	589	12.7
8	without ISW	1.0	1.00	0.32	–	0.99	0.008	–	–	0.16	15.0
9	without ISW	1.0	0.30	1.93	–	0.99	0.01	–	–	0.09	15.0
10	without ISW	1.0	0.20	3.57	2.1×10^5	0.67	0.33	0.98	–	63.2	12.7
11	without ISW	1.0	0.10	10.1	4.0×10^6	0.62	0.37	0.98	–	166	12.7
12	without ISW	1.0	0.03	61.5	1.3×10^7	0.51	0.45	0.96	–	569	12.7
13	with ISW	5.0	1.00	0.71	2.0×10^7	2.14	0.25	0.95	–	65.1	7.5
14	with ISW	5.0	0.50	2.00	1.9×10^7	2.47	0.60	0.80	–	185	0.21
15	with ISW	5.0	0.30	4.31	4.3×10^5	0.13	3.23	0.15	–	12.5	0.09
16	without ISW	5.0	1.00	0.71	4.1×10^7	3.02	0.66	0.69	–	213	0.12
17	without ISW	5.0	0.50	2.00	3.4×10^5	0.31	2.62	0.14	–	12.0	0.12
18	without ISW	5.0	0.30	4.31	8.3×10^3	0.06	3.53	0.15	–	11.8	0.12
19	with ISW	10.0	1.00	0.85	4.7×10^7	3.56	0.80	0.72	–	171	0.05
20	with ISW	10.0	0.50	2.41	3.3×10^6	0.21	2.63	0.41	–	74.7	0.02
21	with ISW	10.0	0.30	5.18	1.4×10^4	0.02	2.14	0.65	–	408	0.04
22	without ISW	10.0	1.00	0.85	2.6×10^7	4.51	1.68	0.67	–	100	1.26
23	without ISW	10.0	0.50	2.41	–	0.05	2.11	0.59	–	174	0.05
24	without ISW	10.0	0.30	5.18	–	0.01	2.14	0.63	–	399	0.05
25	with ISW	0.5	0.50	0.05	3.8×10^6	0.49	0.007	–	–	1.67	15.0
26	with ISW	0.3	1.00	0.002	9.6×10^6	0.13	0.001	–	–	0.02	2.25
27	with ISW	30.0	0.90	0.18	–	0.26	10.3	–	0.74	0.39	0.001
28	with ISW	30.0	0.30	0.91	–	0.11	10.5	–	0.66	2.00	0.001
29	with ISW	30.0	0.10	4.72	–	0.01	10.5	–	0.75	10.4	0.001
30	with ISW	30.0	1.00	1.19	1.7×10^6	2.13	5.83	0.95	–	23.2	0.01
31	with ISW	30.0	0.40	4.70	7.4×10^5	0.08	8.58	–	0.59	37.4	0.01
32	with ISW	30.0	0.10	37.6	–	0.06	12.2	0.80	–	169	0.008

$(M_2)_0$ is the initial mass of the donor; D, the initial ratio of the donor radius and mean Roche-lobe radius; P_0, the initial orbital period; τ(ULX), the duration of the evolutionary stage when the binary is a ULX (i.e., when the accretion rate is higher than 2×10^{-8} $M_\odot$/yr and the rate of mass loss by the donor is lower than 10^{-6} $M_\odot$/yr); M_{acc}, the amount of mass accreted by the BH during its evolution; $(M_2)_f$, the mass of the donor at the end of the evolutionary track; m_{He}, the relative mass of the helium core of the donor at the end of the track; m_{CO}, the relative mass of the carbon–oxygen core of the donor at the end of the track; P_f, the orbital period at the end of the track; and t_f, the age of the system at the end of the track. For tracks 1–24, the donor is initially a main-sequence star; for track 25, it is a nondegenerate helium star; for track 26, a degenerate helium dwarf; for tracks 27–29, a Wolf–Rayet star; and for tracks 30–32, an O star.

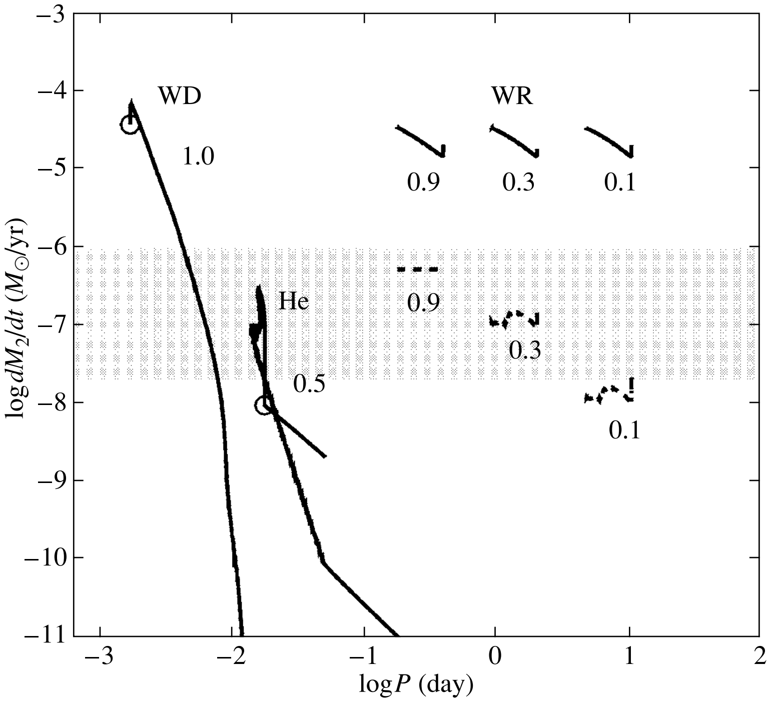

Fig. 2. Logarithm of the orbital period plotted against logarithm of the donor's mass-loss rate for binary systems containing 30 $M_\odot$ black holes and three types of donors: a 0.3 $M_\odot$ degenerate helium dwarf (WD), a 0.5 $M_\odot$ nondegenerate helium star (He), and a 30 $M_\odot$ Wolf–Rayet star. We show both the mass-loss rate (solid curves) and mass-exchange rate (dashed curves) for the Wolf–Rayet star. The tracks take into account the induced stellar wind. The numbers by the tracks indicate the initial fraction of the Roche lobe filled by the donor D. Open circles mark times of Roche-lobe overflow. The broad gray strip shows the range of BH accretion rates that correspond to the model for the ULXs.

$\sim 10^{-7}$ $M_\odot$/yr and L_x can reach $\sim 10^{39}$ erg/s [56]. The parameters of the initial systems given above can be used to estimate the Galactic rate of formation of such ULXs and their number via (4). If $\Delta \log A \approx 0.3$, $\Delta q \approx 0.1$, and the mass-exchange timescale is 10^6 yr, then $\nu \approx 3 \times 10^{-5}$/yr, and $N \approx 30$. The realization of this scenario requires a common-envelope phase in a system containing a BH and a 3–6 $M_\odot$ giant. However, we cannot rule out the possibility that the stellar wind induced by the X-ray radiation of the BH prevents Roche-lobe overflow by the donor, closing this channel for the formation of ULXs.

We computed the evolution of a binary that initially contains a 0.5 $M_\odot$ helium nondegenerate donor. The evolutionary track for this system is shown in Fig. 2. The ISW influences the evolution of this type of system only weakly: the only difference from the evolution without the ISW is an evolutionarily insignificant mass loss in the semidetached stage. As Fig. 2 shows, the rate of mass loss by the nondegenerate helium star can reach the Eddington limit.

3.9. Wolf–Rayet Stars with BH Companions

Wolf–Rayet (WR) stars have strong stellar winds that may be driven by pulsations [29, 75]. The mass-loss rate is $\dot{M}_{WR} \approx 10^{-6}(M_{\rm WR}/M_\odot)^{1.3} M_\odot$/yr [76, 77]. Some fraction of the lost matter can be captured by the nearby BH [see (3)]. If the Wolf–Rayet star is a 10–30 $M_\odot$ pure helium star, its radius is given by the relation $R_{\rm WR}/R_\odot \approx 0.2(M_{\rm WR}/M_\odot)^{0.6}$ [40]. Assuming for our estimates $M_{\rm WR} = M_{BH} = M$, we obtain for the accretion rate $\dot{M}_{acc}(M_\odot/{\rm yr}) \approx 10^{-9.5}(M/M_\odot)^{1.83} P_{orb}^{-4/3}$, where P_{orb} is in days. The mass-loss rate will be maximum when the Wolf–Rayet star fills its Roche lobe: $\dot{M}_{acc} \approx 10^{-7.4}(M/M_\odot)^{1/3} M_\odot$/yr.

The birthrate of ULXs in this scenario can be obtained using (4), specifying $\Delta \log A \approx 0.3$, $\Delta q \approx 0.4$ and the timescale for helium burning in the core of the star, $\sim 5 \times 10^5$ yr. Then, $\nu \approx 10^{-4}$/yr and $N \approx 50$. The expected orbital periods of such systems range from several hours to several days. It is interesting that the collapse of a Wolf–Rayet core into a BH can produce γ-ray bursts in the closest systems of this type [77, 78].

The first WR+BH system was probably discovered in the galaxy IC 10 [79]. The position of the brightest X-ray source in this galaxy coincides with the position of a Wolf–Rayet star. Estimates show that absorption of X-rays by the stellar wind of this star is negligible in this case [80]. In our Galaxy, this family of binaries is represented by the Cygnus X-3 system, which contains a $\sim 17\ M_\odot$ BH and a Wolf–Rayet star [81, 82]. It is possible that the ULX Cyg X-1, with an orbital period of ~ 8 h [83], also belongs to this family.

Figure 2 shows evolutionary tracks for close binaries with Wolf–Rayet donors with an initial mass of 30 $M_\odot$, computed taking into account the stellar wind and assuming various initial ratios of the donor radius and the mean Roche-lobe radius (filling factor), D. The evolution was followed up to the depletion of helium in the donor core. The rate of mass exchange in these systems is determined by the fraction of the stellar wind that can be captured by the BH, which increases with D. For D close to unity, the accretion rate becomes close to the Eddington limit and L_x approaches 10^{40} erg/s.

3.10. O Stars with BH Companions

O stars also have strong stellar winds, whose rates have been estimated to be $\dot{M}_{\rm O} \approx 10^{-12.4} \times (M_{\rm O}/M_\odot)^4 M_\odot$/yr [76, 77, 84]. Some fraction of this wind can be captured by the nearby BH [see (3)]. Let us find the relation between the orbital period and accretion rate. If we suppose that the radius of the O star is $R_{\rm O}/R_\odot \approx 2(M_{\rm O}/M_\odot)^{0.45}$ [40] and its mass is $M_{\rm O} = M_{BH} = M$, then $\dot{M}_{acc}$ ($M_\odot$/yr) $\approx 10^{-13.8}(M/M_\odot)^{4.23} P_{orb}^{-4/3}$, where P_{orb} is in days. Since the radii of main-sequence O stars provide a lower limit for P_{orb}, $P = (M_{\rm O}/M_\odot)^{0.18}$, the maximum accretion rate is limited to $\dot{M}_{acc} \lesssim 10^{-13.8} \times (M/M_\odot)^4\ M_\odot$/yr. The appearance of a ULX requires $\dot{M}_{acc} \gtrsim 10^{-8}\ M_\odot$/yr. This requires a $\sim 40\ M_\odot$ O companion that is very close to the BH. However, due to their strong stellar wind, solar-composition O stars with masses exceeding $\sim 50\ M_\odot$ do not expand after the formation of their helium cores [24, 25, 84]. Therefore, the semimajor orbital axes in such systems increase in the course of their evolution, but the possibility of forming a ULX remains due to the enhanced stellar wind. However, the winds of low-metallicity stars become weaker, and the range of masses permitting the formation of ULXs broadens. Possible examples of ULXs of this type include an object in M81 with $L_x = 2 \times 10^{39}$ erg/s and an orbital period of two days and an object in IC 342 with an orbital period of 30–40 h [5]. Another possible example of an eclipsing system of this type is an X-ray binary X-7 in M33 with $P_{orb} \approx 3.45$ day and $L_x \approx 10^{38}$ erg/s [86].

It is interesting that some ULXs of this type demonstrate the action of accumulative instability. One of the closest well-studied sources is X-1 in IC 342, in which a supernova remnant with an age of $\sim 10^5$ yr surrounds a variable ULX with a luminosity of $(3-10) \times 10^{39}$ erg/s in a close binary with a BH. A $\sim 18\ M\odot$ O8V star was discovered at the position of the variable ULX X-11 in M81, which has $L_x \approx 10^6 L_\odot$ [85], but the expected periodicity of the optical and X-ray emission has not been detected.

To illustrate this model, we computed the evolution of a binary system with an O-star (i.e., a main-sequence star with an initial mass of 30 $M_\odot$) donor. Tracks for various initial Roche-lobe filling factors D taking into account the ISW and the stellar wind of the O star are shown in Fig. 3. The stellar wind of the O star governs the evolution of these systems as long as the system is detached; however, due to its nuclear evolution, the donor rapidly fills its Roche lobe and the mass-loss rate increases by almost three orders of magnitude. Thus, we conclude that the donor mass-loss rates in these systems are too large for them to be ULXs for appreciable periods of time.

3.11. BHs with Main-sequence B Companions (5–10 $M_\odot$)

For typical masses of the main-sequence B companions of 5–10 $M_\odot$, the rate of mass exchange regulated by the nuclear evolution of the B star should be $\sim 10^{-10}(M/M_\odot)^4\ M_\odot$/yr. Therefore, Roche-lobe filling B stars are good candidates for ULX donors. The discovery of an optical star at the position of a ULX in the spiral galaxy NGC 1313 [87] opens possibilities for the observational verification of this scenario. The system X-2 in NGC 1313 [87], with a 10 $M_\odot$ optical component and unknown orbital period, probably belongs to this same class. The object J1819.3-2525, which has an orbital period of 2.82 day and contains a $\sim 10\ M_\odot$ BH and a $\sim 7\ M_\odot$ B star, may be a similar ULX.

To estimate the number of potential ULXs of this kind, let us assume that $M_{10} = 25\ M_\odot$, $\Delta \log A \approx 0.3$, and $q \approx 0.1$. Then, according to (4), the birthrate of such ULXs is $\nu \approx 3 \times 10^{-5}$/yr and their expected number in the Galaxy for a mass-exchange time interval of $\sim 10^7$ yr is ~ 300. This makes such ULXs the most abundant type in galaxies with continuous star formation that can provide a supply of 5–10 $M_\odot$ donors [88].

Figures 4 and 5 show tracks for systems with donors with initial masses of 5 and 10 $M_\odot$ computed for various D values and two evolutionary models (with and without the ISW). The influence of the ISW is important only when the initial D values are sufficiently high, while the tracks for $D \approx 0.1$ with and without the ISW are nearly identical: the dominant

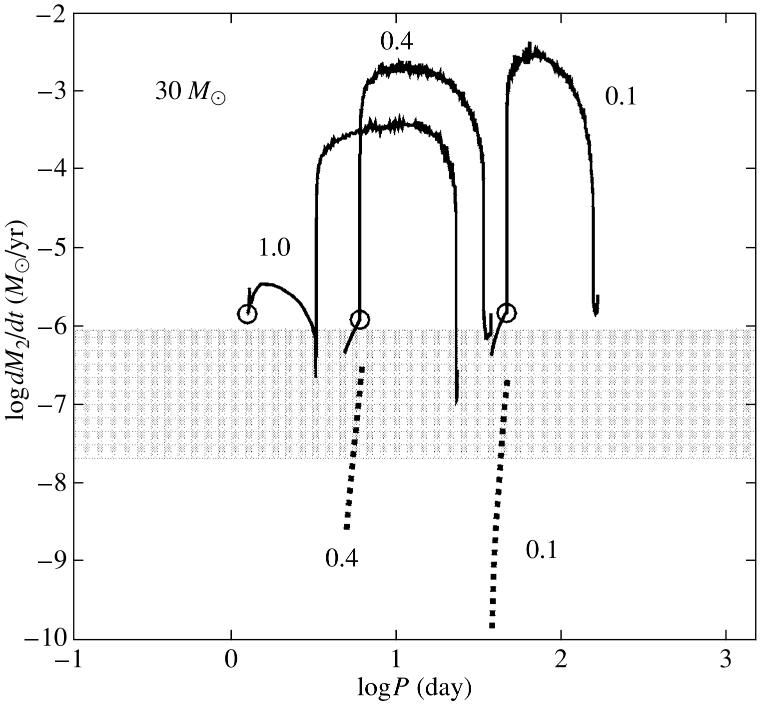

Fig. 3. Logarithm of the orbital period plotted against the logarithm of the donor's mass-loss rate for binary systems containing 30 $M_\odot$ black holes and 30 $M_\odot$ O donors. For the two tracks with initial Roche-lobe filling factors $D < 1$, the rate of mass exchange with the BH before Roche-lobe overflow is also shown (dashed curves). The tracks were computed taking into account the induced stellar wind. The values of D are indicated next to the tracks. The open circles mark times of Roche-lobe overflow. The broad gray strip shows the range of accretion rates by the BH that correspond to the ULX model.

role in the evolution of the system is played by mass loss by the evolved donor after it fills its Roche lobe. Our computations show that the mass-loss rate is much higher than the Eddington limit, with both this excess and the duration of the stage when it exists increasing with the initial donor mass. However, among all the tracks for high mass-loss rates, only track 14 for the 5 $M_\odot$ donor and $D = 0.5$ satisfies the ULX model, since the formation of a common envelope is expected for the remaining tracks, which may considerably shorten the ULX stage and decrease the number of ULX sources.

3.12. Low-mass (0.3–1.5 $M_\odot$) Stars with BH Companions

The large number of observed systems of this kind with known parameters [29] and the "cosmological" lifetimes of the donors makes them attractive candidates for ULXs in old stellar populations: elliptical galaxies and the bulges of spherical systems (Fig. 1). The evolution of the closest systems of this kind is determined by the magnetic stellar wind of the donor, which arises in the presence of a convective envelope and radiative core [56]. However, the magnetic stellar wind is unable to support mass-exchange rates higher than 3×10^{-8} $M_\odot$/yr (Fig. 6). In addition, an appreciable fraction of the donor mass is lost via the ISW. In wider systems, the mass exchange is determined mainly by the evolutionary expansion of the donor with its degenerate helium or carbon–oxygen core if initial mass of the donor is 0.8–2.5 $M_\odot$. The radius of the donor in these stars depends only on the mass of the core [51]. The formation of the carbon–oxygen core shortens the timescale for the star's evolution to $\sim 10^6$ yr. The corresponding mass-exchange rate, $\sim 10^{-6}$ $M_\odot$/yr, is sufficient for the appearance of a ULX if the accretor is a sufficiently massive BH.

When considering this scenario, we must consider the survival of a low-mass donor during the evolution of the BH progenitor. If the initial mass of a solar-composition primary exceeds $M_{10} \sim 50$ $M_\odot$, the red-supergiant phase is absent due to the effect of the strong stellar wind [24]. This enables the survival of the companion. According to the formalism for describing common envelopes presented in [43], the semimajor orbital axes of systems with $M_{10} =$ 25–50 $M_\odot$ are decreased by nearly a factor of 100. This excludes the possibility of transforming their donors into red supergiants and so prevents these systems from becoming candidate ULXs.

To estimate the number of potential ULXs of this type, we must estimate the number of secondary

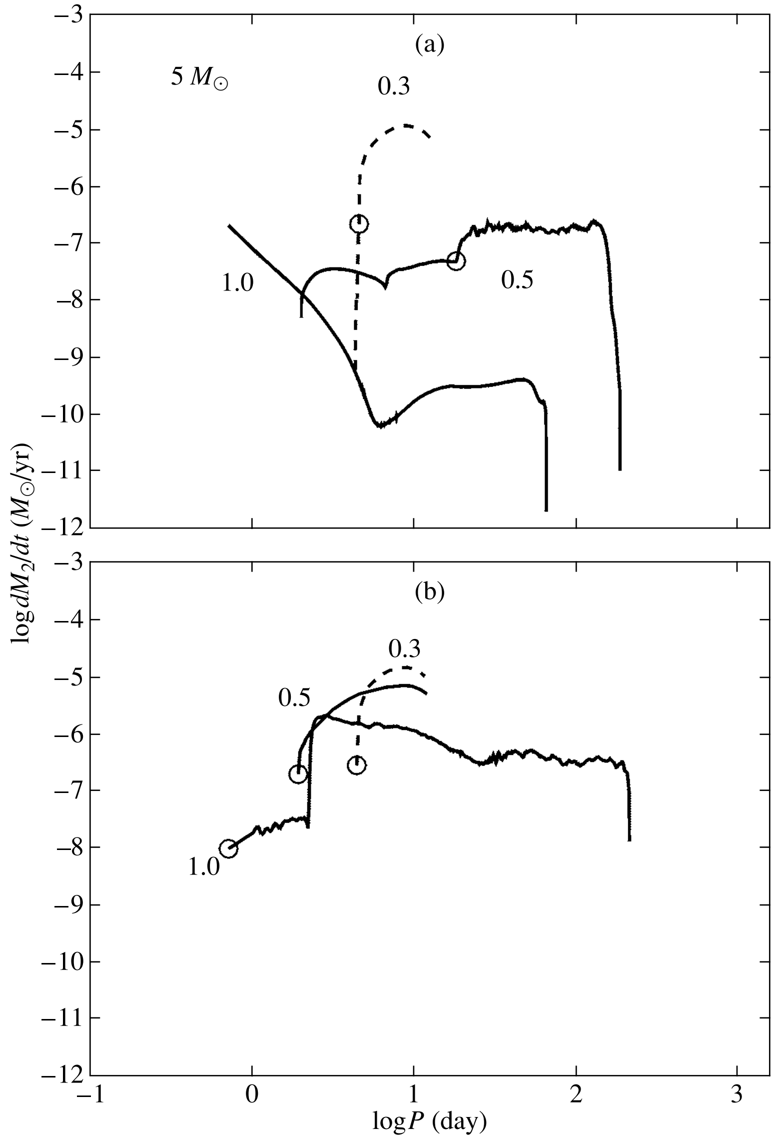

Fig. 4. Logarithm of the orbital period plotted against the logarithm of the donor's mass-loss rate for binary systems containing 30 $M_\odot$ black holes and 5 $M_\odot$ main-sequence donors. The tracks in panel (a) and (b) were computed with and without taking into account the induced stellar wind. The initial Roche-lobe filling factors D are indicated next to the tracks. (For clarity, tracks with different D values are sometimes drawn using different line styles in this and following figures.) The open circles mark times of Roche-lobe overflow. The broad gray strip shows the range of accretion rates by the BH that correspond to the ULX model.

components that become red supergiants. This is approximately equal to $\tau^2/3T_\mathrm{H}$, where τ is the lifetime of red supergiants and T_H is the Hubble time. We can estimate the lifetime of the corresponding ULXs as $\sim 10^7$ yr if the mass-exchange rate is $\sim 10^{-7}$ $M_\odot$/yr. Assuming $M_{10} \gtrsim 50$ $M_\odot$ and $\Delta \log A \approx 1$, we find using (4) that $N \approx 10^{-14}\tau^2$; i.e., we obtain only one source per galaxy similar to our own. However, some ULXs in elliptical galaxies may belong to this class. Long series of observations may reveal such ULXs as eclipsing binaries.

The tracks for systems with main-sequence donors with initial masses of 1 $M_\odot$ computed for various D values and two evolutionary models (with and without the ISW) are shown in Fig. 6. These computations show that high mass-exchange rates, approaching the Eddington limit for massive BHs, are possible only for low initial Roche-lobe filling factors. In this case, the mass exchange starts after the donor has sufficiently expanded in the course of its evolution. However, even then, the mass-loss rate is usually below the Eddington limit. Track 7 for $D = 0.01$ (computed with the ISW), for which the donor mass-loss rate experiences a sharp increase after the relative

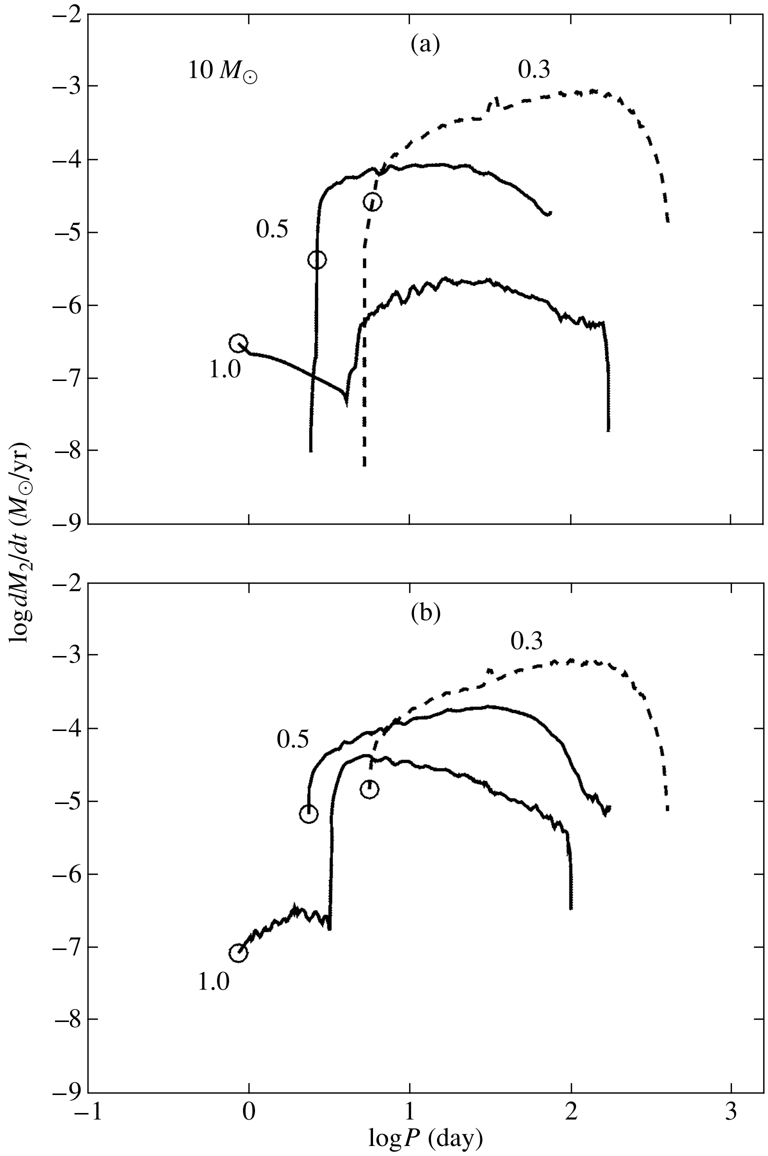

Fig. 5. Same as Fig. 4 for a 10 $M_\odot$ main-sequence star.

mass of its core becomes 0.57, is of interest. A probable outcome of this increase in the mass-loss rate is the formation of a common envelope.

3.13. Expanding Hertzsprung-gap Stars with BH Companions

A donor with a mass greater than $\sim 2.5\ M_\odot$ that expands when it crosses the Hertzsprung gap over the thermal time scale for its envelope T_{KH} is able to support the mass-exchange rate necessary for a ULX. Since the density in the donor envelope decreases as e^{r/H_P}, where r is the distance from the center of the star and H_P is the pressure scale height, the typical lifetime of the corresponding ULXs will be close to $T_{KH}H_P/R$, where R is the stellar radius. This lifetime will be close to $kTM/\mu L$, where L is luminosity of the donor, T is the temperature of its envelope, and μ is the molecular weight of the envelope material. Assuming $T = 10^4$ K, we obtain for the lifetime of the ULX $\tau \approx 3 \times 10^4 (M_\odot/M)^3$ yr. It is clear that systems with $\sim 2.5\ M_\odot$ will have the longest lifetimes. Relation (4) implies that several ULXs of this kind may exist in our Galaxy. Note that the existence of such ULXs is possible only in relatively young stellar clusters, with ages below $\sim 10^9$ yr. There should not be any ULXs of this kind in elliptical galaxies.

4. CONCLUSIONS

The aim of this study was to investigate the evolutionary status of ULXs associated with close binaries

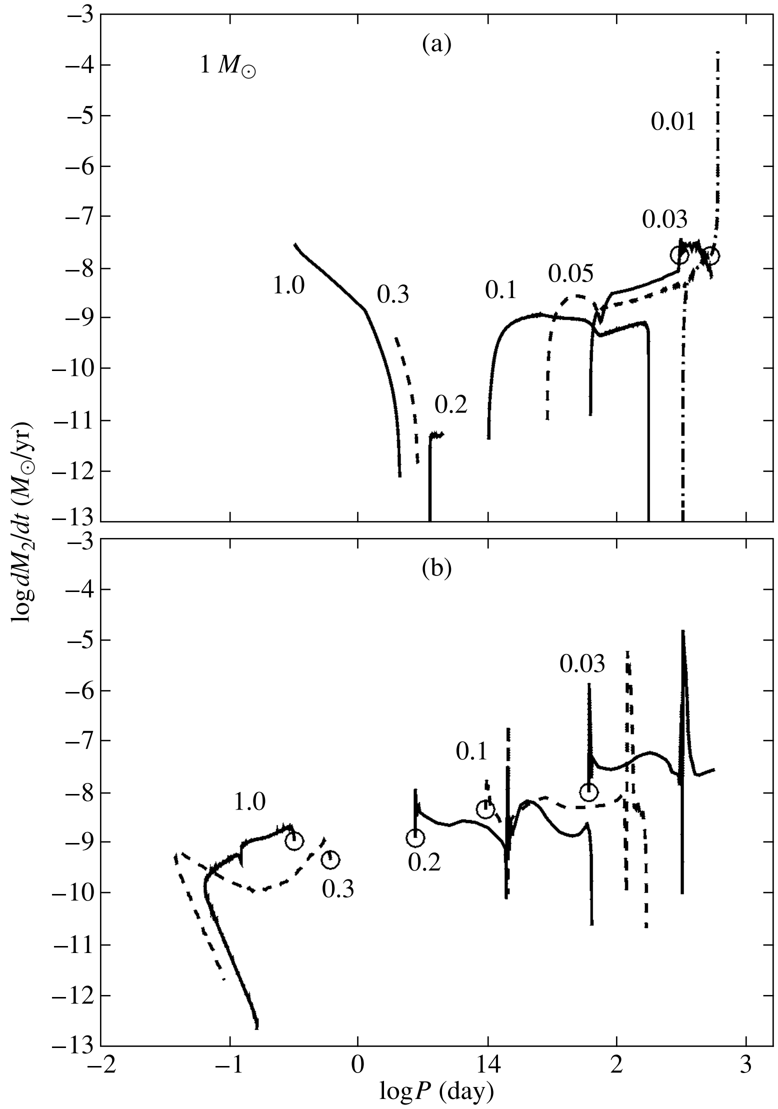

Fig. 6. Same as Fig. 4 for a $1\,M_\odot$ donor.

whose primaries exceed $\sim 25\ M_\odot$ and form BHs at the end of their evolution. The masses of the resulting BHs can be as high as ~ 40–$100\ M_\odot$. The formation of the most massive BHs is facilitated by a low metallicity. Intermediate-mass (10^3–$10^4\ M_\odot$) BHs can form as a result of dynamical friction of stellar BHs in the cores of globular clusters. In principle, they can explain the origin of the brightest ULXs with $L_x \gtrsim 10^{40}$ erg/s. However, such ULXs could also arise as a result of the collimation of the radiation of accreting stellar BHs.

ULXs can be separated into three types: extended regions of hot gas, accreting single BHs in dense molecular clouds, and close binary systems containing massive (~ 40–$100\ M_\odot$) BHs and donors with various masses. Sources of the first type include supernova remnants in a dense interstellar medium and gas that is heated by collisions of intergalactic gaseous clouds or by collisions of small satellite galaxies with the gaseous disk of a giant galaxy. The second group of objects comprises intermediate-mass BHs that accrete from a dense gaseous medium. This group may include intermediate-mass BHs in the nuclei of globular clusters or galaxies, as well as stellar BHs that have ended up in dense molecular clouds, facilitating a high accretion rate. The formation of intermediate-mass BHs is probably not a consequence of the accretion of interstellar gas and instead results from the accumulation of stellar BHs in globular clusters, which first lose energy due to tidal friction, then form binaries that merge due to their gravitational radiation.

However, most ULXs are close binaries contain-

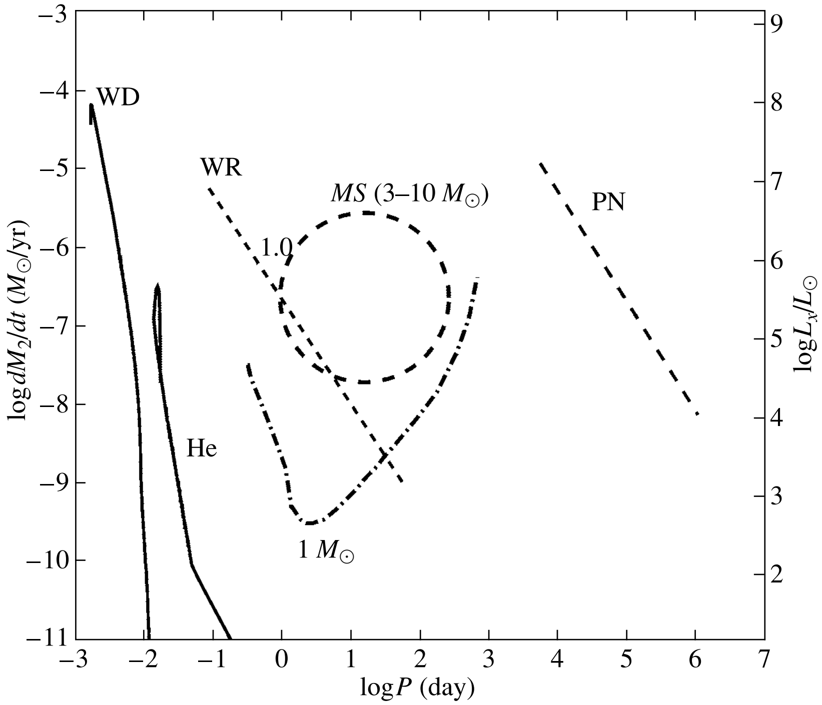

Fig. 7. Logarithm of the orbital period plotted against the logarithm of the donor's mass-loss rate, summarizing the results of the evolutionary computations for close binary systems containing 30 $M_\odot$ black holes and donors of various types. The solid curves show the tracks for degenerate dwarfs (WD) and nondegenerate helium stars (He). The dashed curves show the positions of systems with Wolf–Rayet (WR) and planetary-nebula (PN) donors. Semidetached systems with 3–10 $M_\odot$ main-sequence donors are located inside the dashed circle. The dash–dot curve shows the upper limit for the mass-exchange rate in systems with solar-mass donors that overflow their Roche lobes at various stages of their evolution. The broad gray strip shows the range of accretion rates by the BH that correspond to the ULX model.

ing a stellar BH and a companion. Figure 7 presents a sketch of all the close-binary ULXs with mass exchange that we have studied, indicating the range of accretion rates that corresponds to ULXs.

Since ULXs are well represented in both young and old stellar populations (i.e., in both spiral and elliptical galaxies), several models are necessary to explain their origin. The most promising models for young stellar populations seem to be those in which a BH has a close Wolf–Rayet or ~7 $M_\odot$ Roche-lobe-filling main-sequence companion. In the former case, the mass exchange and X-ray luminosity are supported by the accretion of some fraction of the Wolf–Rayet's stellar wind; in the latter case, they are supported by the nuclear evolution of the donor.

Several possible explanations of the existence of ULXs in elliptical galaxies are suggested, which can, of course, also be realized in spiral galaxies with well-represented old populations. In these cases, ULXs can contain BHs with low-mass degenerate helium dwarf companions or with a massive disk that is produced by the disruption of a massive degenerate dwarf companion. In the former case, the evolution is determined by gravitational radiation, while, in the latter case, the dominant role is played by the viscosity of the disk material. BHs in elliptical galaxies can also be fed by Roche-lobe-filling low-mass (super)giants with degenerate helium cores. However, after careful examination of the observed distribution of ULXs in 28 elliptical and S0 galaxies [89], we cannot rule out the possibility that ULXs with X-ray luminosities exceeding 2×10^{39} erg/s ($\dot{M}_{acc} > 3 \times 10^{-7}\ M_\odot$/yr) are absent in such galaxies. This may mean (Fig. 6a) that systems with nondegenerate solar-mass donors fully account for the range of observed X-ray luminosities in these galaxies.

Our analysis has shown that binaries containing BHs and with relatively low mass-exchange rates can also be manifest as ULXs if the system's accretion disk is subject to accumulative instability. This implies that ULXs may be transient. The identification of observed ULXs with the various models suggested in this paper requires systematic observations with good time resolution, to enable discrimination between the models. Ultraluminous sources in close binaries can be discovered via the presence of periodic X-ray eclipses.

ACKNOWLEDGMENTS

This work was supported by a grant of the President of the Russian Federation, the Federal Scientific and Technological Program "Astronomy," and the Russian Foundation for Basic Research (project no. 03-02-16254).

REFERENCES

1. G. Fabbiano, Astrophys. J. **330**, 672 (1988).
2. G. Fabbiano, A. Zezas, and S. Murray, Astrophys. J. **554**, 1035 (2001).
3. E. Colbert and A. Ptak, Astrophys. J., Suppl. Ser. **143**, 25 (2002).
4. Y. Gao, Q. Wang, P. Appleton, and R. Lucas, astro-ph/0309253 (2003).
5. M. Sugiho, J. Kotoku, K. Makishima, *et al.*, Astrophys. J. Lett. **561**, L73 (2001).
6. J.-F. Liu, J. N. Bregman, J. Irwin, *et al.*, Astrophys. J. Lett. **581**, L93 (2002).
7. T. Roberts and G. Colbert, Mon. Not. R. Astron. Soc. **341**, L49 (2003).
8. H. Grimm, M. Gilfanov, and R. Sunyaev, Mon. Not. R. Astron. Soc. **339**, 793 (2003).
9. A. Shapley, G. Fabbiano, and P. Eskridge, Astrophys. J., Suppl. Ser. **137**, 139 (2001).
10. E. Colbert, T. Heckman, A. Ptak, *et al.*, astro-ph/0305476 (2003).
11. L. Angelini, M. Loewenstein, and R. Mushotzky, Astrophys. J. Lett. **557**, L35 (2001).
12. N. Masetti, L. Foschini, L. Ho, *et al.*, astro-ph/0305452 (2003).
13. P. Humphreys and G. Fabbiano, astro-ph/0305345 (2003).
14. K. Gebhardt, R. Ri, and L. Ho, Astrophys. J. Lett. **578**, L41 (2002).
15. J. Gerssen, R. Marel, K. Gebhardt, *et al.*, Astron. J. **125**, 376 (2002).
16. E. Kording, H. Falcke, and S. Marvoff, Astron. Astrophys. **382**, L13 (2002).
17. H. Wu, S. Xue, X. Xia, *et al.*, Astrophys. J. **576**, 738 (2002).
18. S. Trudolyubov, K. Borozdin, K. Mason, *et al.*, Astrophys. J. Lett. **571**, L17 (2002).
19. R. White, C. Sarazin, and S. Kulkarni, Astrophys. J. Lett. **571**, L23 (2002).
20. I. Gioia, J. Henry, C. Mullis, *et al.*, astro-ph/0309788 (2003).
21. H. Grimm, M. Gilfanov, and R. Sunyaev, Astron. Astrophys. **391**, 923 (2002).
22. A. M. Ghez, B. L. Klein, M. Morris, *et al.*, Astrophys. J. **509**, 678 (1998).
23. P. Maetini and D. Schneider, astro-ph/0309650 (2003).
24. P. Humphreys, Astrophys. J., Suppl. Ser. **29**, 389 (1975).
25. H. Lamers, N. Panagia, S. Scuderi, *et al.*, Astrophys. J. **566**, 818 (2002).
26. P. Madan and M. Rees, Astrophys. J. Lett. **551**, L27 (2001).
27. R. Schneider, A. Ferrara, R. Salvaterra, *et al.*, Nature **422**, 869 (2003).
28. J. Greiner, J. Guby, and M. McCaughrean, Nature **414**, 522 (2001).
29. A. V. Tutukov and A. M. Cherepashchuk, Astron. Zh. **80**, 419 (2003) [Astron. Rep. **47**, 386 (2003)].
30. E. Staritsyn, Nauchn. Inform. Astron. Sovet Akad. Nauk SSSR **68**, 35 (1990).
31. R. McLure and J. Dunlop, Mon. Not. R. Astron. Soc. **331**, 795 (2002).
32. M. Loewenstein, Astrophys. J. **557**, 573 (2001).
33. G. Meynet and A. Maeder, astro-ph/0006404 (2000).
34. C. Abia, I. Domingues, O. Straniero, *et al.*, Astrophys. J. **557**, 126 (2001).
35. G. Meynet and A. Maeder, Astron. Astrophys. **361**, 101 (2000).
36. J. Brodie and J. Huchra, Astrophys. J. **379**, 157 (1991).
37. K. Nagamine, M. Fukugita, R. Genand, and J. P. Ostriker, Astrophys. J. **558**, 497 (2001).
38. R. Margini, R. Corradi, R. Greiwel, *et al.*, astro-ph/0305105 (2003).
39. J. Vink, A. de Koter, and H. Lamors, astro-ph/0101509 (2001).
40. A. V. Tutukov, L. R. Yungel'son, and A. Klyaĭman, Nauchn. Inform. Astron. Sovet Akad. Nauk SSSR **27**, 1 (1973).
41. G. Meynet and A. Maeder, Astron. Astrophys. **390**, 561 (2002).
42. P. Massey and K. Olsen, astro-ph/0309272 (2003).
43. A. V. Tutukov and L. R. Yungel'son, Astron. Zh. **79**, 738 (2002) [Astron. Rep. **46**, 667 (2002)].
44. D. Pooley, W. Lewin, F. Verbunt, *et al.*, astro-ph/0305003 (2003).
45. M. Gilfanov, astro-ph/0309454 (2003).
46. R. Narayan, I. Igumenschev, and M. Abramovicz, astro-ph/0305029 (2003).
47. H. Bondi and F. Hoyle, Mon. Not. R. Astron. Soc. **104**, 273 (1944).
48. A. V. Tutukov and L. R. Yungel'son, Astrofizika **12**, 125 (1976).
49. D. V. Bisikalo, A. A. Boyarchuk, and O. A. Kuznetsov, Astron. Zh. **77**, 31 (2000) [Astron. Rep. **44**, 26 (2000)].
50. A. Boyarchuk, D. Bisikalo, E. Kilpio, and D. Kuznetsov, astro-ph/0212227 (2002).
51. A. G. Masevich and A. V. Tutukov, *Stellar Evolution: Theory and Observation* (Nauka, Moscow, 1988) [in Russian].
52. A. Piro and L. Bildstein, Astrophys. J. Lett. **571**, L103 (2002).
53. R. Hynes, C. Haswell, S. Chaty, *et al.*, Mon. Not. R. Astron. Soc. **331**, 169 (2002).
54. J. Tomsick, S. Corbel, R. Fender, *et al.*, astro-ph/0309741 (2003).
55. C. Firmani and A. Tutukov, Astron. Astrophys. **264**, 37 (1992).

56. A. V. Tutukov and A. V. Fedorova, Astron. Zh. **79**, 847 (2002) [Astron. Rep. **46**, 765 (2002)].
57. S. Ruchinski, astro-ph/0104483 (2001).
58. E. O'Sullivan, D. A. Forbes, and T. J. Ponman, Mon. Not. R. Astron. Soc. **328**, 461 (2001).
59. P. Ranalli, A. Comastri, and G. Setti, Astron. Astrophys. **399**, 39 (2003).
60. M. Ueno, A. Bamba, and K. Koyama, Astrophys. J. **588**, 338 (2003).
61. T. Roberts and E. Colbert, astro-ph/0304024 (2003).
62. A. Fabian and R. Terlevich, Mon. Not. R. Astron. Soc. **280**, L5 (1996).
63. S. Timmler, W. Lewin, in *Supernovae and Gamma-Ray Bursts*, Ed. by K. W. Weiler (Springer, New York, 2002).
64. K. Mukai, W. D. Pence, S. L. Snowden, *et al.*, astro-ph/0209166 (2002).
65. P. Kaaret, astro-ph/0206374 (2002).
66. S. Veilleux, astro-ph/0309119 (2003).
67. A. M. Cherepashchuk, Usp. Fiz. Nauk **143**, 375 (2003).
68. S. Shrader and L. Titarchuk, astro-ph/0308057 (2003).
69. J. Dunlop, R. NcLure, and M. Kukulaebol, Mon. Not. R. Astron. Soc. **340**, 1095 (2003).
70. T. Jeltema and C. Camizares, Astrophys. J. **585**, 756 (2003).
71. A. Juett and D. Chakrabarty, astro-ph/0206417 (2002).
72. A. King, astro-ph/0309524 (2003).
73. I. Iben, Jr., A. V. Tutukov, and A. V. Fedorova, Astrophys. J. **486**, 955 (1997).
74. I. Iben, Jr. and A. Tutukov, Astrophys. J., Suppl. Ser. **58**, 661 (1985).
75. W. Glatzel and H. O. Kaltschmidt, Mon. Not. R. Astron. Soc. **337**, 743 (2003).
76. R. Stothers, Astrophys. J. **568**, 312 (2002).
77. A. V. Tutukov, Astron. Zh. **80**, 692 (2003) [Astron. Rep. **47**, 637 (2003)].
78. T. Roberts, M. Goad, M. Ward, and R. Warwick, astro-ph/0303110 (2003).
79. F. Bauer and W. Brandt, astro-ph/0310039 (2003).
80. F. Rogers and C. Iglesias, Astrophys. J., Suppl. Ser. **79**, 507 (1992).
81. L. Koch-Miranmond, P. Abraham, Y. Fuchs, *et al.*, Astron. Astrophys. **396**, 877 (2002).
82. A. V. Tutukov and A. M. Cherepashchuk, Astron Zh. (2004, in press).
83. M. Weisskopf, K. Wu, A. Tennant, *et al.*, astro-ph/0311291 (2003).
84. P. Crowter, astro-ph/0305141 (2003).
85. J.-F. Liu, J. Bregman, and P. Seitzer, Astrophys. J. Lett. **580**, L31 (2002).
86. W. Dietsch, B. Mochejska, Z. Misanovic, *et al.*, astro-ph/0310111 (2003).
87. L. Zampieri, P. Mucciarelli, R. Falomo, *et al.*, astro-ph/0309687 (2003).
88. J. A. Orosz, E. Kuulkers, M. van der Klis, *et al.*, Astrophys. J. **555**, 489 (2001).
89. J. A. Irwin, J. N. Bregman, and A. E. Athey, astro-ph/0312393 (2003).

Translated by L. Yungel'son

Astronomy Reports, Vol. 48, No. 7, 2004, pp. 550–562. Translated from Astronomicheskiĭ Zhurnal, Vol. 81, No. 7, 2004, pp. 606–619.
Original Russian Text Copyright © 2004 by Abubekerov, Antokhina, Cherepashchuk.

Estimate of the Black-Hole Mass and Orbital Inclination from the Radial-Velocity Curve of the X-Ray Binary Cyg X-1

M. K. Abubekerov[1], E. A. Antokhina[2], and A. M. Cherepashchuk[1, 2]

[1] *Moscow State University, Vorob'evy gory, Moscow, 119899 Russia*
[2] *Sternberg Astronomical Institute, Moscow State University, Universitetskiĭ pr. 13, Moscow, 119899 Russia*

Received January 5, 2004; in final form, January 9, 2004

Abstract—The results of a statistical approach to interpreting a master radial-velocity curve for the X-ray binary Cyg X-1 are presented. The dependence of the mass of the X-ray component m_x on the mass of the optical component m_v is obtained in a Roche model. A method for estimating the orbital inclination from the radial-velocity curve is described. In contrast to the situation for a pointlike optical star, both the amplitude and shape of the radial-velocity curve changes as a function of the orbital inclination i in the case of a tidally deformed star with a complex temperature distribution over its surface. Thus, high-accuracy radial-velocity curves can be used to impose constraints on the mass and orbital inclination of the black hole: $i < 45^\circ$. Using the information on the optical light curve, radius, and luminosity of the optical star, we estimate $31^\circ < i < 44^\circ$ and $8.5M_\odot < m_x < 13.6M_\odot$. *© 2004 MAIK "Nauka/Interperiodica".*

1. INTRODUCTION

A new method for determining the component-mass ratio and orbital inclination of an X-ray binary from the orbital variability of the absorption-line profiles in the spectrum of the optical star was proposed by Antokhina and Cherepashchuk [1] and Shahbaz [2]. The dependence of the absorption-line profile on the phase of the orbital period is due to the tidal deformation of the star's shape and the complex temperature distribution over its surface due to gravitational darkening and the effect of X-ray heating. High-resolution spectra ($R = \lambda/\Delta\lambda = 50\,000$) are necessary to apply this method to X-ray novas in their quiescent state. In principle, such spectra can be obtained using modern 8–10 m telescopes, but with considerable difficulties.

The Cyg X-1 system, which is composed of a O9.7Iab supergiant and a black hole, is sufficiently bright ($V = 9.5^m$) to obtain high-resolution spectra suitable for investigations of fine effects in the optical star's rotation [3] and obtaining spectroscopic estimates of the parameters of the optical using model atmospheres [4].

A large number of measurements of the radial velocity of the optical star in the Cyg X-1 system with moderate spectral resolution have been accumulated up to the present. These can be used to construct a high-accuracy radial-velocity curve, which should contain the averaged effects of the orbital variability in the absorption line profiles, as is described in [1, 2]. Therefore, it is of interest to try to estimate simultaneously the black-hole mass and orbital inclination of Cyg X-1 using a high-accuracy mean radial-velocity curve.

In contrast to the model with two point masses, both the amplitude and shape of the radial-velocity curve change with variations in the orbital inclination of an X-ray binary containing a tidally deformed optical star. Wilson and Sofia [5] were the first to draw attention to this dependence. This effect makes it possible to estimate both the mass and the orbital inclination of the system based on a high-accuracy radial-velocity curve of Cyg X-1.

2. OBSERVATIONAL MATERIAL

A master radial-velocity curve was compiled from the spectral data of [6–12], which were obtained in 1973–1997. Since the test undertaken in [13] demonstrated that the theoretical radial velocities for the HeI 4713 Å and Hγ absorption lines are very similar, the velocities determined from both hydrogen and HeI lines were included in the master radial-velocity curve. Although the spectral data were separated by considerable time intervals, they agree with each other very well (Fig. 1). We took the orbital period of the X-ray binary Cyg X-1 to be $5\overset{d}{.}599829$, as follows from the analysis of a long series of observations [12].

The observed velocities were corrected for the systemic velocity before their inclusion in the radial-velocity curve. The systemic velocity of the close binary derived from the spectral data of [6–12] is

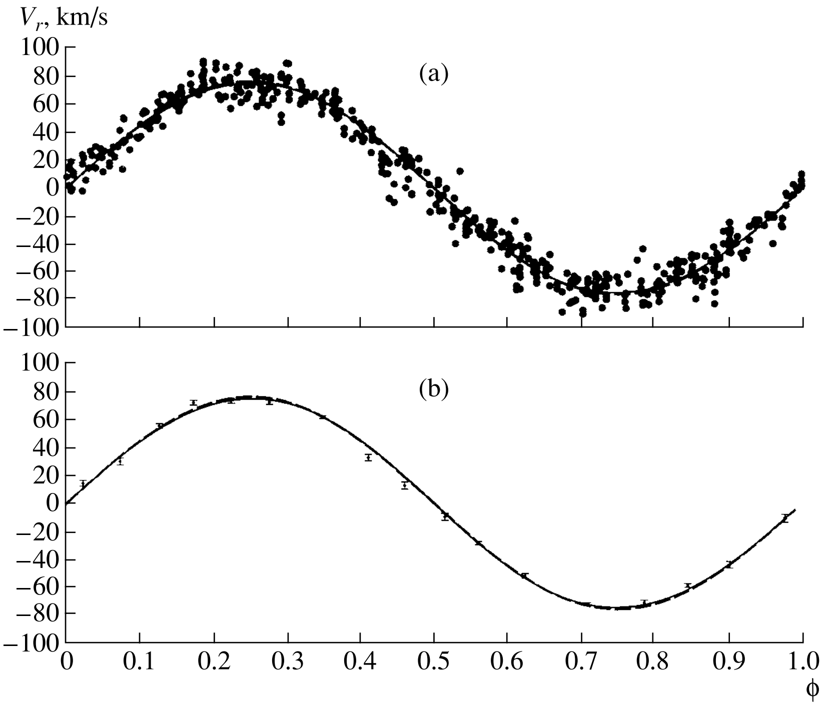

Fig. 1. (a) Master observed radial-velocity curve for the optical star in the X-ray binary Cyg X-1. Filled circles represent radial velocities derived from absorption lines of hydrogen and HeI. For comparison, theoretical radial-velocity curves for the Roche model (solid) and point-mass model (dashed) are also presented. These curves were obtained for $m_x = 10.86M_\odot$, which corresponds to the minimum residual in the Roche model with $m_v = 20M_\odot$ calculated using method 2 (i.e., excluding the mean observed radial velocities at phases 0.4–0.6) and with an orbital inclination of 35°. The parameters of the Roche model are summarized in Table 2. (b) Radial velocities averaged over phase intervals (the average radial velocities within phase intervals are presented by the filled circles). For comparison, theoretical radial-velocity curves for the Roche model (solid) and point-mass model (dashed) with $m_v = 20M_\odot$, $m_x = 10.86M_\odot$, and $i = 35°$ are also presented.

presented in Table 1. Let us discuss in more detail each of these cited works.

A set of summer observations of HDE 226868 carried out in 1973 using a 2.54-m telescope are presented in [6]. A total of 17 spectra at 6100–6800 Å with a dispersion of 20 Å/mm were obtained. The radial velocities were determined from the HeI 6678 Å absorption line.

The spectral data presented in [7] were collected from 1972 to 1975. The exposure time for these spectra was 20–65 min. A total of 85 spectra were obtained: 23 with a dispersion of 39 Å/mm obtained using a 2.1-m Cassegrain telescope and 62 with a dispersion of 63 Å/mm obtained using a 0.9-m Cassegrain telescope. The radial velocity was derived from absorption lines of hydrogen H9, H8, Hδ, Hγ, helium HeI 4026 Å, and HeI 4471 Å.

Spectra obtained from 1971 to 1981 using a 1.88-m telescope are presented in [8]. A total of 78 spectra at 3700–4920 Å with dispersions of 12 and 16 Å/mm were recorded. The radial velocity was measured using both absorption lines of hydrogen (Hβ, Hγ, Hδ, Hϵ, and H8–H16) and helium (HeI 3819.606, 4009.270, 4026.189, 4120.812, 4143.759, 4168.971, 4387.928, 4387.928, 4471.507, and 4713.143 Å).

Spectral observations obtained from 1980 to 1984 are presented in [9]. A total of 84 spectra were obtained on a 1.22-m telescope with a dispersion of 40 Å/mm (or 0.6 Å per diode), a 1.83-m telescope with a dispersion of 15 Å/mm (or 0.231 Å per diode), and a 3.6-m telescope with a dispersion of 2.4 Å/mm (or 0.036 Å per diode). The radial velocities were measured separately using absorption lines of hydrogen and helium. The radial velocity for the hydrogen absorption lines was determined as the weighted mean of the velocities for the Hβ, Hγ, and Hδ lines. The radial velocity for the helium lines was determined as the weighted mean of the velocities for the HeI 4009.270, 4026.189, 4120.812, 4143.759, 4387.928, 4471.477, 4713.143, 4921.929, 5015.675, and 5047.736 Å absorption lines.

Observations of HDE 226868 carried out in 1985–1986 are described in [10]. A total of 14 spectra

Table 1. Observation epoch, element whose line was used to measure the radial velocity, number of spectra, and systemic radial velocity of the optical component of Cyg X-1

JD 24400000+	Element	Number of spectra	γ velocity, km/s	Reference
41844–41290	HeI	17	−3.6	[6]
42205–42910	H, HeI	85	−5.3	[7]
41213–44795	H	78	−2.5	[8]
	HeI	78	−4.2	[8]
44513–45895	H	56	−10.4	[9]
	HeI	84	−5.6	[9]
46332–46635	HeI	14	−10.5	[10]
50228–50255	H	35	−7.5	[11]
	HeI	35	−2.9	[11]
50615–50677	HeI	20	−2.1	[12]

were obtained on a 2.1-m telescope at 6500-6710 Å with a dispersion of 0.14 Å per pixel. The exposure time for each spectrum varied from 1–3 h. The signal-to-noise ratio per pixel was $S/N = 100-300$. The radial velocity was measured using the HeI 6678 Å absorption line.

Observations of the optical component of Cyg X-1 carried out in 1996 using the Isaac Newton Telescope are presented in [11]. A total of 37 spectra were obtained at 4100–4900 Å with a dispersion of 0.8 Å/mm, exposure times of 100–200 s, and $S/N > 100$. The radial velocity was determined relative to a standard spectrum of Cep 19 using a cross-correlation method. The velocity was measured separately for the absorption lines of hydrogen and HeI. The HeI 4387.928, 4471.477, 4713.143, and 4921.929 Å absorption lines were used.

Spectra obtained using a Coudé spectrograph of the 2.6-m telescope of the Crimean Astrophysical Observatory are presented in [12]. A total of 20 spectra with a dispersion of 3 Å/mm and a resolution of 25 000 were recorded. The mean exposure time was 1.5 h, yielding final signal-to-noise ratios $S/N = 100$. The width of the spectra was 60 Å. Before determining the radial velocity, the spectra were centered on the HeII 4686 Å line. The radial velocity was measured using the HeI 4713.143 Å line.

Thus, we collected 502 radial-velocity measurements distributed fairly uniformly in orbital phase (Fig. 1). To reduce the influence of random errors, the radial velocities were averaged in phase intervals with widths of 0.05 to 0.08. The mean radial-velocity curves are presented in Fig. 1b. Quantrell *et al.* [14] have shown that the errors in the observed radial velocity of the optical star due to tidal gravitational waves are random and, thus, can be suppressed by averaging over many observations.

Due to the large number of measured radial velocities (502 values) and the comparatively large half-amplitude of the radial-velocity curve for the Cyg X-1 system (∼75 km/s), the relative errors of the normal points in the mean observed radial-velocity curve are small (∼3%). This provides hope of being able to simultaneously estimate the black-hole mass and orbital inclination based on this radial-velocity curve.

3. INTERPRETATION OF THE AVERAGE RADIAL-VELOCITY CURVE

The optical component in the close binary Cyg X-1 approximately fills its critical Roche lobe [15]. Due to the tidal action with the relativistic companion, the shape of the optical component is not spherical. The side facing the relativistic component is heated by X-ray radiation. These effects must be taken into consideration when interpreting the observed radial-velocity curve. We accordingly fit the curve in a Roche model, which enabled us to implement a first approximation to include these effects. A detailed description of the Roche model is presented in [16], and we do not repeat this information here. The numerical values of the parameters for the X-ray binary Cyg X-1 are summarized in Table 2.

The orbit was taken to be circular, since the orbital period ($P_{orb} \simeq 5\overset{d}{.}6$) is comparable to the periods of the X-ray binaries SMC X-1 ($P_{orb} \simeq 3\overset{d}{.}9$) and 4U 1538-52 ($P_{orb} \simeq 3\overset{d}{.}7$), whose orbits are circular, according to the results of timing measurements for X-ray pulsars [18, 19]. The coefficient of asynchronism of the rotation f was taken to be 0.95, in accordance with the results of Gies and Bolton [3], whose analysis of the profile of the HeI 4471 Å line led them to conclude that the coefficient of asynchronism was close to unity. This also supports our assumption that the orbit is circular [20, 21]. Since the radius of the optical star is more than 0.25 of the radius of the relative orbit of the system, we can assume that the orbit of the Cyg X-1 system has had time to circularize since the formation of the black hole [20, 21]. It is not possible to accurately determine the eccentricity e from the radial-velocity curve of the optical star due to the effect of the anisotropy of the stellar wind (for more details, see [13, 22]).

The masses of both components and the orbital inclination were treated as unknown parameters. We

Table 2. Parameters used to synthesize the radial-velocity curves of the optical component of Cyg X-1 in the Roche model

P, days	5.599829	Period
e	0.0	Eccentricity (postulated)
i, deg	30, 35, 40 45, 55, 65	Orbital inclination
μ	0.95*	Roche-lobe filling by the optical component
f	0.95	Asynchronism of rotation of the optical component
T_{eff}(K)	32 000**	Effective temperature of the optical component
β	0.25	Gravitational darkening
k_x	0.02	X-ray luminosity of the relativistic component/ bolometric luminosity of the optical component, L_x/L_v
A	0.5	Reprocessing of the X-ray radiation
u	0.3***	Limb darkening

* Data taken from [15].

** Data taken from [4].

*** Data taken from [17].

obtained multiple solutions of the direct problem using various parameter values. A series of masses of the compact object m_x were considered for each mass of the optical component m_v from the discrete set of values 20, 30, 40, 50, 60, and $70M_\odot$ for a specified orbital inclination i. This yielded the dependences of the mass of the compact object on the mass of the optical component for $i = 30°$, $35°$, $40°$, $45°$, $55°$, and $65°$.

The residual between the mean observed radial-velocity curve and the theoretical curve was calculated using the formula

$$\Delta m_x = \frac{\sum_{j=1}^{M}(n_j - 1)}{M} \frac{\sum_{j=1}^{M} n_j (V_j^{teor} - \bar{V}_j^{obs})^2}{\sum_{j=1}^{M} n_j (n_j - 1)\sigma_j^2}, \quad (1)$$

where $\bar{V}_j^{obs}$ is the observed mean radial velocity in a phase interval centered at $\bar{\phi}_j$, V_j^{teor} is the theoretical radial velocity at this phase, σ_j is the rms deviation for $\bar{V}_j^{obs}$ in the given phase interval centered at $\bar{\phi}_j$, M is the number of phase intervals, and n_j is the number of averaged observations of the radial velocity in a given phase interval.

The quantity $\Delta(m_x)$ is distributed according to a Fisher law, $F_{M,\sum_{j=1}^{M}(n_j-1),\alpha}$ [23]. If the significance level α is specified, we can find a confidence set for the unknown parameter m_x for fixed values of i and m_v. This set is composed of values of m_x for which the following condition is satisfied [24]:

$$\Delta m_x \le F_{M,\sum\limits_{j=1}^{M}(n_j-1),\alpha}.$$

In addition to the Roche model, we also found solutions using a point-mass model. The results were used to reveal discrepancies between the models.

Let us discuss the stellar wind from the optical component in the Cyg X-1 binary in more detail. The optical star is an O supergiant. The nonuniformity of the gravitational force at its surface and heating of the surface facing the relativistic companion disrupt the isotropy of the stellar-wind outflow. The wind velocity increases near the Lagrange point L_1. This is manifest as an excess negative radial velocity near phase 0.5, when the X-ray source is in front of the O supergiant (Fig. 1). A detailed analysis of the anisotropy of the stellar wind in an X-ray binary with OB supergiants was carried out in [13]. This anisotropy leads to systematic errors in the observed radial-velocity curve. We accordingly used the following two methods to fit the mean radial-velocity curve.

Method 1. Using all the averaged observed radial velocities.

Method 2. Excluding the observed radial velocities at phases 0.4–0.6, since they are most distorted by the anisotropy of the stellar wind.

We adopted a significance level of 5%. Both the Roche and point-mass models can be rejected at a

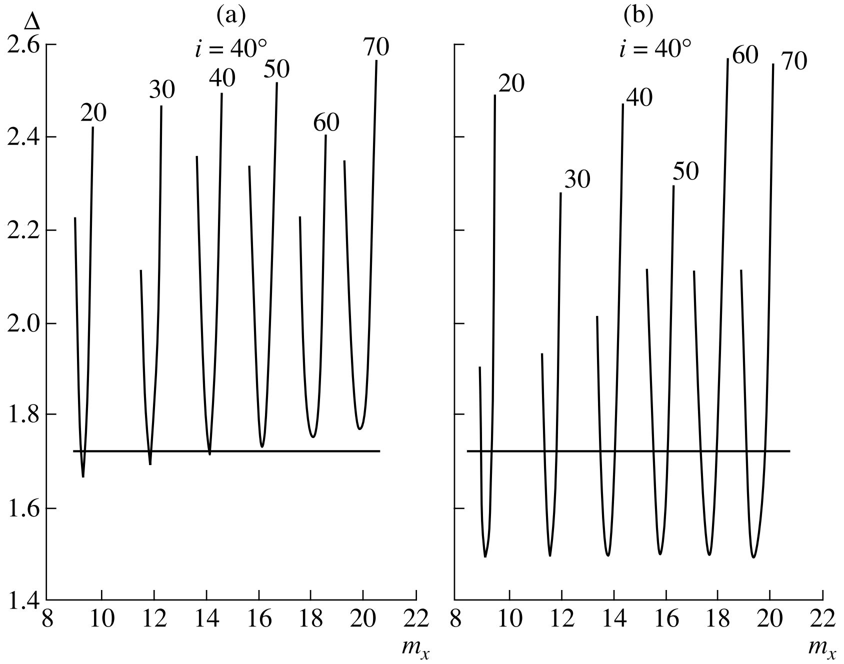

Fig. 2. Residuals obtained for method 2 (i.e., excluding the mean observed radial velocities at phases 0.4–0.6). Shown are the difference between the mean observed radial-velocity curve of Cyg X-1 and the synthesized curves for the (a) Roche model and (b) point-mass model for orbital inclination 40°. The horizontal line corresponds to the critical residual according to the Fisher criterion, $\Delta_{13,401} = 1.72$ for a significance level of 5%. The masses of the optical component in solar masses for which the residuals were derived are presented near the curves.

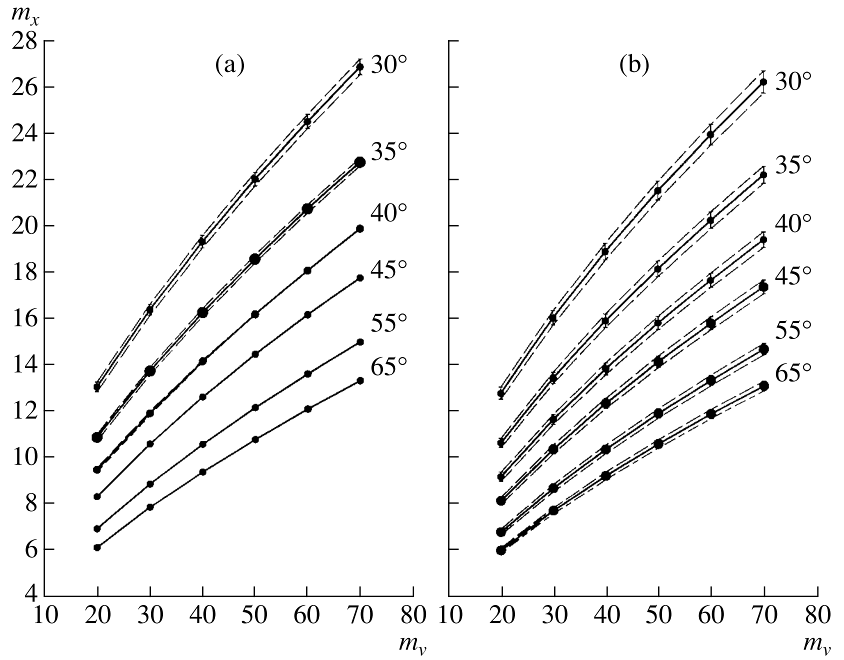

Fig. 3. (a) Dependence of the mass of the compact object in the Cyg X-1 binary on the mass of the optical star obtained in the Roche model using method 2 (i.e., excluding the mean observed radial velocities at phases 0.4–0.6). The orbital inclinations are shown near the curves. (b) Same dependence for the point-mass model. In this case, a model can be obtained for any orbital inclination i and the corresponding confidence interval (whose boundaries are marked by the dashed curves) estimated. Because the Roche model can be rejected for $i \geq 45°$, confidence intervals were not determined for $i \geq 45°$ and the error band is not indicated.

Table 3. Dependence of mass of the relativistic component on mass of the optical component in the Roche model for $i = 30°–65°$

$m_v, M_\odot$	$m_x, M_\odot$					
	$i = 30°$	$i = 35°$	$i = 40°$	$i = 45°$	$i = 55°$	$i = 65°$
20	$13.03^{+0.21}_{-0.21}$	$10.86^{+0.21}_{-0.21}$	$9.37^{+0.09}_{-0.09}$	8.31	6.92	6.12
30	$16.36^{+0.24}_{-0.24}$	$13.71^{+0.21}_{-0.21}$	$11.89^{+0.09}_{-0.09}$	10.58	8.85	7.84
40	$19.29^{+0.27}_{-0.26}$	$16.24^{+0.21}_{-0.21}$	$14.13^{+0.05}_{-0.05}$	12.59	10.56	9.36
50	$21.98^{+0.29}_{-0.30}$	$18.55^{+0.21}_{-0.21}$	16.16	14.43	12.12	10.76
60	$24.47^{+0.31}_{-0.30}$	$20.70^{+0.21}_{-0.21}$	18.06	16.14	13.58	12.06
70	$26.83^{+0.33}_{-0.33}$	$22.72^{+0.21}_{-0.21}$	19.85	17.74	14.95	13.29

Table 4. Dependence of mass of the relativistic component on mass of the optical component in the point-mass model for $i = 30°–65°$

$m_v, M_\odot$	$m_x, M_\odot$					
	$i = 30°$	$i = 35°$	$i = 40°$	$i = 45°$	$i = 55°$	$i = 65°$
20	$12.82^{+0.26}_{-0.26}$	$10.68^{+0.21}_{-0.19}$	$9.23^{+0.20}_{-0.19}$	$8.19^{+0.16}_{-0.15}$	$6.84^{+0.12}_{-0.12}$	$6.06^{+0.11}_{-0.10}$
30	$16.07^{+0.32}_{-0.31}$	$13.48^{+0.25}_{-0.24}$	$11.69^{+0.22}_{-0.20}$	$10.41^{+0.20}_{-0.18}$	$8.74^{+0.16}_{-0.16}$	$7.76^{+0.14}_{-0.13}$
40	$18.94^{+0.36}_{-0.36}$	$15.95^{+0.29}_{-0.29}$	$13.87^{+0.25}_{-0.25}$	$12.38^{+0.22}_{-0.22}$	$10.41^{+0.19}_{-0.17}$	$9.27^{+0.17}_{-0.16}$
50	$21.56^{+0.40}_{-0.41}$	$18.20^{+0.33}_{-0.33}$	$15.86^{+0.29}_{-0.27}$	$14.17^{+0.25}_{-0.26}$	$11.95^{+0.21}_{-0.20}$	$10.65^{+0.19}_{-0.18}$
60	$23.98^{+0.45}_{-0.44}$	$20.29^{+0.38}_{-0.36}$	$17.71^{+0.32}_{-0.31}$	$15.84^{+0.28}_{-0.27}$	$13.38^{+0.23}_{-0.23}$	$11.93^{+0.20}_{-0.19}$
70	$26.27^{+0.48}_{-0.48}$	$22.25^{+0.40}_{-0.36}$	$19.46^{+0.34}_{-0.34}$	$17.42^{+0.30}_{-0.30}$	$14.72^{+0.25}_{-0.25}$	$13.14^{+0.22}_{-0.21}$

significance level of $\alpha = 5\%$ for method 1. We accordingly identified method 2 as being preferable.

Analysis of the mean observed radial-velocity curves indirectly taking into account the wind anisotropy using method 2 yielded models that were acceptable at the 5% significance level. Consequently, it is important to bear in mind the anisotropy of the stellar wind when interpreting the radial velocity curves for OB stars in close binary systems [13, 22]. The behaviors of the residuals obtained using the Roche and point-mass models for an orbital inclination of 40° are presented in Fig. 2. The results were used to construct the dependences of the mass of the X-ray component on the mass of the optical star (Figs. 3a and 3b). When the orbital inclination is 40° and the optical component mass is specified to be $50M_\odot$, the minimum residual occurs for $m_x = 16.16M_\odot$ and is equal to the quantile of the critical level. Therefore, the error band in Fig. 3a is truncated at an optical-star mass of $50M_\odot$. At orbital inclinations of 45° or more, no mass of the relativistic component can fit the mean observed radial-velocity curve at the 5% significance level, as will be discussed in more detail below. Therefore, the component-mass dependences for inclinations of 45°, 55°, and 65° derived by minimizing the residuals are presented in Fig. 3a without error bands. The numerical results of fitting the mean radial-velocity curve using method 2 in the Roche model are presented in Table 3, and the results for the point-mass model are presented in Table 4. The masses of the compact object for which the models were rejected at the 5% significance level are presented in Table 3 without the confidence intervals.

Tables 3 and 4 show that the masses of the compact object obtained in the Roche model are systematically slightly greater than those obtained in the point-mass model (by $\sim 2\%$).

The similarity of the masses of the compact object obtained for these two models can be explained by the following two reasons. First, the temperature of the "nose" of the optical star is lower than the temperature of most of its surface due to the low gravitational acceleration near L_1 (gravitational darkening). Second, the heating of the part of the optical star facing the X-ray source is low ($k_x = 0.02$). Therefore, the nose, which produces the largest perturbation to the observed radial-velocity curve, contributes only a

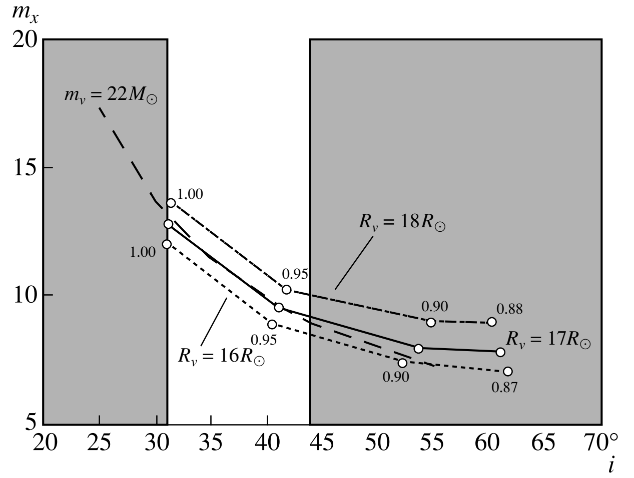

Fig. 4. Dependence of the mass of the compact object in Cyg X-1 on the orbital inclination. The solid, dash–dot, and dotted curves were derived from the fit to the light curve [25] with radii of the optical star equal to $17R_\odot$ [4], $18R_\odot$, and $16R_\odot$ [4]; the dashed curve was derived from the observed mean radial-velocity curve with the mass of the optical star equal to $22M_\odot$. The numbers near the hollow circles show the degree of filling of the Roche lobe by the optical star. Dark regions correspond to orbital inclinations that are incompatible with the light curve presented in [25] and the radial-velocity curve.

small fraction of the integrated emission of the optical component. This can explain the similarity of the results for the Roche and point-mass models. The influence of the heating coefficient on the shape of the radial-velocity curve is discussed in more detail in [1].

4. MASSES OF THE COMPONENTS OF Cyg X-1

Constraint on the Mass of the Black Hole from the Radial-Velocity Curve

As follows from Fig. 3a and Table 3, the high-accuracy mean observed radial-velocity curve enables us to impose an upper limit on the orbital inclination of the Cyg X-1 binary independent of the mass of the optical star m_v: $i < 45°$. This upper limit can be used to obtain a lower limit for the black-hole mass. The mass of the compact object m_x following from the mass function of the optical star $f_v(m)$ is

$$m_x = f_v(m)\left(1+\frac{1}{q}\right)^2\frac{1}{\sin^3 i}. \qquad (2)$$

Since $q = m_x/m_v > 0$, expression (2) gives

$$m_x > f_v(m)\frac{1}{\sin^3 i}, \qquad (3)$$

where $f_v(m)$ can be determined from the expression

$$f_v(m) = \frac{P(1-e^2)^{3/2}}{2\pi G}K_v^3. \qquad (4)$$

Note that the observed mass function $f_v(m)$ corresponds to the real (nonpointlike) shape of the star and, thus, is low when compared with a point-mass model. We can take this into account when using mass function (4) by substituting the quantity K_v corresponding to the value of m_x obtained in the Roche model rather than the point-mass model. We corrected the observed value of $f_v(m)$ for the uncertainty in the parameters of the optical star. For example, if the orbital inclination is $i = 35°$, $f_v(m) = 0.245 \pm 0.002M_\odot$ in the point-mass model, while the corrected mass function is $f_v(m) = 0.2571 \pm 0.0006M_\odot$. When $i = 40°$, $f_v(m) = 0.248 \pm 0.002M_\odot$ in the point-mass model, while the corrected value is $f_v(m) = 0.2580 \pm 0.0007M_\odot$. We will take the mass function of the optical component to be $0.258M_\odot$. Using this new mass function and the upper limit for the orbital inclination, $i = 45°$, we can derive a lower limit on the mass of the black hole from (3). As a result, we find that the mass of the black hole in the Cyg X-1 binary is $m_x > 0.73M_\odot$. We emphasize again that this estimate was derived purely from a single high-accuracy radial-velocity curve.

Estimating the Black-Hole Mass from the Radius of the Optical Component

Fits of a high-accuracy light curve of Cyg X-1 for distances to the system of 1.5, 2.0, and 2.5 kpc, which correspond to radii of the optical component of 13.5, 18.0, and $22.5R_\odot$, are presented in [25]. The relation between the component-mass ratio q and the orbital inclination i was determined for the corresponding degree of filling of the Roche lobe by the optical star. Analysis of the light curve presented in [25] shows that, if $i < 31°$, the optical star must overfill its Roche lobe if it is to produce the observed amplitude of the optical light curve ($\sim 0.04^m$). Overfilling of the Roche lobe in Cyg X-1 is unrealistic from a physical point of view, since Cyg X-1 is not associated with an object such as SS 433. If the optical star in a massive X-ray system overfills its Roche lobe, the rate of inflow of material to the accretion disk is so high that the disk becomes optically thick to X rays, and a bright optical accretion disk is observed instead of an X-ray source. Since a powerful X-ray source is observed in Cyg X-1, we can reject the hypothesis that the optical star overfills its Roche lobe. Therefore, the analysis of the light curve provides a lower limit on the orbital inclination of the Cyg X-1 binary: $i > 31°$.

The analysis of spectra of the optical component in a non-LTE approximation conducted in [4] yields a radius for the optical star of $17R_\odot$. Based on this radius and the fits to the light curve from [25], we constructed the dependence of the mass of the relativistic component in Cyg X-1 on the orbital inclination (Fig. 4). The mass of the compact object for q and i values corresponding to $17R_\odot$ was calculated using (2). Figure 4 shows that, given the limits on the orbital inclination, $i = 31°-44°$, the mass of the compact object obtained in [25] should be $9.2-12.8M_\odot$. We verified the dependence of the estimate of m_x on the radius of the optical star by considering two additional radii, 16 and $18R_\odot$. These R_v values were also used to construct the dependences of the black-hole mass m_x on the orbital inclination i (Fig. 4) by fitting the light curve [25]. We can see in Fig. 4 that the corresponding dependences are fairly close to each other: for the range of allowed orbital inclinations $31° < i < 44°$, the range of black-hole masses is $8.5-12.0M_\odot$ and $10.0-13.6M_\odot$, respectively, for $R_v = 16R_\odot$ and $18R_\odot$.

Therefore, taking the optical-star radius to be $R_v = 17 \pm 1R_\odot$, we find that the mass of the black hole in the Cyg X-1 binary is in the range $m_x = 8.5-13.6M_\odot$.

Estimate of the Black-Hole Mass Based on Luminosity of the Optical Component

The detailed spectroscopic analysis of [4] yielded both the radius R_v and the bolometric luminosity $\log(L_v/L_\odot) = 5.4$ of the optical star in the Cyg X-1 system. This luminosity could then be used to obtain an estimate of the optical star's mass.

The mass–luminosity relation for the optical components of X-ray binaries differs from the relation for isolated stars [26]. An optical star in a close binary with a filled Roche lobe or an intense stellar wind loses the upper layers of its atmosphere. As a result, its surface temperature and luminosity are greater than for an isolated star of the same mass. Let us consider the mass–luminosity relation for OB supergiants in X-ray binaries (which contain X-ray pulsars for which eclipses are observed) presented in Fig. 7 of [27]. The luminosity of the optical component in Cyg X-1, $\log(L_v/L_\odot) = 5.4$, corresponds to the mass $22M_\odot$, whereas the mass–luminosity relation for noninteracting binaries gives the mass $28M_\odot$ for the same luminosity. We will take the mass of the optical component to be $22M_\odot$. We used the relationship between the masses of the optical star and the compact object obtained in the Roche model (Fig. 3a) to derive the dependence of the mass of the compact object on the orbital inclination when $m_v = 22M_\odot$ (Fig. 4). With the allowed range of orbital inclinations, $i = 31°-44°$, the mass of the compact object should be in the range $m_x = 9.0-13.2M_\odot$.

Therefore, the black-hole masses derived from the radius of the optical component and a fit of the light curve, on the one hand, and from the luminosity of the optical star, on the other hand, agree very well. Thus, we estimate the mass of the compact object to be $m_x = 8.5-13.6M_\odot$ for the allowed range of orbital inclinations $i = 31°-44°$.

5. DETERMINING THE ORBITAL INCLINATION FROM THE RADIAL-VELOCITY CURVE

Let us consider the relations between the masses of the components derived in the Roche model for $i =$ 30°, 35°, 40°, 45°, 55°, and 65° (Fig. 3a). We can see that, beginning from $i = 45°$, the theoretical radial-velocity curves cannot fit the high-accuracy mean observed radial-velocity curve at the 5% significance level for any mass of the optical star.

Figure 5a presents plots of the residuals calculated when determining the mass of the relativistic component in the Roche model for $i = 30°$, 35°, 40°, 45°, 55°, and 65° and the mass of the optical component $m_v = 22M_\odot$. The minimum residual between the observed mean and theoretical radial-velocity curves in the Roche model increases with the orbital inclination. In other words, the model is sensitive to both the mass of the compact object and the orbital inclination. Additional calculations show that it is not possible to obtain a description of the observed mean radial-velocity curve at the 5% significance level for inclinations above $i = 44°$ and $m_v = 22M_\odot$ for any mass of the compact object.

Figure 5b shows plots of the residuals calculated when determining the mass of the relativistic object in the point-mass model for $i = 30°$, 35°, 40°, 45°, 55°, and 65° and the mass of the optical component $m_v = 22M_\odot$. The minimum residual is constant in this case; i.e., the model is sensitive only to $m_x \sin^3 i$. In other words, some mass of the compact object that satisfies the mean observed radial-velocity curve at the 95% confidence level can be determined for any orbital inclination; the minimum residual is always the same.

The possibility of determining the orbital inclination from the high-accuracy mean observed radial-velocity curve arises due to the method used to calculate the radial velocity in the Roche model. The radial velocity of a star is calculated from the shift of the integrated Hγ line profile relative to its laboratory wavelength. The position of the core of the Hγ absorption line at each phase of the orbital period is determined as the average wavelength at one-third, two-thirds, and one-half of the residual intensity of the absorption line (for more details, see [1, 16]).

If the optical star were pointlike, the profile of the absorption line would not change shape with the phase of the orbital period and the Doppler shift of the

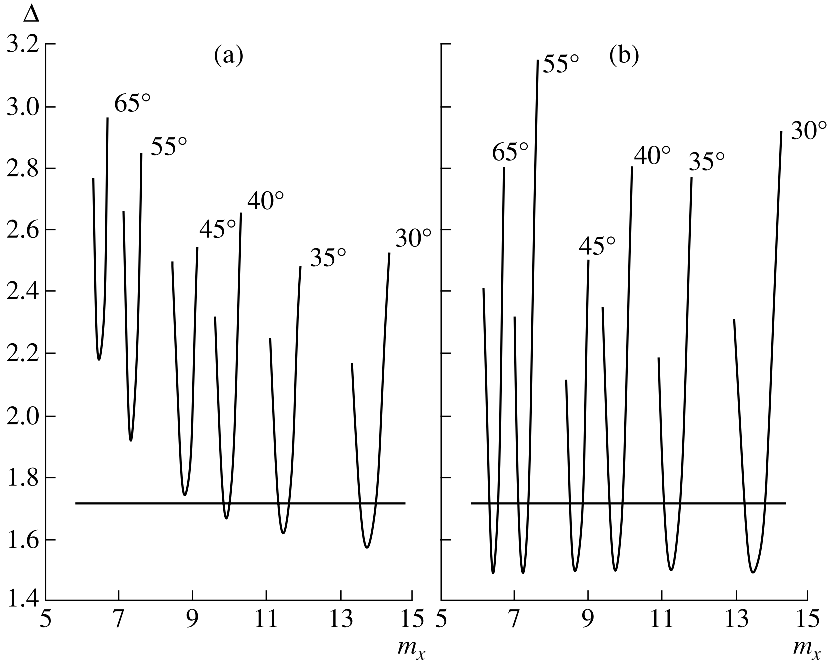

Fig. 5. (a) Residual obtained by fitting the mean observed radial-velocity curve in the Roche model using method 2 (i.e., excluding the mean observed radial velocities at phases 0.4–0.6) with $m_v = 22M_\odot$ and various orbital inclinations (the other parameters of the Roche model are listed in Table 2). The orbital inclinations are written near the curves. (b) Same for the point-mass model.

absorption-line core would correspond to the velocity of the center of mass of the star. On the other hand, since the optical component is actually a pear-shaped object with a complex temperature distribution over its surface, the absorption-line profile at each phase differs from that formed by a point mass. The shift of the core of the Hγ absorption line relative to the laboratory value 4340.47 Å will no longer correspond to the velocity of the center of mass. As a result, there

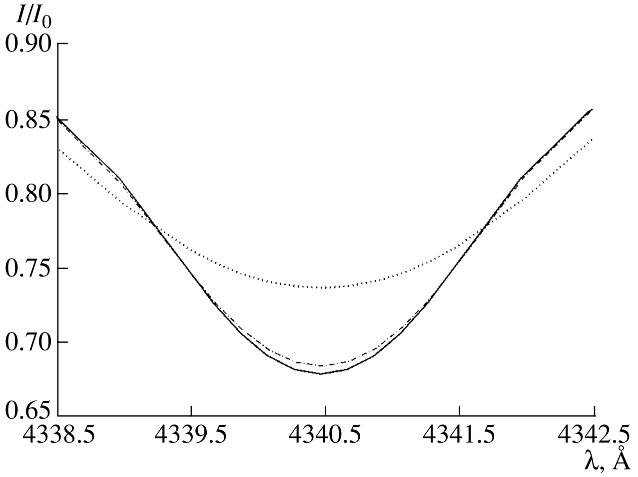

Fig. 6. Profile of the Hγ absorption line in the spectrum of the optical star in Cyg X-1 for $m_v = 22M_\odot$, $m_x = 11.47M_\odot$ and $i = 35°$ at phase 0.0 (solid) and phase 0.25 (dash–dot) and for $m_v = 22M_\odot$, $m_x = 6.48M_\odot$, and $i = 65°$ at phase 0.25.

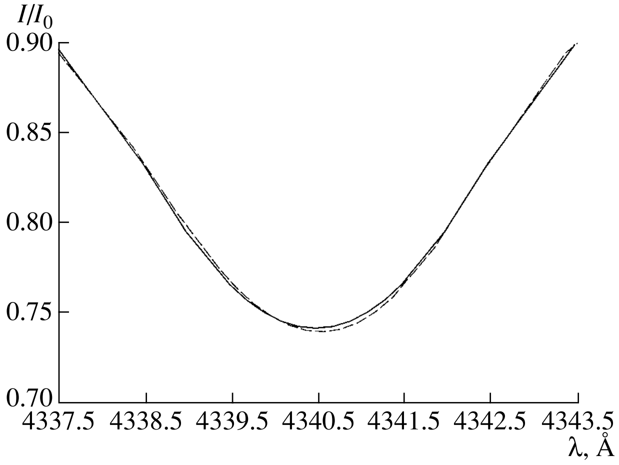

Fig. 7. Profile of the Hγ absorption line in the spectrum of the optical star in Cyg X-1 for $m_v = 22M_\odot$, $m_x = 11.47M_\odot$, $i = 80°$, and $\mu = 1$ at phase 0.0 (solid) and phase 0.40 (dashed); the other parameters of the Roche model are presented in Table 2. The line profile at phase 0.40 was corrected for the Doppler shift, which was determined as the mean of the shifts at residual-intensity levels of one-third, two-thirds, and one-half.

will be a discrepancy between the theoretical radial velocities in the Roche and point-mass models for a given orbital inclination.

For example, the core of the Hγ absorption line in the point-mass model is shifted from the laboratory value by 1.101 Å at phase 0.25, whereas the core is shifted by 1.084 Å in the Roche model due to the asymmetry of the profile. Figure 6 presents the Hγ profiles in the Roche model at phase 0.0 (when the optical component is in front of the compact object) and at phase 0.25 for $m_v = 22M_\odot$ and $i = 35°$. The Hγ absorption profile is symmetric at phase 0.0 due to the symmetric distribution of the temperatures of the emissive regions of the optical component. At phase 0.25, the profile is asymmetric relative to the Hγ profile at phase 0.0 (Fig. 6). To demonstrate the effect of this asymmetry more clearly, we carried out additional line-profile calculations for phases 0.0 and 0.40 for an orbital inclination of $i = 80°$, with the optical component filling its Roche lobe ($\mu = 1.0$) and the remaining model parameters equal to those for Cyg X-1 (Table 2). The synthesized profiles are presented in Fig. 7. We can see that the shape of the Hγ profile varies with the phase of the orbital period.

Note that the theoretical profiles do not suffer from the effect of smoothing by the instrumental profile of a spectrograph, while the observed profiles used to derive the radial-velocity curve were smoothed by the corresponding instrumental profile. Since the radial velocity was measured using fairly broad hydrogen Balmer lines and HeI lines, and the resolution of the observations was high, we can disregard the effect of smoothing of the theoretical profiles by an instrumental profile.

In addition, we synthesized radial-velocity curves from the Hγ absorption profile convolved with the instrumental profile. These calculations were carried out for two instrumental profiles with full widths at half maximum FWHM = 7 Å and FWHM = 14 Å. In a special calculation, the mass of the optical component was taken to be $m_v = 22\ M_\odot$, keeping the other model parameters the same (Table 2). We considered a series of masses for the compact object m_x and orbital inclinations $i = 30°, 35°, 40°, 45°, 55°$, and 65°. These calculations show that, as before, all models with orbital inclinations exceeding 45° can be rejected at the 5% significance level. The residuals between the observed radial-velocity curve obtained from the undistorted synthesized Hγ profile and the profile convolved with the instrumental function were very similar at various values of i. Therefore, the observed radial-velocity curves of binaries with OB stars (derived from HeI lines and Balmer hydrogen lines, which are substantially broadened by the Stark effect) can be interpreted using a synthesized Hγ absorption profile, neglecting the influence of the instrumental function of the spectrograph.

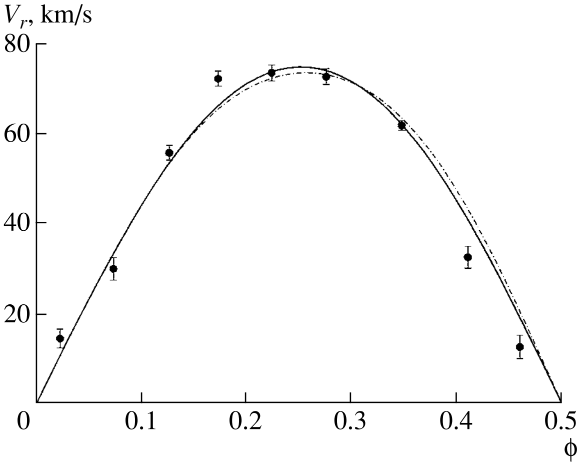

Fig. 8. Theoretical radial-velocity curve of the optical star in the Cyg X-1 binary calculated for the parameters corresponding to the minimum residual: $m_v = 22M_\odot$, $m_x = 11.47M_\odot$, and $i = 35°$ (solid curve) and $m_v = 22M_\odot$, $m_x = 6.48M_\odot$, and $i = 65°$ (dash–dot curve). The mean observed radial velocities of the optical star are shown by the points. Although the amplitudes of the best-fit radial-velocity curves are similar, the shapes of the two curves are substantially different. Precisely this fact enables us to impose constraints on the orbital inclination i using the high-accuracy radial-velocity curve.

In the case of a point source, if the orbital inclination is changed, the speed of the motion at a given phase will change by the ratio of the sines of the former and new orbital inclination angle (see, for example, [28]). In the Roche model, the pattern will change qualitatively when the inclination of the binary changes. Formerly hidden regions of the optical component will appear in the observer's plane of the sky, while some previously visible regions disappear. The observed line profile at a given phase will be fundamentally different (Fig. 6).

For example, when $i = 35°$ and $m_v = 22M_\odot$, the minimum residual in the Roche model corresponds to the mass of the compact object $m_x = 11.47M_\odot$. When $i = 65°$ and $m_v = 22M_\odot$, the minimum residual in the Roche model corresponds to $m_x = 6.48M_\odot$. The theoretical radial-velocity curves for these cases are presented in Fig. 8. We can see a qualitative difference between the radial-velocity curves due to the variation in the orbital inclination. When $m_x = 6.48M_\odot$, $m_v = 22M_\odot$, and $i = 65°$, the deviations of the radial velocities, determined by the shift of the integrated Hγ profile relative to the observed mean velocity, are too large to be acceptable at the 95% confidence level.

Therefore, the high-accuracy radial-velocity curve and the Roche model can be used to find an upper limit for the orbital inclination. The upper limit to the orbital inclination of the Cyg X-1 binary is $i = 44°$ for $m_v = 22M_{\odot}$. A light curve with a smaller observational error ($\sigma \simeq 1$ km/s) would enable more precise estimation of the orbital inclination.

6. DEPENDENCE OF THE SHAPE OF THE RADIAL-VELOCITY CURVE ON THE ORBITAL INCLINATION

To study more carefully the effect of the orbital inclination on the shape of the radial-velocity curve in the Roche model, we calculated a series of theoretical radial-velocity curves for various orbital inclinations for both circular and elliptical orbits.

When synthesizing the radial-velocity curves for a circular orbit, the mass of the optical star was taken to be $m_v = 22M_{\odot}$, and the mass of the relativistic component, to be $m_x = 11.47M_{\odot}$. This mass of the compact object corresponds to the fit of the mean observed radial-velocity curve for orbital inclination 35° (Table 3, Fig. 2a). The values of other parameters of the Roche model were the same as before (Table 2). Theoretical radial-velocity curves were synthesized for orbital inclinations $i = 30°$, 60°, and 90°. Since the amplitude of the radial-velocity curves increases with the orbital inclination, the theoretical radial velocity was normalized to the maximum velocity in the phase interval 0.0–0.5. These normalized radial velocities for $i = 30°$, 60°, and 90° are presented in Fig. 9a. Due to the small magnitude of the effect, this figure presents only fragments of the relative radial-velocity curves. The shape of the curve is sensitive to the orbital inclination: the relative radial velocity of the optical star increases at phases 0.3–0.5 (and the reciprocal phase interval 0.5–0.8) with increasing i.

Theoretical radial-velocity curves for an orbit with eccentricity $e = 0.05$ were calculated for $m_v = 22M_{\odot}$ and $m_x = 11.47M_{\odot}$, which corresponds $m_v = 22M_{\odot}$ in the relation between the component masses for $i = 35°$ (Fig. 2a). Radial-velocity curves for $i = 30°$, 60°, and 90° were synthesized for the longitudes of periastron $\omega_v = 0°$, 90°, 180°, and 270°. The theoretical values of the radial velocity were normalized to the maximum velocity at phases 0.0–0.5. The theoretical relative radial-velocity curves for the optical star for each longitude of periastron $\omega_v = 0°$, 90°, 180°, and 270° show variations in the shape of the radial-velocity curves, with the velocity at phases 0.3–0.5 (and the reciprocal phases 0.5–0.8) increasing with the orbital inclination. Due to the similarity of the various figures, we present here only the set of relative radial-velocity curves for $\omega_v = 90°$ (Fig. 9b). Since the effect has a small magnitude, only fragments of the curves are presented in Fig. 9b.

To complete our study of the mean observed radial-velocity curve, we estimated the eccentricity e. This search was carried out both using all the observed mean radial velocities and excluding the values at phases 0.4–0.6.

In the search for the eccentricity using all the observed mean radial velocities, we specified the mass of the optical component to be $m_v = 22M_{\odot}$. The initial value of the eccentricity was taken to be $e = 0.05$. The solution was found by obtaining multiple solutions of the direct problem, with the mass of the compact object being a variable parameter and the other parameters of the Roche model being the same as before (Table 2). The minimum residual, calculated using (1), was reached for the mass of the compact object $m_x = 13.5M_{\odot}$ and the longitude of periastron of the optical star $\omega_v = 270°–330°$, but this model was rejected at the 5% significance level. The mass of the compact companion for which the minimum residual was reached depended very weakly on the eccentricity and longitude of periastron of the optical component. If the eccentricity is reduced to 0.02–0.04, models with $\omega_v = 280°–330°$ and $m_x = 13.5M_{\odot}$ can be accepted at the 95% confidence level. For other longitudes of periastron of the optical component, the models are still rejected. If the eccentricity continues to decrease to $e = 0.01$, the models are again rejected for any longitude of periastron. Therefore, we conclude that the nominal values of the eccentricity and longitude of periastron of the optical star for $m_v = 22M_{\odot}$ and $m_v = 13.5M_{\odot}$ are $e = 0.03 \pm 0.01$ and $\omega_v = 300° \pm 30°$, clearly suggesting appreciable influence of anisotropy of the stellar wind on the observed radial-velocity curve [13, 22].

The search for the eccentricity excluding the mean radial velocities at phases 0.4–0.6 was carried out in the same way. The mass of the optical star was specified to be $22M_{\odot}$. The minimum residual satisfying the critical level was reached for $m_x = 13.7M_{\odot}$, $e = 0.01–0.02$, and $\omega_v = 300° \pm 40°$. The model is rejected at the 5% significance level for all longitudes of periastron beyond $300° \pm 40°$ and all significantly nonzero eccentricities.

Therefore, in the case $e \neq 0$, the high-accuracy radial-velocity curve of the X-ray binary likewise enables us to impose an upper constraint on the orbital inclination i in the Roche model.

7. CONCLUSIONS

The main results of this work are the relations between the masses of the optical and compact objects for orbital inclinations $i = 30°$, 35°, 40°, 45°, 55°, and 65° (Tables 3 and 4, Fig. 3) obtained in a Roche model for the optical star.

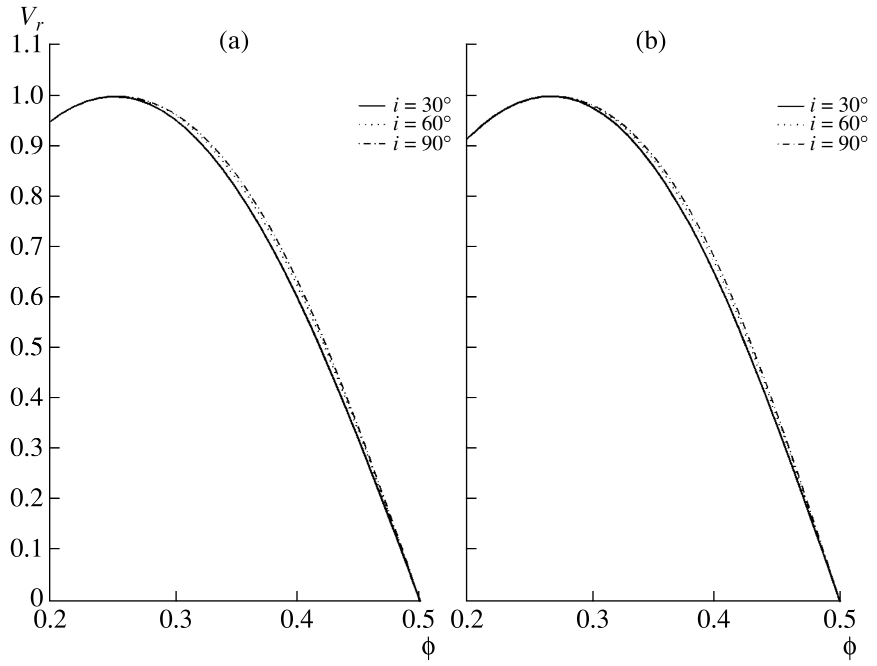

Fig. 9. The relative theoretical radial-velocity curves obtained in the Roche model for (a) $m_v = 22M_\odot$, $m_x = 11.47M_\odot$, and $e = 0.0$ for $i = 30°$, $60°$, and $90°$ and (b) $m_v = 22M_\odot$, $m_x = 11.47M_\odot$, $e = 0.05$, and $\omega_v = 90°$ for $i = 30°$, $60°$, and $90°$. The remaining parameters of the Roche model are presented in Table 2. As in the case of a circular orbit, we can see the dependence of the shape of the radial-velocity curve on the orbital inclination i when $e \neq 0$.

Another important result is the basis this work provides for estimating the orbital inclination i from the high-accuracy radial-velocity curve of an X-ray binary in a Roche model. The relations between the masses of the compact object and optical star (Fig. 3a) show that it is possible to estimate the orbital inclination when fitting the observed radial-velocity curve in a Roche model. Due to its asymmetry, the synthesized absorption profile is fairly sensitive to variations in the inclination of the binary. For nearly any mass of the optical star, the upper limit on the orbital inclination is $i = 45°$; in the particular case $m_v = 22M_\odot$, the upper limit is $i = 44°$.

The mass of the relativistic component was estimated using two independent methods. Using a B light curve of Cyg X-1 and the fit obtained in [25] and assuming the radius of the optical star to be $R_v = 17 \pm 1R_\odot$ [4], we found that the mass of the compact object should be $m_x = 8.5M_\odot$–$13.6M_\odot$. Assuming the mass of the optical component to be $22M_\odot$ and using the mass–luminosity relation for X-ray binaries [27] yields $m_x = 9.0M_\odot$–$13.2M_\odot$. Therefore, the black-hole masses derived from the radius of the optical component and the light curve and from the luminosity of the optical star are in good agreement. Since we do not know the exact orbital inclination, it is impossible to estimate the mass of the black hole in Cyg X-1 uniquely; we can specify only a range of possible masses. Based on the admissible interval of orbital inclinations, $31° < i < 44°$, the mass of the compact object in the Cyg X-1 binary should be in the range $m_x = 8.5M_\odot$–$13.6M_\odot$, which clearly exceeds the absolute upper limit on the neutron-star mass $3M_\odot$ predicted by general relativity. When the accuracy of the observed radial-velocity curve is improved, it will be possible to more accurately estimate the orbital inclination and, consequently, the black-hole mass. In addition, accurate measurements of the distance to Cyg X-1 obtained by future space astrometric observatories (such as GAIA, SIM, etc.) will provide empirical estimates of the radius of the optical star, enabling us to resolve the question of the black-hole mass in the X-ray binary Cyg X-1.

ACKNOWLEDGMENTS

This work was supported by the Russian Foundation for Basic Research (project no. 02-02-17524) and by a grant from the Program of Support for Leading Scientific Schools of Russia (project NSh-388.2003.2).

REFERENCES

1. E. A. Antokhina and A. M. Cherepashchyuk, Pis'ma Astron. Zh. **23**, 889 (1997) [Astron. Lett. **23**, 773 (1997)].
2. T. Shahbaz, Mon. Not. R. Astron. Soc. **298**, 153 (1998).

3. D. R. Gies and C. T. Bolton, Astrophys. J. **304**, 371 (1986).
4. A. Herrero, R. P. Kudritzky, R. Gabler, *et al.*, Astron. Astrophys. **297**, 556 (1995).
5. R. E. Wilson and S. Sofia, Astrophys. J. **203**, 182 (1976).
6. R. J. Brucato and R. R. Zappala, Astrophys. J. **189**, L71 (1974).
7. H. A. Abt, P. Hintzen, and S. G. Levy, Astrophys. J. **213**, 815 (1977).
8. D. R. Gies and C. T. Bolton, Astrophys. J. **260**, 240 (1982).
9. Z. Ninkov, G. A. H. Walker, and S. Yang, Astrophys. J. **321**, 425 (1987).
10. J. W. Sowers, D. R. Gies, W. G. Bagnuolo, *et al.*, Astrophys. J. **506**, 424 (1998).
11. J. LaSala, P. A. Charles, R. A. D. Smith, *et al.*, Mon. Not. R. Astron. Soc. **301**, 285 (1998).
12. C. Brocksopp, A. E. Tarasov, V. M. Lyuty, and P. Roche, Astron. Astrophys. **343**, 861 (1999).
13. M. K. Abubekerov, E. A. Antokhina, and A. M. Cherepashchuk, Astron. Zh. **81**, 1 (2004) [Astron. Rep. **48**, 89 (2004)].
14. H. Quantrell, A. J. Norton, T. D. C. Ash, *et al.*, Astron. Astrophys. **401**, 313 (2003).
15. A. M. Cherepashchuk, N. A. Katysheva, T. S. Khruzina, and C. Yu. Shugarov, *Highly Evolved Close Binary Stars: Catalog* (Netherland Gordon and Breach Sci., 1996), Vol. 1, Part 1, p. 82.
16. E. A. Antokhina, Astron. Zh. **73**, 532 (1996) [Astron. Rep. **40**, 483 (1996)].
17. A. A. Rubashevskiĭ, Astron. Zh. **68**, 799 (1991) [Sov. Astron. **35**, 626 (1991)].
18. M. H. van Kerkwijk, J. van Paradijs, and E. J. Zuiderwijk, Astron. Astrophys. **303**, 497 (1995).
19. K. Makishima, K. Koyama, S. Hayakawa, and F. Nagase, Astrophys. J. **314**, 619 (1987).
20. J. P. Zahn, Astron. Astrophys. **57**, 383 (1977).
21. J. P. Zahn, Astron. Astrophys. **220**, 112 (1989).
22. M. Milgrom, Astron. Astrophys. **70**, 763 (1978).
23. D. Hudson, *Statistics. Lectures on Elementary Statistics and Probability* (Geneva, 1964; Mir, Moscow, 1970).
24. A. M. Cherepashchuk, Astron. Zh. **70**, 1157 (1993) [Astron. Rep. **37**, 585 (1993)].
25. N. I. Balog, A. V. Goncharskiĭ, and A. M. Cherepashchuk, Pis'ma Astron. Zh. **7**, 605 (1981) [Sov. Astron. Lett. **7**, 336 (1981)].
26. J. Ziolkowski, *Nonstationary Evolution of Close Binaries,* Ed. by A. N. Zitkov (PWN, Warsaw, 1978), p. 29.
27. M. K. Abubekerov, Astron. Zh. (2004, in press).
28. A. V. Goncharskiĭ, A. M. Cherepashchuk, and A. G. Yagola, *Incorrect Problems in Astrophysics* (Nauka, Moscow, 1985), p. 54 [in Russian].

Translated by Yu. Dumin

Astronomy Reports, Vol. 48, No. 7, 2004, pp. 563–576. Translated from Astronomicheskiĭ Zhurnal, Vol. 81, No. 7, 2004, pp. 620–634.
Original Russian Text Copyright © 2004 by Shimanskiĭ, Borisov, Sakhibullin, Surkov.

The Nature of the Unique Precataclysmic Variable V664 Cas with Two-Peaked Balmer Lines in Its Spectrum

V. V. Shimanskiĭ[1], **N. V. Borisov**[2], **N. A. Sakhibullin**[1], **and A. E. Surkov**[2]

[1]*Kazan State University, Kazan, Russia*
[2]*Special Astrophysical Observatory, Russian Academy of Sciences, Nizhniĭ Arkhyz, Karachaĭ-Cherkessian Republic, 357147 Russia*

Received August 1, 2003; in final form, January 9, 2004

Abstract—We analyze photometric and spectroscopic observations of the close binary system V664 Cas. All the characteristics of its radiation are consistent with the star being a cataclysmic variable with powerful reflection effects. The orbital period is refined ($P = 0.5816475$ d) and the ephemerides of the system determined. The U, B, V, R light curves of V664 Cas display sinusoidal variations with similar amplitudes near $\Delta m = 1.1^m$. This suggests that a hot spot on the surface of the secondary always dominates the optical radiation of the system. The spectra contain emission lines, two-peaked hydrogen lines, and narrow lines of helium and heavy elements in high ionization states, whose intensities vary synchronously with the brightness. The HeII λ4686 Å line has broad absorption wings that form in the atmosphere of the O subdwarf. The mass function, $f(m) = 0.007M_\odot$, is the lowest among all precataclysmic variables: the mass of the secondary exceeds the mass of the primary by more than a factor of 1.6. A full set of fundamental parameters for V664 Cas is determined based on modeling of the spectra and light curves, taking into account reflection effects in the system. Most of the emission lines are formed under conditions of appreciable deviations from local thermodynamic equilibrium. The possibility of carrying out correct modeling of the Balmer-line profiles assuming the stellar radiation is absorbed in a planetary nebula is demonstrated. *© 2004 MAIK "Nauka/Interperiodica".*

1. INTRODUCTION

Precataclysmic variables form a class of close detached binary systems containing hot subdwarfs or white dwarfs together with low-luminosity late-type stars [1]. The grouping together of systems of these types by Ritter [1] turned out to be fully justified, since this class includes objects in a general, intermediate phase of their evolution, between systems with common envelopes, on the one hand, and cataclysmic variables, on the other.

However, it is now usual to divide the class of precataclysmic variables into three groups of objects, which have appreciably different spectra and variability amplitudes, as well as different types of primary components. The first group includes old precataclysmic variables containing cooling white dwarfs (in which more than 10^6 yrs have passed since the ejection of their common envelopes), while the second and third groups include young precataclysmic variables containing hot, low-luminosity sdB and sdO subdwarfs. It is clear from models of the evolution of the primaries of precataclysmic variables [2] that the first group should contain many more systems than the second group and even moreso than the third group. This has been confirmed by the statistics of discovered new objects: among precataclysmic variables found since the middle of the 1990s, more than 70% are old systems. In addition, scaled spectroscopic studies of weak blue stars have made it possible to appreciably expand the list of precataclysmic variables containing sdB subdwarfs. One example of the progress that has been made in this area is the work of Morales-Rueda *et al.* [3], who determined the orbital periods of 22 close binary systems, of which about 20% are likely precataclysmic variables. Note also that, in most cases, studies have not been restricted to the discovery of new objects, and various multifaceted analyses of these systems have been carried out aimed at determining the largest possible sets of parameters for the systems.

In contrast, progress in connection with the detection and investigation of young precataclysmic variables containing hot ($T_{eff} > 60\,000$ K) sdO subdwarfs has been relatively modest. For example, only one or two systems of this type were discovered from 1985 to 2002 (TW Crv [4] and HS 1136+6646 [5]), with parameters being determined only for two previously known systems (BE UMa and UU Sge). The absence of more substantial progress in this area is only partly explained by the relatively small number of young precataclysmic variables in the Galaxy, since their high luminosities and the unique characteristics of their radiation (high variability amplitudes $\Delta m > 0.5^m$, numerous emission lines, and their association with planetary nebulas) help make them comparatively easy to study. Expansion of the list of well-studied objects in this group has been appreciably hindered by the disproportionate attention paid to certain individual stars. It suffices to point out that, at present, results have been published for nine studies of BE UMa, five studies of UU Sge, and only four (!) studies of other systems. The five stars identified by De Kool and Ritter [6] as promising young precataclysmic variable candidates (V664 Cas, VW Pyx, and the cores of the nebulas Abell 65, SP1 and Ht Tr4) remained virtually unstudied up to 2000. However, as is demonstrated by the results of Exter *et al.* [7], some of these objects have properties that were discovered for the first time among precataclysmic variables, in terms of both the parameters of their components and their characteristic radiation. This makes observations and analyses of the remaining candidate precataclysmic variables with sdO primaries topical.

V664 Cas was first discovered as the core of the planetary nebula HFG1 by Heckathorn and Fesen [8], who estimated the effective temperature of the subdwarf to be $T_{eff} = 50\,000{-}60\,000$ K. High-amplitude variability with $\Delta m_B \approx 1.1^m$ and an orbital period of $P_{orb} = 0.5816^{\rm d}$ were found by Grauer *et al.* [9], who also noted the presence of numerous emission lines in the spectrum of the system. Grauer *et al.* [9] proposed that V664 Cas was a close, detached system that had finished its common-envelope stage, i.e., it was a precataclysmic variable. Later, based on low-resolution spectra, Acker and Stenholm [10] classified this object as a polar with a prolonged orbital period. However, V664 Cas is listed as a precataclysmic variable in the subsequent catalog of Ritter and Kolb [11], in agreement with the photometric observations of [12, 13]. Thus, there has been no conclusive determination of the evolutionary status of this system, and no estimates of its parameters have been published.

We carried out photometric and spectroscopic observations of V664 Cas at various phases of its orbital period. We show that the star is a young precataclysmic variable with an unusual component-mass ratio for systems of this type. Section 2 contains a brief description of the observations and data-reduction methods used. In Section 3, we present the observed spectra, light curves, and radial-velocity curves of the system, together with the results of our analysis of these data. We derive a full set of fundamental parameters for V664 Cas based on theoretical modeling of the system's radiation in Section 4. Section 5 contains a discussion of the various features of the object's spectra, including its unique, two-peaked Balmer lines.

2. OBSERVATIONS

2.1. Photometry

Our photometric observations of V664 Cas were carried out on a three-channel, rapid B, V, R electrophotometer mounted on the 70-cm telescope of the Kourov Astronomical Observatory. The brightness of the system was measured over three nights in March 2000, in parallel in the B and R filters, with exposure times of 2.5 min. We also simultaneously made observations of a number of field stars with $m_V = 13^m{-}15^m$ in order to exclude variations of the brightness of V664 Cas due to variations in the observing conditions. The total duration of the three sets of observations was about 23 h, and the observations encompass all phases of the orbital period. The mean error in a single brightness measurement was $\Delta m_{B,R} = 0.02^m$.

2.2. Spectroscopy

Our spectroscopic observations of V664 Cas were carried out on the 6-m telescope of the Special Astrophysical Observatory using a long-slit spectrograph [14] and a 1024×1024 Photometrics CCD (with pixel size $24 \times 24 \mu$m) mounted at the prime focus. The observations were obtained on August 26–28, 2001, March 23, 2002, and August 16, 2002. In all cases, a diffraction grid with 1302 lines/mm was used, providing a dispersion of 1.2 Å/pixel. We chose to observe the wavelength range $\Delta\lambda = 3930{-}5100$ Å, which contains the maximum number of emission lines of hydrogen and heavy elements. The size of the stellar images did not exceed $2.3''$, which determined the resulting resolution of the spectra of V664 Cas, $\Delta\lambda = 2.9$ Å. On each night from August 26 to 28, 2001, we obtained six individual successive spectrograms with exposures of 180 s, while four spectrograms with exposures of 300 s were obtained on each of the nights of March 23 and August 16, 2002. The mean signal-to-noise ratio for the August 2001 and August 2002 spectrograms was $s/n = 45{-}75$. The March 23 observations were carried out under unfavorable conditions, resulting in a lower signal-to-noise ratio, $s/n \approx 20$, and could be used only for the radial-velocity analysis. For use in the calibration of the wavelength scale and flux level in the radial-velocity analysis, we also obtained spectra of an ArNeHe lamp, the spectrophotometric standard

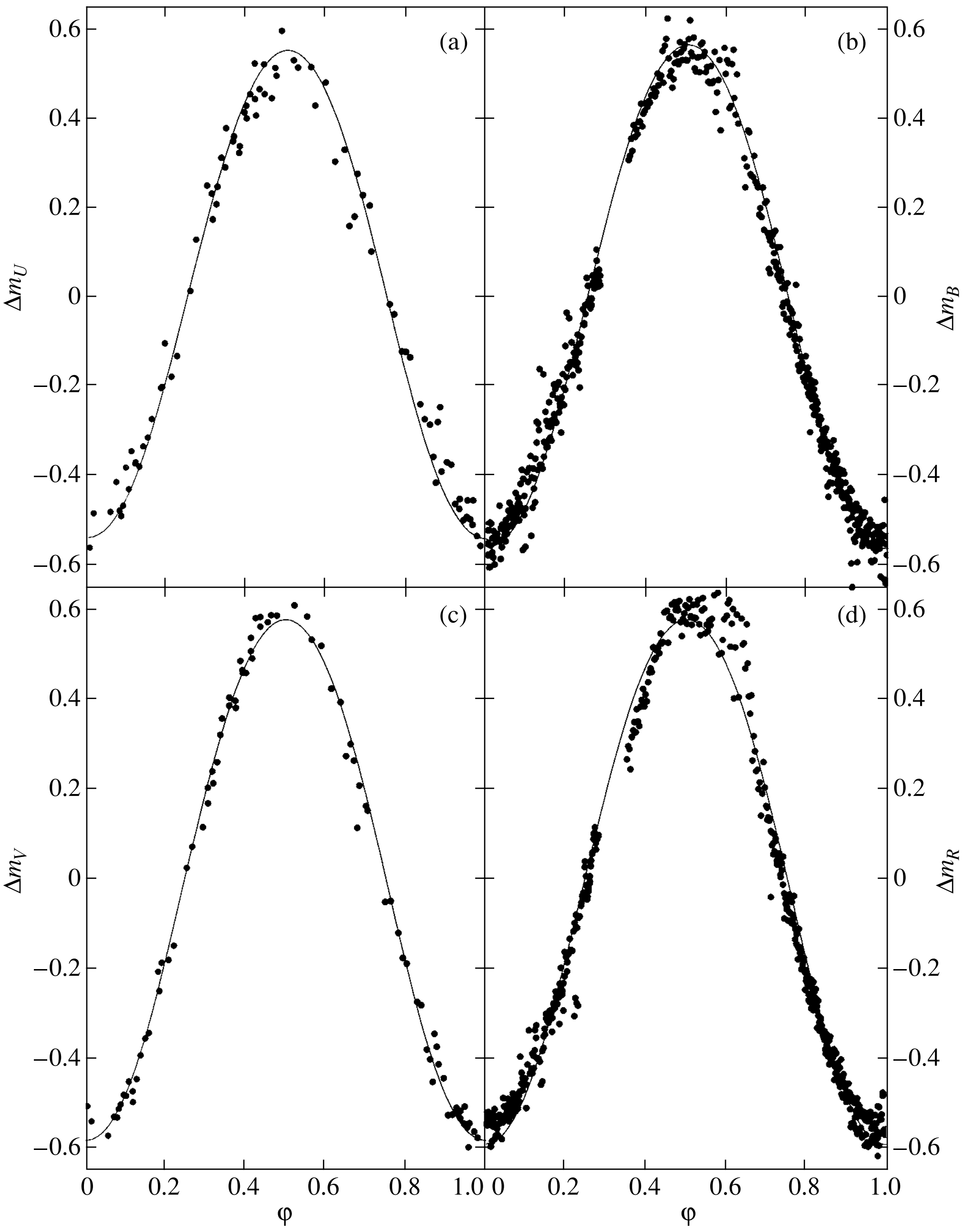

Fig. 1. Observed (circles) and theoretical (solid curves) light curves for V664 Cas in the (a) U, (b) B, (c) V, and (d) R bands.

BD+28 2106 from the survey [15], and the precataclysmic variable BE UMa. A log of the observations is presented in Table 1, which contains data on the Julian dates of the observing epochs JD, the orbital phases φ according to our own ephemerides (see below), and the measured heliocentric radial velocities of the secondary $V_r(obs)$.

The reduction of the spectrograms was carried out using standard techniques in the MIDAS package [16].

3. CHARACTERISTICS OF THE RADIATION OF V664 Cas

3.1. Light Curves and Ephemerides

A preliminary analysis of our B-band photometric observations of V664 Cas showed that the amplitude of the brightness variations was identical to that for the data of [12]. This enabled us to use our data jointly with the data of [12] to construct the light curves of V664 Cas and determine the ephemerides of the system. We used the value HJD 2451470.5241

Table 1. Spectroscopic observations of V664 Cas. JD is Julian date; φ, orbital phase; and s/n and V_r, the signal-to-noise ratio and heliocentric radial velocity of the secondary for the averaged spectrograms

JD 2452000+	φ	s/n	V_r, km/s	JD 2452000+	φ	s/n	V_r, km/s
149.455	0.760	109	−4.0	149.469	0.784	103	0.5
149.460	0.768			149.472	0.790		
149.465	0.776			149.476	0.797		
150.377	0.345	140	92.9	150.389	0.366	127	89.3
150.381	0.351			150.392	0.371		
150.385	0.358			150.397	0.379		
151.366	0.045	78	58.4	151.381	0.072	84	56.9
151.374	0.058			151.385	0.079		
151.378	0.066			151.390	0.086		
356.333	0.437	44	62.3	503.510	0.471	101	55.3
356.337	0.443			503.514	0.478		
356.341	0.450			503.518	0.485	108	48.1
356.345	0.457			503.522	0.491		

obtained in [13] for the epoch of maximum brightness as a check. The total interval covered by the observations was 2360 days, which enabled us to derive the orbital period with an accuracy of about $0.000002^{\rm d}$. Our analysis yielded the following ephemerides for V664 Cas:

$$\mathrm{JD} = 2451623.059(\pm 0.001) + 0.5816475(\pm 0.0000022)E,$$

where $E = 0.0$ corresponds to the minimum reflection effects. U, B, V, and R light curves calculated using this ephemerides are presented in Fig. 1. Approximation of the light curves by the three-parameter relations

$$m = A + B\cos\varphi + C\cos 2\varphi$$

showed that $C/B < 0.02$ for all the bands studied. The very small value of the coefficient C testifies to the weakness of effects due to asphericity of the components of V664 Cas. As has been noted earlier [9, 13], the total amplitudes of the brightness variations Δm are nearly the same over the entire visible spectrum: $\Delta m_B = 1.12^m$, $\Delta m_V = 1.15^m$, and $\Delta m_R = 1.15^m$. Note also the similar value $\Delta m_I = 1.12^m$ obtained in [13] for the infrared variations. The stability of the brightness-variation amplitude over a broad spectral interval suggests that the radiation of V664 Cas is dominated by the flux of a hot spot observed at various projections, i.e., that the orbital inclination is small. The contribution of the primary begins to appreciably increase only at the frequencies of the Balmer continuum, since the U-band amplitude is $\Delta m_U = 1.03^m$.

3.2. Spectra

Figure 2 presents averaged, normalized spectra of V664 Cas for several orbital phases, while Fig. 3 presents a mean spectrum with $s/n \approx 280$ for phases near maximum brightness, $\Delta\varphi = 0.25$–0.75, obtained by adding the individual spectrograms taking into account their radial velocities (see below). The mean spectrum of the precataclysmic variable BE UMa for phases $\Delta\varphi = 0.40$–0.60 is presented for comparison. The spectra of V664 Cas contain numerous emission lines of hydrogen, helium, and heavy elements in high ionization states, whose intensity varies synchronously with the brightness variations. Our identifications of the lines observed in the mean

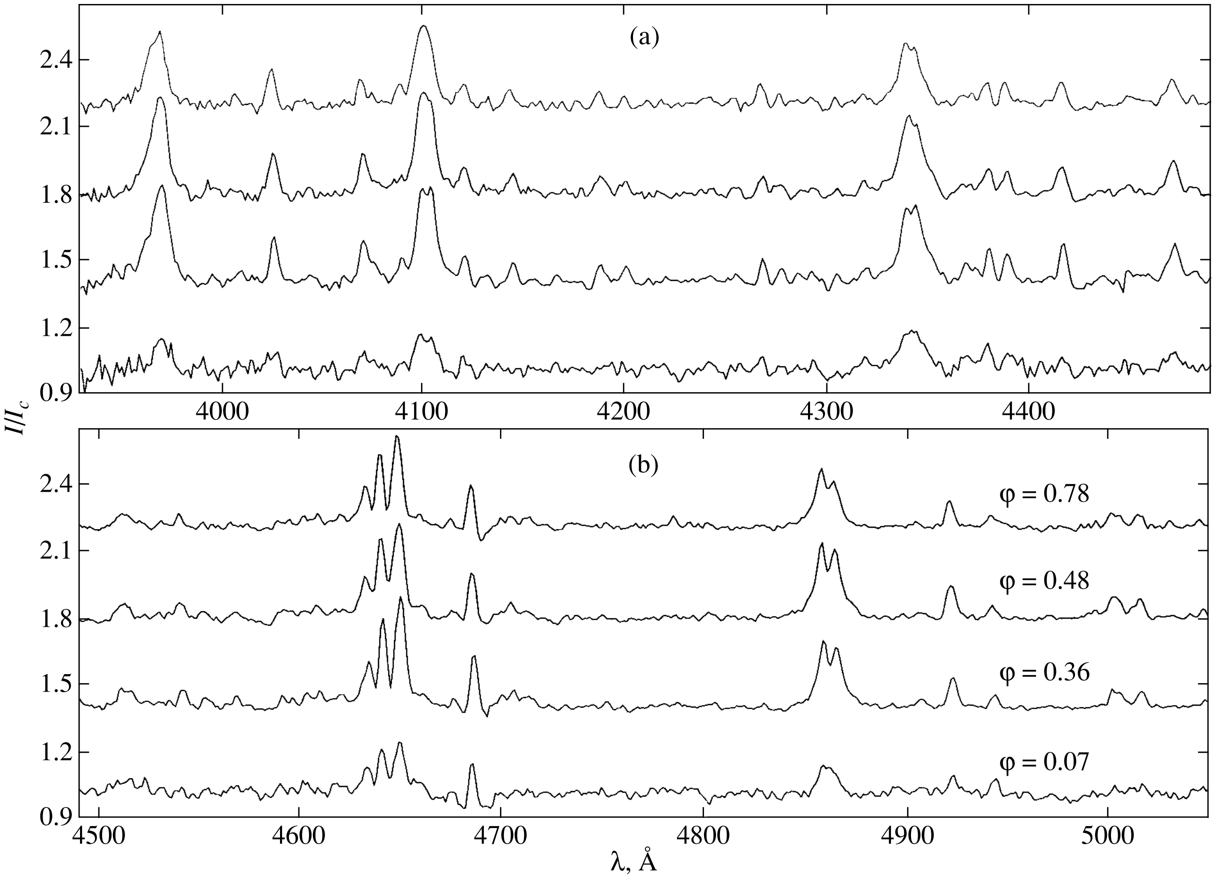

Fig. 2. Normalized observed spectra of V664 Cas for orbital phases $\varphi = 0.78, 0.48, 0.36$, and 0.07. The spectra are successively shifted along the vertical axis by 0.2.

spectrum and data on their equivalent widths W_λ are presented in Table 2. The initial identifications were based on synthetic spectra calculated using the SYNTH program and the model atmosphere of Kurucz with $T_{eff} = 26\,000$ K, $\log g = 4.0$, and $[A] = 0.0$ [17]. After determining the parameters of V664 Cas (see below), we carried out a new identification of the observed lines using the resulting synthetic spectra for the system.

Overall, the spectra of the two cataclysmic variables have a similar set of emission lines, which confirm that the lines in V664 Cas are formed under the action of reflection effects in the vicinity of a hot spot on the secondary. The lower intensity of the lines of metals and helium in the spectra of V664 Cas is due primarily to the lower amplitude of reflection effects for these lines. Therefore, we suggest that the chemical composition of the secondary does not differ qualitatively from that of the secondary of BE UMa, which has been shown by Ferguson *et al.* [18] to be close to the solar composition. However, comparison of our set of W_λ values for V664 Cas with the analogous data of [19] for BE UMa reveals an enhancement of the lines of NII, NIII, MgII, and SiIII relative to those of OII, CII, and CIII, which may provide evidence for overabundances of nitrogen, magnesium, and silicon. As was analyzed earlier in [20], these overabundances are associated with the accretion of material from the primary enriched in the products of nuclear synthesis onto the surface of the secondary during the common-envelope phase. Overall, the presence of lines of highly ionized ions in the spectra enables us to obtain a preliminary estimate of the atmospheric temperature of the plasma in the hot spot, $\Delta T_e = 19\,000{-}25\,000$ K.

All the emission lines of helium and heavy elements have half-widths $\Delta\lambda < 3.4$ Å, determined primarily by the instrumental function of the spectrograph. Analysis of the profiles of the narrowest unblended lines yielded an upper limit for the rotational velocity of the secondary of about $V \sin i = 35$ km/s. The broad absorption wings of the HeII λ4686 Å line ($\Delta\lambda \approx 20$ Å) are shifted from the emission core and do not change their intensity with orbital phase (Fig. 2). This is consistent with the suggestion by

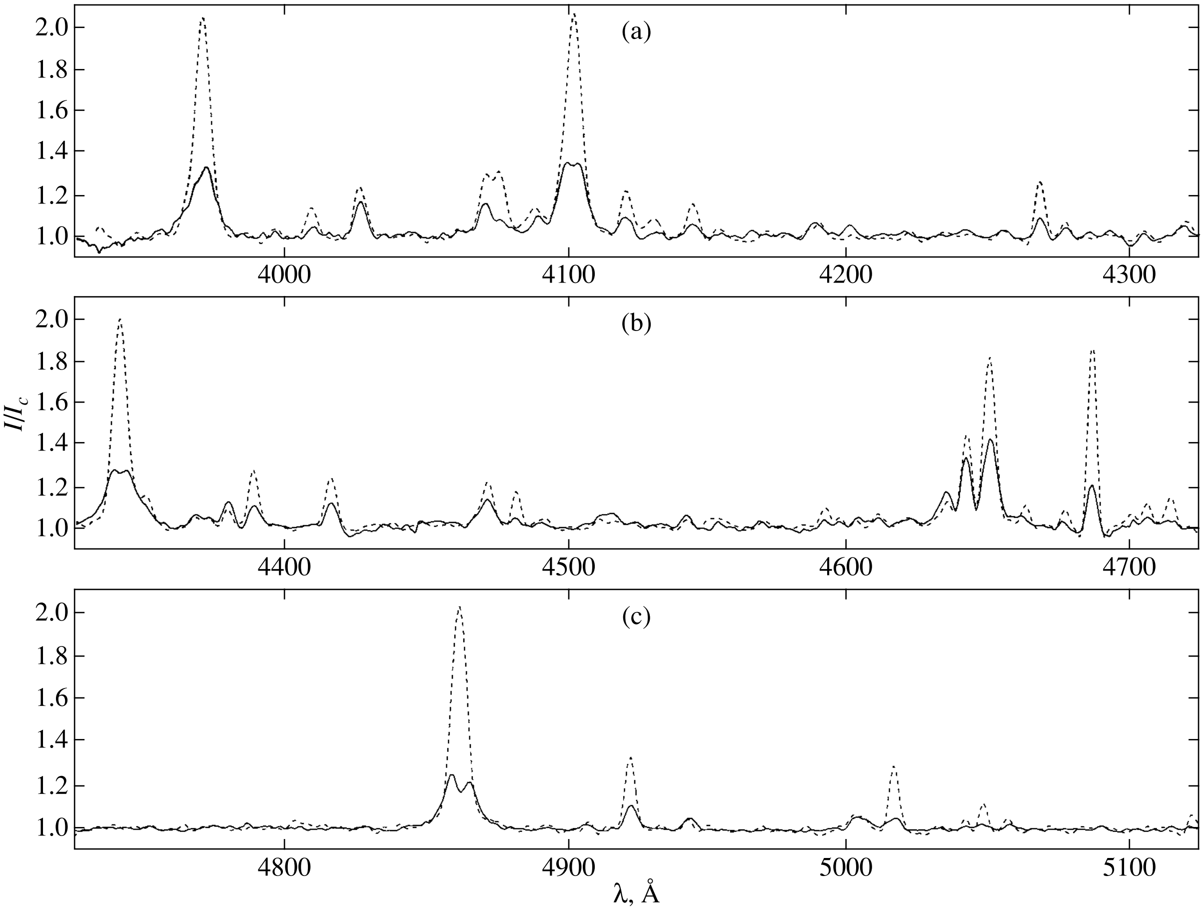

Fig. 3. Mean observed spectra of V664 Cas (solid curve) and BE UMa (dashed curve) for phases $\Delta\varphi = 0.25{-}0.75$.

Exter *et al.* [21], who detected similar HeII absorption wings in spectra of the precataclysmic variable VW Pyx, that these features are formed in the hot star. However, the weakness of the absorption wings and the distortion brought about by the emission core prevents us from reliably measuring the radial velocity of the primary.

As we can see in Figs. 2 and 3, one distinguishing feature of the spectra of V664 Cas is the presence of broad, two-peaked Balmer lines. The widths of the emission wings of these lines are 10–15% larger than those in the spectra of BE UMa and correspond to velocity dispersions of $\Delta V_l = 900$ km/s. The strong Stark broadening of the Balmer lines testifies to their formation in dense layers of the secondary's atmosphere where the surface gravity is equal to or exceeds the value $\log g = 3.95$ determined by Ferguson *et al.* [22] for the red dwarf in the BE UMa system. Our analysis of the central dips in the Hβ, Hγ, and Hδ lines shows that their wavelength does not vary with the orbital period and, thus, they move through the observed emission profiles. As a consequence, the central dips in Fig. 3 are clearly visible only in the Hβ line, whose intensity is maximum. The distance between the two emission peaks for all the two-peaked lines corresponds to a velocity difference of $\Delta V_l = 300{-}340$ km/s, which is smaller than the characteristic value for cataclysmic variables. We will consider possible origins of the two-peaked Balmer lines below.

3.3. Radial Velocities

The large number of emission lines observed against the background of the flat continuum and their small widths enable us to determine the radial velocity of the cool star V_l via a cross-correlation analysis of the spectra. This analysis requires the use of comparison spectra with similar sets of lines with similar intensities. For a preliminary radial-velocity analysis, we used spectra of the precataclysmic variable BE UMa, which is an excellent spectroscopic analogue of V664 Cas (Fig. 3) and has a well-studied radial-velocity curve. Further, after finding the parameters of the system and numerical modeling

Table 2. Identified lines in the spectrum of V664 Cas (W_λ is the measured equivalent width in the mean spectrum)

λ, Å	W_λ, Å	Identification	λ, Å	W_λ, Å	Identification
3945	0.240	OII(3945)	4471	1.110	HeI(4471),
3970	5.010	Hϵ, He(3964)			OII(4465, 4467, 4469)
3995	0.120	NII(3995)	4481	0.260	MgII(4481, 4481),
4009	0.235	HeI(4009)			AlIII(4479, 4479)
4026	0.970	HeI(4026)	4489	0.090	OII(4488, 4489, 4489)
4042	0.200	NII(4041, 4043)	4514	0.630	NIII(4510), OII(4514),
4060	0.130	OII(4060, 4061)			CIII(4515, 4516)
4070	1.120	OII(4069, 4069, 4072)	4522	0.110	NeII(4522), NIII(4523)
4088	0.480	OII(4089), SiIV(4088)	4529	0.090	NII(4530),
4102	5.370	Hδ			AlIII(4528, 4529)
4120	0.530	HeI(4120),	4541	0.360	HeII(4541)
		OII(4119, 4120, 4121)	4552	0.170	SiIII(4552)
4131	0.095	OII(4132)	4568	0.230	SiIII(4567)
4144	0.430	HeI(4143),	4591	0.190	OII(4591)
		OII(4141, 4142, 4145)	4596	0.210	OII(4596)
4153	0.110	OII(4153), CIII(4152)	4602	0.240	OII(4602), NII(4601)
4163	0.070	CII(4162)	4609	0.310	OII(4609), NII(4607)
4169	0.080	HeI(4168), OII(4169)	4619	0.280	CII(4618, 4619)
4187	0.460	OII(4185, 4189)	4632	1.170	NII(4630), SiIV(4631, 4631)
4199	0.310	HeII(4199),	4640	1.490	OII(4638, 4641), NIII(4640)
		NII(4199), NIII(4200)	4649	2.870	OII(4649, 4650),
4211	0.025	SiIV(4211)			CIII(4647, 4650, 4451)
4219	0.040	NeII(4219)	4661	0.410	OII(4661)
4241	0.190	NII(4241)	4676	0.110	OII(4676)
4253	0.160	OII(4253, 4254)	4686	0.850	HeII(4685)
4267	0.410	CII(4267)	4705	0.260	OII(4705)
4276	0.260	OII(4275, 4276, 4276, 4277)	4713	0.480	HeI(4713)
4285	0.140	OII(4283)	4751	0.100	OII(4751)
4291	0.220	OII(4291)	4787	0.110	NII(4788)
4303	0.110	OII(4302, 4303, 4303, 4303)	4803	0.100	NII(4803)
4318	0.310	OII(4317, 4319, 4319)	4828	0.055	SiIII(4828)
4340	4.640	Hγ	4862	4.260	Hβ
4367	0.170	OII(4366, 4369)	4906	0.170	OII(4906)
4372	0.190	CII(4372, 4372)	4922	0.780	HeI(4921)
4378	0.490	OII(4378, 4378)	4942	0.310	OII(4941, 4943)
4388	0.410	HeI(4387)	4993	0.085	NII(4994)
4415	0.810	OII(4414, 4416)	5003	0.660	NII(5001, 5001, 5005)
4435	0.190	HeI(4437), NII(4432)	5015	0.390	HeI(5015)
4448	0.300	OII(4446, 4448, 4448),	5047	0.120	HeI(5047), NII(5045)
		NII(4447)	5090	0.110	SiIII(5091, 5091)

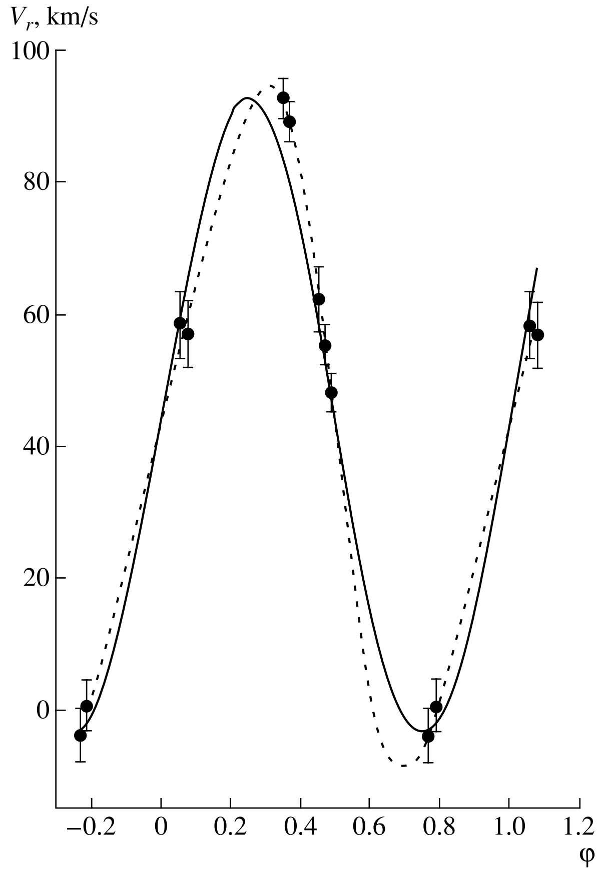

Fig. 4. Radial-velocity curves for the V664 Cas secondary. The solid and dashed curves show approximations for models with a circular and elliptical orbit, respectively.

of its spectra (see below), we revised the V_l values using the new theoretical spectra. We accurately took into account the radial velocities of various parts of the surfaces of both components when computing these spectra. This enabled us to determine values of V_l for the center of mass of the secondary, which differ from the values $V_l^{'}$ obtained using the Doppler shifts of the emission lines. This difference arises exclusively during the formation of emission lines in the zone of a hot spot on the surface of an irradiated star with a high rotational velocity. Therefore, it is important to take into account the rotational velocity of the secondary when deriving its radial velocities. Since we established earlier the upper limit $V \sin i \sim 35$ km/s, our subsequent theoretical modeling used the fixed value $V \sin i = 30$ km/s. Note that this rotational velocity is substantially lower than the velocity that would be synchronous with the orbital motion, but, as we will show below, our choice of $V \sin i$ has a reasonably firm physical basis.

The V_l values were computed by minimizing the integral

$$\int_{\lambda_1}^{\lambda_2} (I_\lambda^1 - 1)(I_\lambda^2 - 1)\, d\lambda, \qquad (1)$$

where I_λ^1 and I_λ^2 are the intensities in the normalized comparison spectra and the spectra of the studied star, and the integration is carried out over the entire spectral range studied. To avoid possible errors in V_l due to the unusual two-peaked profiles of the Balmer lines, we excluded portions of the spectrum within $\Delta\lambda = 2.5$ Å of the centers of these lines from the analysis. To increase the accuracy of the V_l values, we determined them using spectra summed from all of the three spectograms for August 2001, the two spectrograms for August 2002, and all the spectrograms for March 2002. This yielded nine heliocentric radial velocities for the secondary, presented in Table 1 and Fig. 4. We estimate the accuracy of the V_l values to be $\sigma = 3$–6 km/s, depending on the signal-to-noise ratios in the spectra.

Our analysis of the radial-velocity curve for the secondary using a model with a circular orbit showed substantial deviations (to $\Delta V_l = 10$ km/s) of the approximating sinusoid from the observational data. We therefore constructed an alternative V_l curve using a model with an elliptical orbit. Note that the sinusoidal shape of the observed light curves does not rule out the possibility of an elliptical orbit, since such a shape could come about if the orbit's perigee is near phase $\varphi = 0.0$ or 0.5 and the inclination of the orbit is small. Table 3 presents the results of our analysis of V_l for both orbits, while Fig. 4 shows the resulting theoretical curves.

It is clear that using the elliptical-orbit model makes it possible to bring the approximation curve into agreement with the observational data within the likely errors σ. The orbital eccentricity obtained in this case ($e = 0.09$) is admissible for close binary systems that have passed through a common-envelope stage, and the passage of the perigee point indeed coincides with phase $\varphi = 0.5$. However, we consider the hypothesis that the orbit is circular to be preferable, since no other precataclysmic variables with appreciable orbital eccentricities ($e > 0.05$) have been found. Further spectral observations of V664 Cas are required to resolve the question of the shape of its orbit.

We obtained similar radial-velocity amplitudes for the secondary in both models ($K_r = 48.7$ and 49.2 km/s), which correspond to the mass function

$$f(m) = \frac{M_1^3}{(M_1 + M_2)^2} \sin^3 i = (0.0068\text{–}0.0072) M_\odot. \qquad (2)$$

Since the V664 Cas primary is the core of a planetary nebula with a minimum mass of $M_1 = 0.55 M_\odot$ [2], this value of $f(m)$ provides unambiguous evidence for a large secondary mass, even if the orbital inclination is close to $i = 30°$. Based on their determination of $f(m) = 0.05 M_\odot$ for VW Pyx, Exter *et al.* [21] studied in detail the possible existence of precataclysmic variables whose secondaries have masses equal to or exceeding their primary masses. Although they concluded that there was not a sufficiently firm basis for this hypothesis, we consider this to be a realistic possibility, since the component-mass ratios for the FF Aqr and V471 Tau systems have been reliably determined to be $q = 0.25$ [23] and $q = 0.89$ [24]. Therefore, supposing that $M_1 = 0.55{-}0.60 M_\odot$ and $i = 26°{-}30°$, we obtain the estimates $q = 0.48{-}0.62$ and $M_2 = 0.90{-}1.30 M_\odot$.

4. PARAMETERS OF V664 Cas

The modest inclination of the V664 Cas orbit and the deficiency of observational data on the primary in the system seriously hinder the derivation of the fundamental parameters of this star. The only means for finding these parameters is modeling the reflection effects in the light curves and spectra of the system. Therefore, we carried out an analysis of the reflection effects based on computed models of irradiated stellar atmospheres [25, 26]. The version of the SPECTR program we used, which realized this method, was identical to that used earlier to study the old precataclysmic variables MS Peg and LM Com [27]. It is designed for computations of models of irradiated atmospheres, taking into account radiation from local areas on the surfaces of both stars and the incident flux from the neighboring component [26]. We computed the specific intensity I_λ of the radiation emitted at various angles to the surface in the wavelength interval $\Delta\lambda = 3000{-}11000$ Å in steps of $\Delta\lambda = 0.04$ Å. The I_λ values were found including the continuous sources of opacity specified in the SPECTR package [25], 530 000 lines from the list [17], and the molecular bands derived by Ya. Pavlenko in accordance with the theory of Nersisyan *et al.* [28]. The resulting theoretical spectra of V664 Cas were computed by summing the specific intensities of all areas at each of 72 orbital phases, taking into account their sizes, visibilities, and radial velocities relative to an observer. The resulting spectra were convolved with the instrumental function of the spectrograph, and theoretical light curves were obtained by convolving with the transmission curves in the Johnston system, in accordance with the data of [29]. Preliminary computation of the atmosphere models for blue subdwarfs with $T_{eff} = 60\,000{-}110\,000$ K and $\log g = 5.5{-}6.2$ were carried out using the BINARY3 code [30].

Table 3. Parameters of V664 Cas (the subscripts 1 and 2 denote quantities obtained for models with a circular and elliptical orbit)

Parameter	Component	
	primary	secondary
P_{orb}, days	0.5816475 ± 0.0000022	
JD(φ_0)	$2\,451\,623.059 \pm 0.001$	
K, km/s		$48.7^1 \pm 1.2$
		$49.2^2 \pm 1.0$
γ, km/s		$43.3^1 \pm 0.9$
		$42.8^2 \pm 0.9$
e	0.09 ± 0.01	
ω	$177° \pm 5°$	
q	0.52 ± 0.02	
T_{eff}, K	$83\,000 \pm 6000$	5400 ± 500
$\log g$	5.65 ± 0.05	4.23 ± 0.06
$M/M_\odot$	0.57 ± 0.03	1.09 ± 0.07
$R/R_\odot$	0.19 ± 0.02	1.30 ± 0.08
$A/R_\odot$	3.37 ± 0.06	
i	$28° \pm 2°$	

The computation of the spectra of the system using this method requires that the effective temperatures, masses, radii, orbital and rotational velocities of the components, and the semimajor axis and inclination of the orbit be specified. Our test computations showed that, when modeling the reflection effects in V664 Cas, the determining factor is the temperature of the blue subdwarf. Based on an analysis of ultraviolet spectra of the object, Heckathorn and Fesen [8] derived the estimate $T_{eff} = 50\,000{-}60\,000$ K but pointed out the strong effect of interstellar extinction and the planetary nebula on their results. This temperature cannot reproduce the observed amplitudes of the brightness variations for any values of the remaining parameters without the addition of accretion or eclipses. We therefore concluded that the temperature and luminosity of the primary are higher than is indicated by the data of [8]. As a result, the volume of analyzed observational data for V664 Cas is insufficient for a direct determination of the system's parameters, and we additionally made use of the evolutionary tracks for hot subdwarfs of [2], which

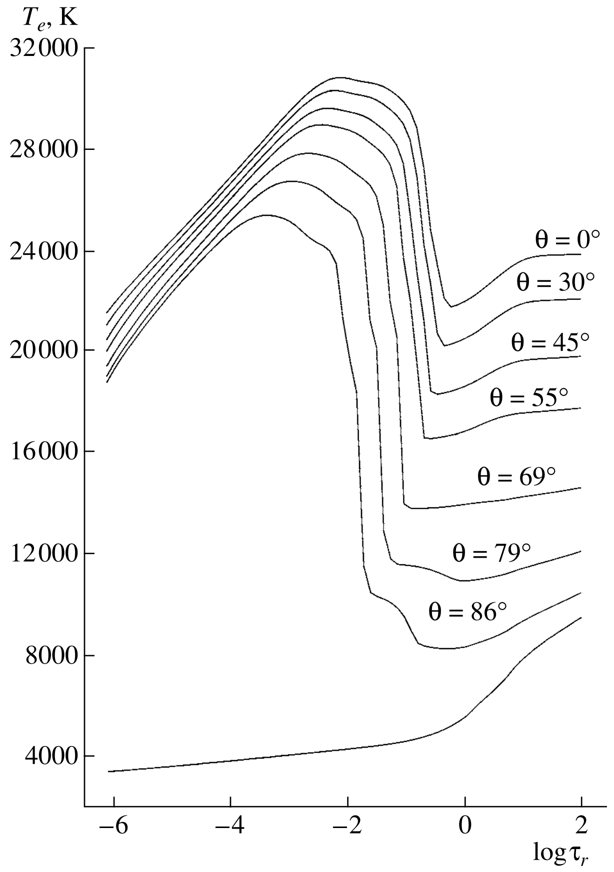

Fig. 5. Distribution of the temperature T_e with the Rosseland opacity τ_r in the atmosphere of the secondary for various points inside and outside the hot spot. The numbers indicate the angle of incidence of the external radiation.

relate the stars' temperature and luminosity with their mass. When searching for the optimal parameters for V664 Cas, we tried to reproduce the observed amplitudes and shapes of the light curves in all bands, the mass function $f(m) = 0.007M_\odot$, and the estimated temperature in the hot-spot zone $\Delta T_e \approx 23\,000$ K found earlier. The resulting parameters are presented in Table 3, the corresponding theoretical light curves in Fig. 1, and the temperature structure of the secondary atmosphere at various points inside and outside the hot spot in Fig. 5.

We can see from Table 3 that the mass of the V664 Cas primary occupies an intermediate position between ordinary blue sdB subdwarfs and the most massive sdO subdwarfs encountered in precataclysmic variables, in BE UMa, UU Sge, and KV Vel. The nearest analogue is the subdwarf in V477 Lyr, which has a mass of $M_1 = 0.52M_\odot$ and $T_{eff} = 60\,000$ K. According to [2], such objects should be formed in the evolution of stars with initial masses $M \approx 3.0M_\odot$ over a time $T = 3 \times 10^8$ yrs. This suggests that V664 Cas belongs to the thin disk of our Galaxy, in agreement with the high abundance of heavy elements in the atmosphere of the G star.

The question of the current physical state of the V664 Cas secondary requires a separate discussion, since the derived mass of this component depends strongly on the adopted rotational velocity. Our use of the value $V \sin i = 30$ km/s, which provides an enhancement in the radial-velocity amplitude by $\Delta K_r = 9.4$ km/s, yields a mass for the G star of about $M_2 = 1.1M_\odot$. In this case, the luminosity of the star is higher than the corresponding main-sequence stars by a factor of 1.2–1.3, as is characteristic of the best studied young precataclysmic variables [18, 31, 32]. This excess luminosity of the secondary is explained by residual excitation after the common-envelope phase. Since V664 Cas is clearly a young precataclysmic variable, the presence of an excited secondary in the system is quite probable. Therefore, we do not believe there is a good basis to lower the rotational velocity of the secondary, which would lead to an increase in its mass. At the same time, a substantial increase in $V \sin i$ (by more than 8.0 km/s) is likewise unacceptable. For example, with our resulting set of parameters for V664 Cas, the radius of the G star is close to the radius of the Roche lobe ($R_2 = 1.39R_\odot$), which admits the possibility of weak accretion onto the blue subdwarf via the stellar wind. When the mass of the secondary is decreased to $M_2 = 1.0M_\odot$, it should overfill its Roche lobe and the system should become a cataclysmic variable. However, none of the observational characteristics of V664 Cas indicate the presence of mass transfer in the system, convincing us of the correctness of our derived value for M_2.

5. FORMATION OF THE SPECTRUM OF V664 Cas

We used the parameters we obtained to compute a blanketed mean spectrum for V664 Cas for phases near maximum brightness, $\Delta\varphi = 0.25$–0.75. Figure 6 shows this spectrum and the observed spectrum for these phases. This comparison enables us to draw a number of conclusions about the conditions under which the lines are formed and the accuracy of our method for modeling them.

1. There is good agreement between the theoretical and observed profiles of many weak lines of heavy elements in the second ionization state, and also for most HeI lines. We therefore conclude that the material in the layers in which these lines are formed, $-1.0 < \log \tau_r < 0.0$, is close to a thermalized state. The stronger HeI $\lambda\lambda$4026, 4471 Å line is formed partially in the hot Lyman chromosphere with $-2.0 < \log \tau_r < -0.7$. As was shown in [33], the appearance

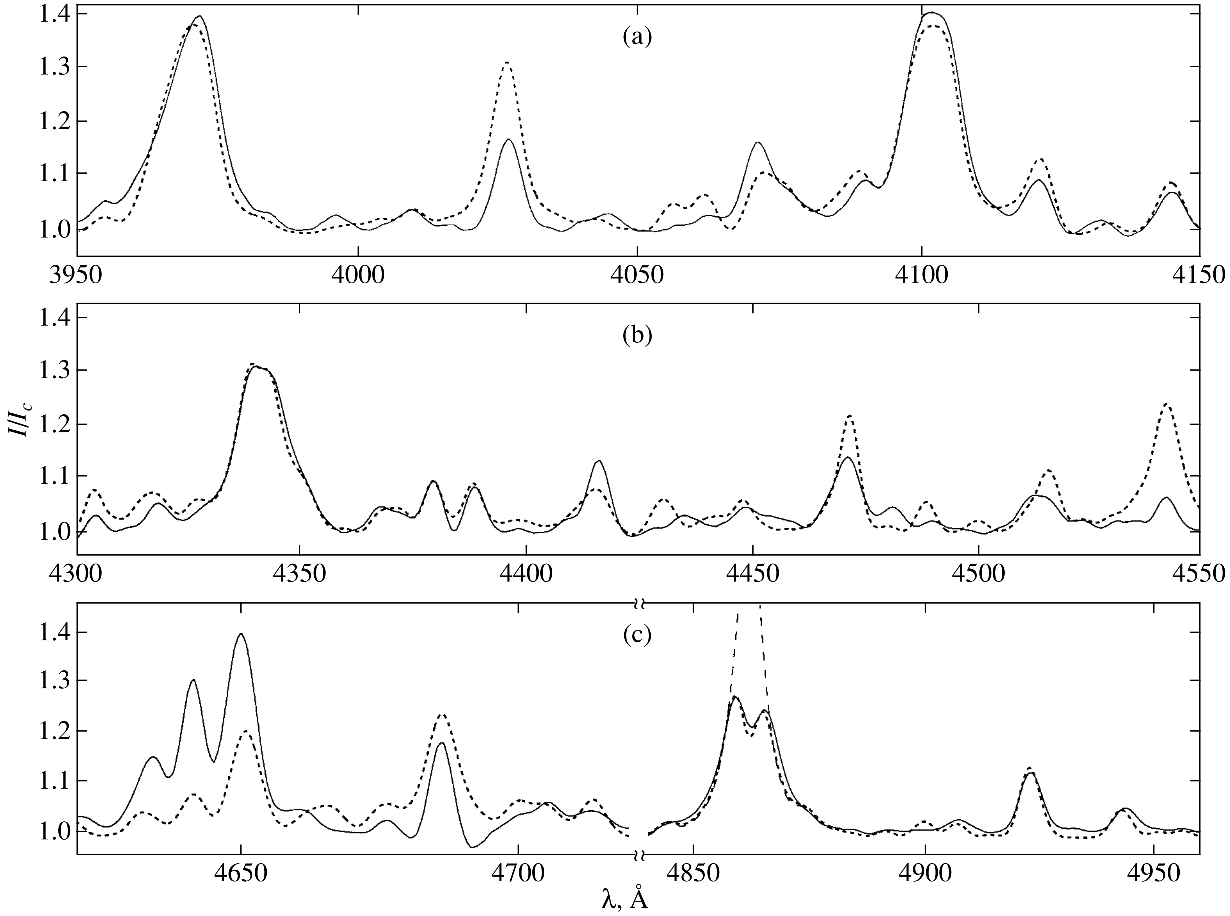

Fig. 6. Observed (solid curve) and theoretical (short-dashed curve) mean spectra of V664 Cas at phases $\Delta\varphi = 0.25$–0.75. The long-dashed curve in the lower panel shows the profile of the Hβ line without allowance for absorption in the nebula (see text).

of a "superrecombination" state is characteristic of weakly ionized elements in a Lyman chromosphere, leading to a weakening of emission lines, as is observed for the HeI $\lambda\lambda$4026, 4471 Å line.

2. The observed intensities of the strong OII λ4071 Å NII λ4630 Å, and especially the NIII λ4640 Å CIII λ4649 Å lines appreciably exceed the theoretical values. The region of formation of all these lines lies only in layers of the Lyman chromosphere with $-4.0 < \log\tau_r < -1.0$, for which a thermalization approximation would clearly be erroneous. The excess intensity of the lines of highly ionized elements indicates their "superionization" by hard ultraviolet radiation, which can be modeled only in a non-LTE approach.

3. We were not able to obtain a satisfactory agreement between the observed and theoretical HeII line profiles. As we can see from Fig. 6, the observed HeII $\lambda\lambda$4200, 4541 Å line is appreciably weaker than the model value, while the discrepancy for the HeII λ4686 Å line is smaller. At the same time, it is not possible to reproduce the observed absorption wings of the HeII λ4686 Å line, since the contribution of the blue subdwarf to the total flux of the system does not exceed 15% at these wavelengths. These problems can be partially eliminated if the helium abundance in the primary atmosphere is enhanced by a factor of 2–3; this could be verified by observations of the HeII λ1640 Å line in the ultraviolet.

The question of the formation of the Balmer lines requires a special study, since the two-peaked shape of their profiles cannot be reproduced using our modeling method. Similar two-peaked profiles were detected by Exter *et al.* [21, 7] in their analysis of spectra of VW Pyx [21] and TW Crv [7], but they are absent from the spectra of all classical precataclysmic variables: BE UMa, NN Ser, etc. There cannot be an optically thin accretion disk in the V664 Cas system, since this would lead to enhancement of the

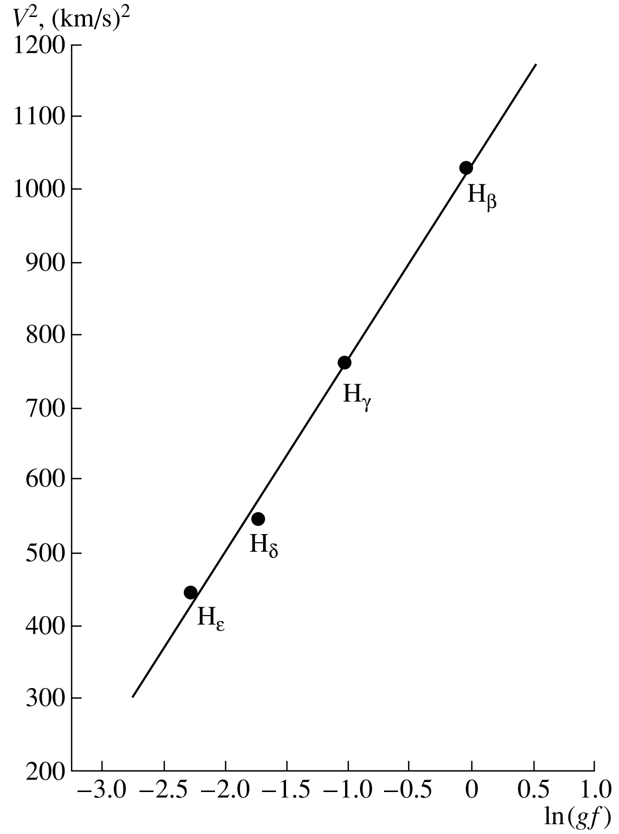

Fig. 7. Dependence of the velocity dispersion $\sigma(V_i)$ of the absorbing atoms in the planetary nebula derived from the Balmer lines on the oscillator strengths of these lines.

emission lines at minimum brightness, in contradiction with the observational data. Our theoretical computations varying the rotational velocity of the secondary demonstrated the impossibility of the two-peaked lines being formed in the spectrum of the irradiated star. The resulting profiles obtained using the adopted parameters for V664 Cas (shown in Fig. 6 only for Hβ) correspond well with the observed profiles in the wings but have core intensities that are a factor of 2–3 too high. Deviations from LTE for the hydrogen atoms may provide an explanation for the weakening of the cores of the Balmer lines, since these lines form partially in the Lyman chromosphere. However, the similarity of the conditions in the irradiated atmospheres of the secondaries in V664 Cas, VW Pyx, and BE UMa in the presence of qualitatively different observed profiles demands that we seek a different explanation. We believe that this is the presence in V664 Cas and VW Pyx of the bright planetary nebulae HFG1 and K1-2, while BE UMa has only a weak, rarified envelope. Indirect evidence for the influence of the nebula on the formation of the central dip in the H line profiles is provided by the stability of its wavelength as the orbital phase changes; i.e., the dip is not associated with the orbital motion of the components. We accordingly modeled the Balmer lines assuming that the radiation within $d\lambda$ of their centers is absorbed in the planetary nebula in its path toward the observer and is replaced by the radiation of the nebula. Subsequent reradiation of the absorbed photons by the nebula occurs in all directions, so that only a small fraction of these reach the observer. We computed the corresponding intensity in the nebula lines in accordance with the data of [34], taking into account the area of the visible disk of the star of three square degrees. This mechanism for the removal of photons from the H lines could be efficient if the optical depth of the nebula is high in the line cores. Unfortunately, there are no estimates of the density of free electrons in the HFG1 nebula. Using the mean value for planetary nebulae, $n_e = 5 \times 10^3$ cm^{-3}, and the radius of HFG1 $R = 0.7$–0.8 pc [34], we find the optical depth in the core of the Hβ line to be $\tau \approx 40$.

We can see from Fig. 6 that our computed Balmer-line profiles are in excellent agreement with the observed profiles. Note especially the enhancement of the blue peak compared to the red peak, in agreement with our observations of V664 Cas, as well as the observations of [21] for VW Pyx. The values of $d\lambda$ were selected individually for each line and were found to be $d\lambda = 0.52$, 0.40, 0.32, and 0.28 Å for the sequence Hβ—Hϵ. The corresponding estimates of the velocity dispersion for the absorbing atoms ($\sigma(V_i) =$ 21–32 km/s) can be represented as

$$\sigma(V_i) = k_i \overline{\Delta V},$$

where $\overline{\Delta V}$ is their mean square velocity in the nebula and the parameter k_i depends on the line opacity coefficients. If the Doppler broadening due to the thermal motion of the atoms dominates in the formation of the absorption profiles, the quantity

$$gf_i \exp\left(-\frac{(\sigma(V_i))^2}{(\overline{\Delta V})^2}\right)$$

should be constant for all the Balmer lines. The dependence of our values of $\sigma(V_i)$ on the line oscillator strengths [17], presented in Fig. 7, fully confirms that this is the case. The approximate relation $\ln gf$ versus $(\sigma(V_i))^2$ is a linear function; we estimated the rms speed of the hydrogen atoms in the absorbing region to be $\overline{\Delta V} = 16.3 \pm 0.4$ km/s, which corresponds to a temperature of $T = 31\,500 \pm 1500$ K.

6. CONCLUSIONS

V664 Cas is the seventh object classified as a young precataclysmic variable containing an sdO subdwarf and surrounded by a planetary nebula. Some of the observed characteristics of its radiation (high-amplitude brightness variations, the presence of emission lines of highly ionized elements, and the domination of the flux in the blue part of the spectrum) are typical of all the members of this group. However, V664 Cas displays a number of features that make it unique among known close binary systems that have passed through a common-envelope stage.

(1) The mass function of the primary—$f(m) \approx 0.007 M_\odot$, as determined in models with both circular and elliptical orbits—is the smallest of all such values for precataclysmic variables. It is noteworthy that the elliptical-orbit model with eccentricity $e = 0.09$ describes the radial-velocity curve appreciably better. The low value of $f(m)$ shows that the secondary in the V664 Cas system has a large mass; this is the only such case among precataclysmic variables with orbital periods less than a day.

(2) The amplitude of the V664 Cas brightness variations remains nearly the same in the visible, infrared, and near-ultraviolet. Consequently, a hot spot on the surface of the secondary dominates the radiation of the system at all orbital phases. A quantitative analysis of the spectra and light curves of V664 Cas indicates that the temperature of the atmosphere at the center of the hot spot is $T_{eff} \approx 23\,000$ K if the temperature of the secondary is $T_{eff} = 5400$ K.

(3) Broad (corresponding to $\Delta V_l = 900$ km/s), two-peaked Balmer profiles are observed in the spectra of V664 Cas, which are not characteristic of the spectra of close binaries without accretion. The two-peaked shape of the profiles is due to absorption of the radiation of V664 Cas by material in the planetary nebula. The hydrogen atoms in the absorbing region have an rms velocity of $\overline{\Delta V} = 16$ km/s and do not have a significant vector velocity relative to the center of the star. The detection of two-peaked H profiles in the spectra of VW Pyx and TW Crv as well suggests that such profiles are characteristic of young precataclysmic variables with sdO subdwarfs. An accurate test of this hypothesis will be carried out via studies of two promising young precataclysmic variable candidates: the cores of the planetary nebulae Abell 65 and SP1.

(4) A detailed analysis of poorly studied cataclysmic binaries whose evolutionary status has been established based on observations of low-resolution spectra may provide an additional means to increase the list of precataclysmic variables. Some of these objects are cores of planetary nebulas and contain narrow lines of neutral and ionized helium, CNO-group elements in high ionization states, and hydrogen with two-peaked profiles in their spectra. Overall, these objects appear very similar to V664 Cas and VW Pyx, which, in the light of the results we have presented here, reopens the question of their classification.

ACKNOWLEDGMENTS

The authors are sincerely grateful to the Committee for Studies using Large Telescopes for their many years of support of our program of studies of the spectra of close binary systems. We also are thankful to V.F. Suleĭmanov for valuable advice and productive discussions of our results, A. Pramskiĭ and A.N. Burenkov for their assistance during the observations on the 6-m telescope, and N.N. Samus' and S.Yu. Shugarov for presenting us with their photometric data. This work was supported by grants 99-02-17488 and 02-02-17174 and by the State Science and Technology Program in Astronomy. V.V. Shimanskiĭ separately thanks the Russian Foundation for Basic Research for two IAU grants (project nos. 02-02-06591 and 01-02-06065).

REFERENCES

1. H. Ritter, Astron. Astrophys. **169**, 139 (1986).
2. I. J. Iben and A. Tutukov, Astrophys. J. **418**, 343 (1993).
3. L. Morales-Rueda, P. F. L. Maxted, T. R. Marsh, *et al.*, Mon. Not. R. Astron. Soc. **338**, 752 (2003).
4. A. Chen, D. O'Donoghue, R. S. Stobie, *et al.*, Mon. Not. R. Astron. Soc. **275**, 100 (1995).
5. D. K. Sing, J. B. Holberg, M. A. Barstow, *et al.*, in *White Dwarfs*, NATO Sci. Ser. II **105**, 349 (2003).
6. M. De Kool and H. Ritter, Astron. Astrophys. **267**, 397 (1993).
7. K. M. Exter, D. L. Pollacco, D. L. Maxted, *et al.*, in *White Dwarfs*, NATO Sci. Ser. II **105**, 287 (2003).
8. J. H. Heckathorn and R. A. Fesen, Astron. Astrophys. **143**, 475 (1985).
9. A. D. Grauer, H. E. Bond, R. Giardullo, and T. A. Fleming, *AAS Meting No. 169*, *Pasadena, 1987*, p. 643.
10. A. Acker and B. Stenholm, Astron. Astrophys. **233**, L21 (1990).
11. H. Ritter and U. Kolb, Astron. Astrophys. **404**, 301 (2003).
12. N. A. Ketsaris, S. V. Antipin, and S. Yu. Shugarov, in *Cataclysmic Variables*, Astrophys. Space Sci. Lib. **205**, 163 (1995).
13. A. Pigulski and G. Michalska, IBVS No. 5218, 1 (2002).
14. V. L. Afanas'ev, A. N. Burenkov, V. V. Vlasyuk, and S. V. Drabek, Preprint No. 234.128, SAO RAN (Spets. Astrofiz. Obs., Nizhnii Arkhyz, 1995).
15. R. C. Bohlin, Astron. J. **111**, 1743 (1996).
16. P. Ballester, ESO/ST-ECF Data Analysis Workshop No. 177 (1992).
17. R. L. Kurucz, SAO CD-ROMs (Cambridge, MA02138, USA, 1994).
18. D. H. Ferguson, S. Haas, R. Napiwotzki, *et al.*, Astron. J. **114**, 1227 (1997).
19. D. H. Ferguson and T. A. James, Astrophys. J., Suppl. Ser. **94**, 723 (1994).

20. V. V. Shimanskiĭ, Astron. Zh. **79**, 145 (2002) [Astron. Rep. **46**, 127 (2002)].
21. K. M. Exter, D. L. Pollacco, and S. A. Bell, Mon. Not. R. Astron. Soc. **348**, 1349 (2003).
22. D. H. Ferguson, J. Liebert, S. Haas, *et al.*, Astrophys. J. **518**, 866 (1999).
23. E. Marilli, A. Frasca, M. Bellina Terra, and S. Katalano, Astron. Astrophys. **295**, 393 (1995).
24. M. S. O'Brien, H. E. Bond, and E. M. Siom, Astrophys. J. **563**, 971 (2001).
25. N. A. Sakhibullin and V. V. Shimanskiĭ, Astron. Zh. **74**, 432 (1997) [Astron. Rep. **41**, 378 (1997)].
26. D. V. Ivanova, N. A. Sakhibullin, and V. V. Shimanskiĭ, Astron. Zh. **79**, 433 (2002) [Astron. Rep. **46**, 390 (2002)].
27. V. V. Shimanskiĭ, N. V. Borisov, and N. N. Shimanskaya, Astron. Zh. **80**, 712 (2003) [Astron. Rep. **47**, 763 (2003)].
28. S. E. Nersisyan, A. V. Shavrina, and A. A. Yaremchuk, Astrofizika **30**, 247 (1989).
29. V. L. Straĭzhis, *Multicolor Stellar Photometry* (Mokslas, Vilnius, 1977) [in Russian].
30. N. A. Sakhibullin and V. V. Shimanskiĭ, Astron. Zh. **73**, 793 (1996) [Astron. Rep. **40**, 723 (1996)].
31. D. L. Pollacco and S. A. Bell, Mon. Not. R. Astron. Soc. **262**, 377 (1993).
32. D. L. Pollacco and S. A. Bell, Mon. Not. R. Astron. Soc. **267**, 452 (1994).
33. D. V. Ivanova, N. A. Sakhibullin, and V. V. Shimanskiĭ, Astron. Zh. (in press).
34. J. H. Heckathorn, R. A. Fesen, and T. R. Gull, Astron. Astrophys. **114**, 414 (1982).

Translated by D. Gabuzda

Astronomy Reports, Vol. 48, No. 7, 2004, pp. 577–587. Translated from Astronomicheskiĭ Zhurnal, Vol. 81, No. 7, 2004, pp. 635–647.

Atmospheric Chemical Composition of the Halo Star HD 221170 from a Synthetic-Spectrum Analysis

V. F. Gopka[1], **A. V. Yushchenko**[1,2], **T. V. Mishenina**[1],
Chulhee Kim[3], **F. A. Musaev**[4,5], and **A. V. Bondar'**[5]

[1]*Odessa Astronomical Observatory, Mechnikov Odessa National University, Park Shevchenko, Odessa 65014, Ukraine*
[2]*Chungbuk National University, Chungju 361-763, Korea*
[3]*Chonbuk National University, Chonju 561-756, Korea*
[4]*Special Astrophysical Observatory, Russian Academy of Sciences, Nizhniĭ Arkhyz, Karachaĭ-Cherkesian Republic 369167, Russia*
[5]*International Center for Astronomical and Medical-Biological Research of National Academy of Sciences of Ukraine and Russian Academy of Sciences, Golosiiv, Kiev 03680, Ukraine*

Received May 20, 2003; in final form, January 9, 2004

Abstract—The atmospheric abundances of 30 chemical elements in the halo star HD 221170 are analyzed by fitting synthetic spectra to observed spectra (i) with a resolution of 60 000 and signal-to-noise ratios of about 200 taken with the 1.93-m telescope of the Observatoire de Haute Provence and (ii) with a resolution of 35 000 and signal-to-noise ratios of more than 100 taken with the 2-m telescope of the Terskol Peak Observatory. The derived parameters of the stellar atmosphere are $T_{eff} = 4475$ K, $\log g = 1.0$, [Fe/H] $= -2.03$, $V_{micro} = 1.7$ km/s, and $V_{macro} = 4$ km/s. The parameters T_{eff}, $\log g$, [Fe/H], and V_{micro} can be determined by analyzing the variations of the rms error of the mean iron abundance derived using different model atmospheres. The chemical composition of the star's atmosphere is analyzed. The abundances of a total of 35 elements in HD 221170 have been derived in this paper and in previous studies. Overall, the abundances of elements lighter than praseodymium are consistent with the elemental abundances in the atmospheres of stars with similar metal deficits. Copper and manganese are underabundant by -2.9 and -2.6 dex, respectively, relative to the Sun (when the analysis includes the effects of hyperfine structure). Heavy r-process elements (starting from praseodymium) are overabundant compared to iron-group elements. This can be explained by an enrichment in r-process elements of the material from which the star was formed. © *2004 MAIK "Nauka/Interperiodica"*.

1. INTRODUCTION

According to the modern theory of stellar evolution, stars of the halo—the spherical component of the Galaxy—with masses higher than a solar mass have already completed their evolution and, having undergone various stages of rapid evolution, can now be observed as neutron stars, white dwarfs, or other relativistic objects. Old low-mass stars (with masses lower than a solar mass) are still evolving. These stars have been preserved to the present precisely due to the low rate of their evolution. These are low-luminosity stars with low metal abundances and probable ages of the order of ten billion billion years or more. The chemical compositions of such objects provide data about the matter from which the stars were formed, which can help us determine whether the interstellar medium was homogeneous at sites of star formation in different parts of the Galaxy and estimate stellar ages using the abundances of long-lived elements. This is possible for a small class of halo stars that are overabundant in r-process elements. Detailed atmospheric-abundance curves for such stars can help us understand how the enrichment in heavy elements proceeded in the Milky Way and via what processes.

The chemical compositions of all generations of stars in the Milky Way carry important information about the history of nucleosynthesis in our Galaxy. The observed elemental abundances are the sum of the products of nuclear reactions in stars of various masses, at various stages of evolution, and with various initial chemical compositions. Most spectroscopic analyses of stellar chemical composition have focused on stars of the Galactic disk. Deciphering such analyses for these stars is a complex and ill-posed inverse problem due to the need to take into account a large number of factors, such as the mass functions of various generations of stars, the production functions for various elements, the fraction of matter enriched in elements heavier than hydrogen during the evolution of stars of various masses and its subsequent ejection into the interstellar medium, binarity, magnetic fields, etc. Old (halo) stars occupy a special position in this respect and may prove to be key to our understanding of the chemical evolution of the Milky Way, since these stars have resulted from a smaller number of life cycles of stars of various masses. Their spectra are easier to interpret, since the smaller number of previous star-formation cycles involved makes it possible to investigate the origin of observed anomalies in elemental abundances with less uncertainty.

Population-II stars may be the products of the nucleosynthesis in as yet undiscovered metal-poor, massive Population-III stars. The chemical compositions of Population-II stars could be reproduced by one or several stellar generations. We cannot develop a well-founded theory for the chemical evolution of the Milky Way, other galaxies, and the Universe as a whole without accumulating abundance data for the largest possible number of elements in various types of stars.

The halo star HD 221170 is underabundant in iron by slightly more than 2 dex and is a giant ascending the giant branch for its first time [1]. Characteristic of old stars of our Galaxy, it has a large heliocentric space velocity; its radial velocity is -121.696 ± 0.027 km/s [2], and the components of its Galactic velocity are $u = -152$, $v = -133$, and $w = 59$ km/s.

The heliocentric distance of HD 221170 (HIP 115949) has been estimated to be 435 pc (according to the HIPPARCOS parallax of $0.00230'' \pm 0.00084''$), 689 pc [3], and 770 pc [4].

The absolute magnitude of the star has been estmated to be $M_v = -2.4$ [1], -1.9 [4], and -1.67 [5]. The apparent magnitude and UBV color indices are $V = 7.70$, $B{-}V = 1.70$, and $U{-}B = 0.62$ [6]. The star is located in Pegasus, making it convenient to observe from the Northern hemisphere, and it has been the subject of numerous studies.

Gilroy *et al.* [7] and others have pointed out that one possible type of abundance curve for metal-poor stars should display an overabundance of lanthanides compared to the abundance for a solar abundance curve that has been shifted along the horizontal axis to make the iron abundance match that of the star considered.

At present, considerable attention is being paid to studies of stars with appreciable metal deficiencies, including stars that are overabundant in r-process elements. Abundance-curve data are being accumulated for various stars with various degrees of heavy-element enrichment.

In their model-atmosphere analysis of several bright halo stars, Gopka *et al.* [8] found one of them, HD 221170, to be overabundant in europium, dysprosium, and erbium (relative to iron). Later, Yushchenko *et al.* [9] confirmed the overabundances in the vicinity of the second and third peaks of neutron-capture elements using new observations and synthetic spectra and identified several more r-process elements that were overabundant.

To refine these results, we analyzed the atmospheric abundances of the halo star HD 221170 by fitting synthetic spectrum using new atomic and molecular data. We focus on the blue part of the spectrum, which is of the greatest interest from the viewpoint of the abundances of neutron-capture elements.

2. SPECTROSCOPIC DATA

We analyze two spectra here. The first is from the library of the Observatoire de Haute Provence [10]. The spectrum was taken with the ELODIE echelle spectroscope mounted on the 1.93-m telescope of this observatory. The standard spectral resolution of the spectroscope is 42 000, but we took the spectral resolution to be 60 000 based on our analysis of these particular data; we found this resolution to yield the best fit between the iron lines in the observed and theoretical spectra when we used the iron abundance derived using the model atmospheres. The spectrum spans the wavelength range from 4500 to 6800 Å and has a signal-to-noise ratio of about 200. The preliminary reduction of the spectrum (image extraction, cosmic-ray removal, etc.) was performed by Katz *et al.* [11], and the subsequent processing (continuum-level tracing, wavelength calibration, etc.), by Mishenina and Kovtyukh [12].

The second spectrum was taken with the 2.0-m Zeiss telescope of the Terskol Peak Observatory in June 2002. This spectrum spans the wavelength range from 3812 to 7752 Å and has a signal-to-noise ratio of more than 100. The standard spectroscopic resolution of the camera employed is 45 000, but the actual resolution of this particular spectrum was 35 000. A description of the spectrograph can be found in [13]. We used the DECH [14] software for the preliminary reduction (image extraction, cosmic-ray removal, etc.) and the URAN [15] software for the remaining reduction. Figures 1 and 2 show examples of the spectra taken at the Observatoire de Haute Provence and the Terskol Peak Observatory.

```
_No__%___R__Wave__Id
 13_799_988 19.831 CrI
 14_998_739 19.979 NiI
 15_746_986 20.072 GdII =
 16_996_274 20.224 FeII
 17_670_989 20.442 CeII =
 18_640_999 20.766 SiH
 19_920_990 20.914 SiH
 20_901_990 21.114 SiH
 21_779_994 21.190 SiH
 22_566_976 21.293 GdII =
 23_718_975 21.322 NiI
 24_795_999 21.492 SiH
 25_985_994 21.641 FeI
 26_504_990 21.815 SiH
 27_739_991 21.951 GdII =
 28_792_991 22.008 CrI
 29_961_981 22.078 CeII =
 30_883_667 22.370 LaII =
 31_558_898 22.512 EuII =
 32_994_264 22.634 FeII
 33_995_288 22.796 TiI
 34_957_646 23.075 CeII =
 35_503_999 23.257 SiH
 36_976_886 23.401 FeI
 37 1000_953 23.566 NdII =
 38_976_991 23.694 NiI
 39_620_995 23.790 SiH
 40_853_863 23.909 SmII =
 41_516_999 24.122 NbI =
 42_974_984 24.206 VI
 43_598_999 24.331 MoI =
 44_643_999 24.400 CeII =
 45_521_999 24.493 FeII
 46_821_987 24.585 CeII =
 47 1000_707 24.687 TiII
 48_727_972 24.837 ThII =
 49_970_942 24.925 BaII =
 50 1000_246 25.141 FeI
 51_868_828 25.242 TiII
 52_703_997 25.673 SiH
```

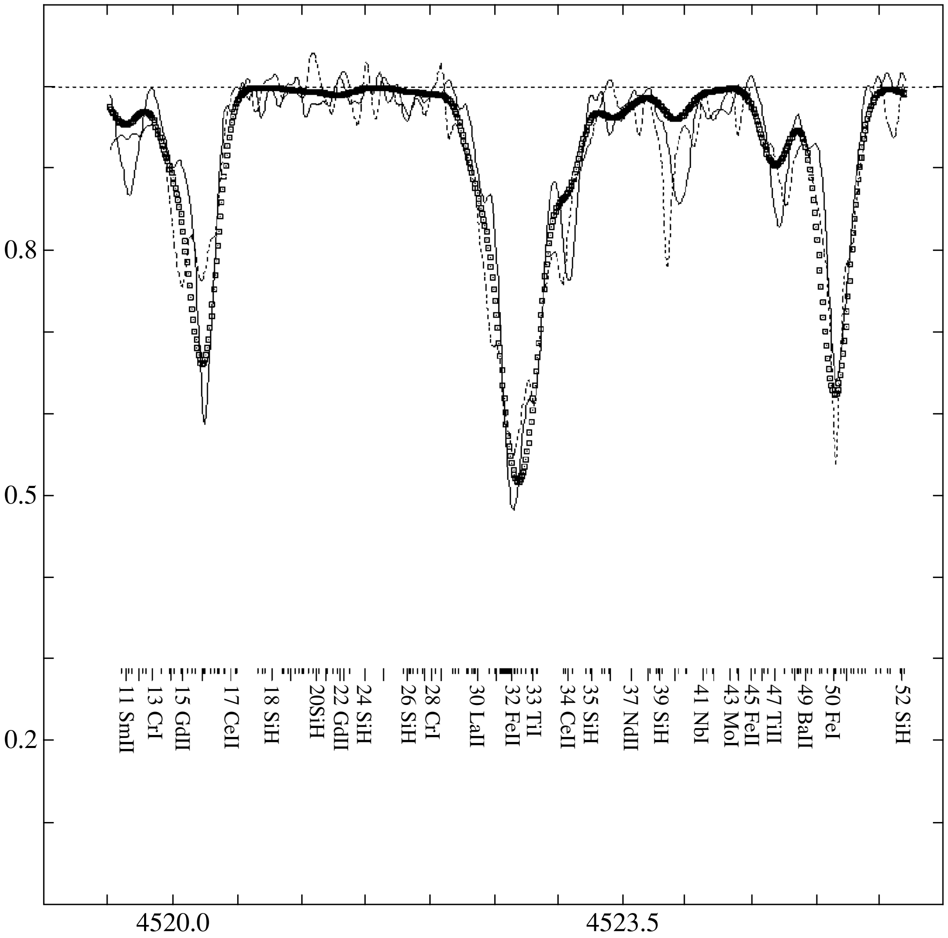

Fig. 1. Observed spectra of HD 221170 and the synthetic-spectrum approximations. The solid and dashed curves show the observations made at the Observatoire de Haute Provence and Terskol Peak Observatory, respectively. The squares show the synthetic spectrum. The synthetic spectrum is convolved with the instrumental profile of the ELODIE spectrograph of the Observatoire de Haute Provence and the microturbulence velocity. The left part of the figure gives data on the strongest lines used in the synthetic-spectrum computations in tabular form. The positions and identifications of these lines are shown in the lower part of the figure. Short dashes indicate weak lines. The table gives the following parameters for strong lines: (1) number of the line in the figure, (2) ten times the percent contribution of the line to the total line absorption coefficient at the central wavelength (equal to 1000 for unblended lines), (3) the level of the synthetic spectrum at the central wavelength computed without convolving with the microturbulence and instrumental profiles, with the continuum scaled to 1000, (4) the last digits of the wavelength, and (5) the identification of the line. The lines of elements with atomic numbers greater than 28 are indicated by "=." This figure and Fig. 2 are screens from the URAN package [15].

3. ATMOSPHERIC PARAMETERS OF HD 221170

The halo star HD 221170 has been regularly studied as new telescopes, methods, and atomic data have become available. Table 1 gives the effective temperatures, logarithmic surface gravities, microturbulence velocities, and iron abundances relative to the Sun derived by us and taken from [1, 4, 6, 7, 12, 16–30].

There is considerable scatter among the various parameter estimates. The effective temperatures differ by almost 350 K, with most of the values being close to 4500 K. The logarithmic surface gravity ranges from 0.0 to 1.5, with most of the $\log g$ estimates being close to 1.0. The estimated microturbulence velocities differ by nearly a factor of two.

We first used the atmospheric parameters of HD 221170 derived by Mishenina and Kovtyukh [12]: $T_{eff} = 4500$ K, $\log g = 1.0$, and $V_{micro} = 1.5$ km/s. We tested the choice of T_{eff} and V_{micro} by analyzing the dependence of the iron abundances derived from individual lines on the energy of the lower level and the equivalent widths of the corresponding lines. We used lines of neutral iron and the solar oscillator strengths of Gutovenko and Kostyk [31]. We were able to select only 90 lines due to the substantial differences in the temperature and metallicity of the Sun and HD 221170. The correlation coefficient for

```
_No__%___R__Wave__Id
 11_997_278 16.615 FeII
 12 1000_580 16.784 FeII
 13_502 1000 17.294 CH
 14 1000_907 17.524 FeI
 15_524 1000 17.734 CH
 16 1000 1000 17.865 MgH
 17 1000_991 18.033 FeI
 18_922_996 18.127 CeII =
 19_998_874 18.349 ScII
 20_866_998 18.598 NbI =
 21_973_988 18.810 CrI
 22_742 1000 19.061 MgH
 23_991_984 19.206 FeI
 24_988_999 19.319 CrI
 25_943_995 19.624 FeI
 26 1000_416 19.815 NdII#
 27 1000_963 20.039 FeI
 28_503 1000 20.205 MgH
 29_504 1000 20. 308 MgH
 30_605_998 20.442 NiI
 31_870_998 20.576 TiI
 32 1000_953 20.782 YII =
 33_842_927 21.069 PrII =
 34_771_937 21.109 FeI
 35_837 1000 21.250 ZrI =
 36_531 1000 21.374 MgH
 37_835_999 21.606 UII =
 38_995_999 21.712 CoI
 39_998_978 21.817 PrII =
 40 1000_605 22.041 FeI
 41 1000_999 22.476 CeII =
 42 1000_758 22.772 PrII =
 43_654 1000 22.983 TmII =
 44_572_999 23.052 ScI
 45_885_997 23.276 KI
 46_998_972 23.510 FeI
```

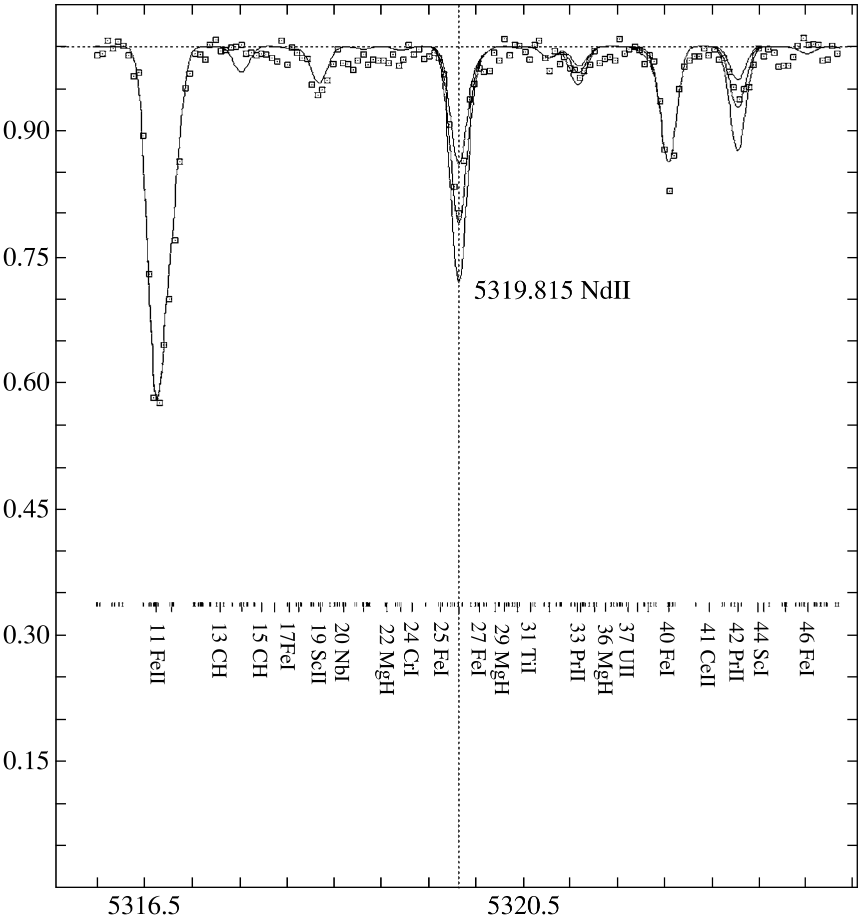

Fig. 2. Observed spectrum of HD 221170 and the synthetic-spectrum approximation in the vicinity of the NdII line at λ 5319.815 Å. The open and filled squares show observations made at the Observatoire de Haute Provence and the synthetic spectra, respectively. Three synthetic spectra are shown in the vicinity of the neodymium line, computed with our derived mean neodymium abundance and with abundances ±0.3 dex higher and lower than this mean. The line under study is indicated by a vertical dashed line in the plot and a "#" symbol in the tabular part of the figure. The left side of the plot shows two praseodymium lines with similarly computed synthetic spectra.

each dependence was close to zero, indicating that the adopted parameters are fairly close to the real parameters of the star.

We refined the model parameters using the method applied by Yushchenko *et al.* [32]. The iron abundances based on individual lines are calculated using a grid of model-atmosphere parameters that are fairly close to the real values, and the results are then used as a basis to select the optimal model atmosphere.

Two dependences are commonly used: the dependence of the iron abundance on (1) the equivalent widths of the lines used or $\log(W_\lambda/\lambda)$ (hereafter $N-W$) or (2) the energy of the lower levels of the corresponding lines (hereafter $N-E$). The initial T_{eff} and $\log g$ are set equal to values based on photometric or other data. The microturbulence velocity is then selected to make the correlation coefficient for the first dependence equal to zero. In the next step, the second dependence is used to test the correctness of the choice of temperature. The process is repeated if the correlation coefficients differ significantly from zero. In recent years, researchers have increasingly estimated the parameters of stellar atmospheres using various model-atmosphere grids, as was done, e.g., by Boyarchuk *et al.* [33].

Yushchenko *et al.* [32] pointed out that the rms error of the mean iron abundance (hereafter sN) computed using a number of different model atmospheres is smallest near values for the atmospheric parameters that are correct according to other estimations of these parameters. We thus have at our disposal an independent variable that enables us to decrease the degree of ill-posedness in our estimation of the atmospheric parameters.

We selected the model-atmosphere parameters on a three-parameter grid. The first two parameters were the effective temperature and surface gravity. We interpolated the model atmospheres of Kurucz [34]

Table 1. Atmospheric parameters of HD 221170 determined by various authors

Authors	Reference	T_{eff}	$\log g$	V_{micro}	[Fe/H]
Wallerstein *et al.*, 1963	[6]				−2.60
Bond, 1980	[4]				−2.60
Leep and Wallerstein, 1981	[16]	4350	0.0	1.50	−2.20
Luck and Bond, 1981	[1]	4500	0.8	3.0	−2.59
Kraft *et al.*, 1982	[17]	4525			−2.20
Gratton and Ortolani, 1984	[18]	4500	1.1		−1.80
Gratton and Sneden, 1987	[19]	4500	1.3	1.4	−1.96
Gilroy *et al.*, 1988	[7]	4625	1.4	2.80	−2.20
Kraft *et al.*, 1992	[20]	4550	1.3	2.00	−2.10
Pilachowski *et al.*, 1993	[21]	4625		2.00	−1.96
Gratton, 1996	[22]	4444	0.92		−2.12
Pilachowski *et al.*, 1996	[23]	4425	1.0	1.5	−2.15
Shetrone *et al.*, 1996	[24]	4550	1.3	2.0	−2.10
Gratton *et al.*, 2000	[25]	4500	0.9	2.7	−2.19
Burris *et al.*, 2000	[26]	4425	1.0	1.5	−2.15
Fulbright *et al.*, 2000	[27]	4500	0.9	2.7	−2.19
Mishenina and Kovtyukh, 2001	[12]	4500	1.0	1.5	−2.05
Snider *et al.*, 2001	[28]	4610	1.57		−2.12
		4686	1.54		−2.11
Melendez *et al.*, 2001	[29]	4460	0.75	1.6	−2.11
		4410	1.49	1.6	−1.79
Melendez and Barbuy, 2002	[30]	4410	1.1		−2.00
This paper		4475	1.0	1.7	−2.03

with [Fe/H] = −2.0 dex in temperature from 4250 to 4750 K in steps of 25 K and in surface gravity from 0.0 to 1.5 in steps of 0.1. The third parameter was the microturbulence velocity. For each model, we calculated the iron abundances with various microturbulence velocities in the interval from 0.1 to 7 km/s with a variable step using the Width9 program of Kurucz [35].

We determined the equivalent widths of 187 lines of neutral iron and 23 lines of ionized iron and then found the two microturbulence velocities that made the correlation coefficients of the $N{-}W$ and $N{-}E$ dependences equal to zero, as well as the microturbulence velocity that minimized the quantity sN for iron. We supposed that these three microturbulence velocities should coincide if T_{eff} and $\log g$ are chosen correctly. For each model atmosphere, we calculated the mean microturbulence velocity and its error.

We also calculated the difference of the mean iron abundances derived from the lines of neutral and ionized iron for all the model atmospheres and microturbulence velocities considered.

Figure 3 shows the results. The Z axis in Fig. 3a plots $1/(|\mathrm{corr}(N{-}W)| + |\mathrm{corr}(N{-}E)|)$, which is the inverse of the sum of the absolute values of the correlation coefficients for the $N{-}W$ and $N{-}E$ relations. The true parameters of the stellar atmosphere should be close to the maximum of this function, when both correlation coefficients vanish. It is clear from Fig. 3a that the solution is ambiguous—the correlation coefficients are close to zero when T_{eff} is approximately 4475 K for all surface-gravity values considered.

The Z axis in Fig. 3b plots $1/|\log N(\mathrm{FeI}) - \log N(\mathrm{FeII})|$, which is the inverse of the absolute value of the difference between the mean abundances inferred for the lines of neutral and ionized iron. It

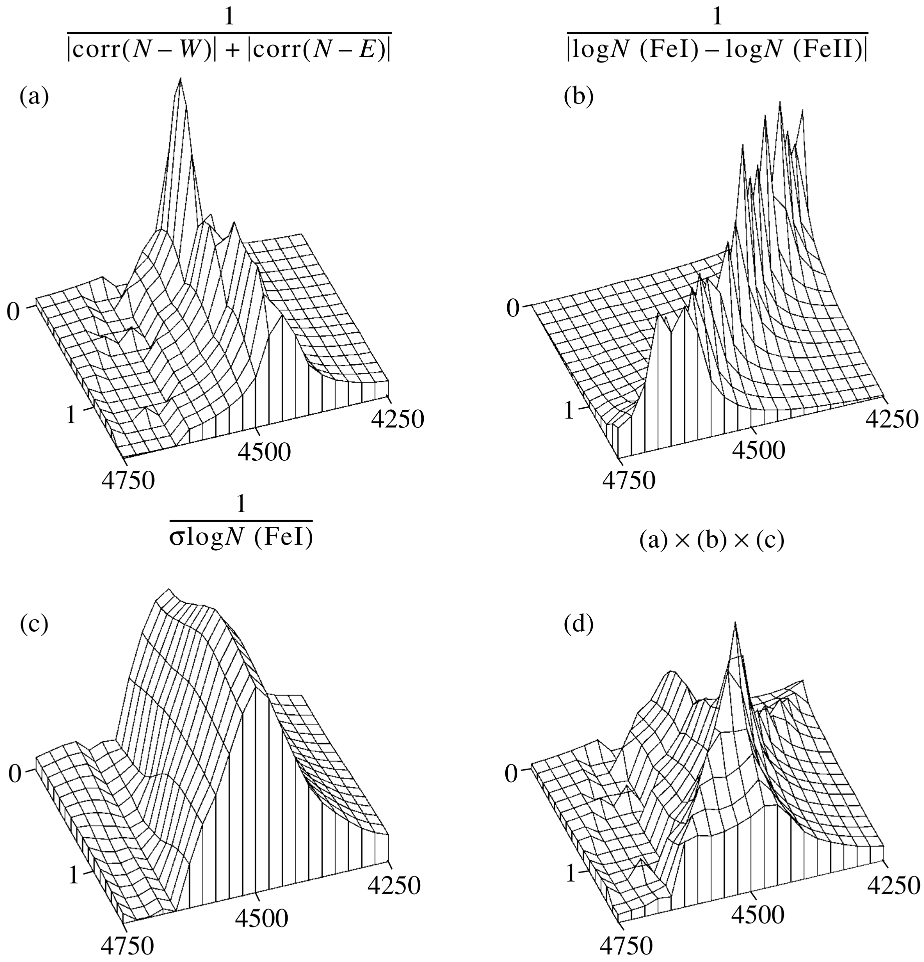

Fig. 3. Determination of the parameters of the model atmosphere of HD 221170 by calculating the iron abundance on a grid of model atmospheres. The X and Y axes give the effective temperature (in K) and the logarithmic surface gravity, while the Z axis plots the parameters described in the text. We have normalized the Z axis for better visualization of the three-dimensional plot.

is reasonable to suppose that this function should likewise reach its maximum when the effective temperature and surface gravity estimates are correct. However, the solution is also ambiguous in this case. The maximum values of this function form a ridge, which is not parallel to the ridge in Fig. 3a.

Simple multiplication of these two functions yields a surface with its maximum in the vicinity of the real parameter values. This is actually a formalization of the commonly applied iterative method for finding the parameters of a stellar atmosphere. Note that we face a number of problems when we compare the abundances of an element derived from lines of a neutral atom and the corresponding ions, including possible deviations from local thermodynamical equilibrium for atoms in the ground state or one of the ions, the quality of the model atmospheres used, and other effects. For this reason, researchers typically do not expect to achieve exact fulfillment of the condition of ionization equilibrium.

In the real case considered here, simple multiplication of the functions shown in Figs. 3a and 3b yields several local maxima with nearly equal heights due to the nonsmooth behavior of the functions near the ridge lines. The choice of the maximum that is closest to the intersection of the two ridges poses no formal problems, but its height differs little from those of the other maxima. If the directions of the ridges are not known *a priori*, the iterations can easily converge to one of the local maxima.

This may explain the usual scatter in the atmospheric parameters published for well-studied stars. Comparison of Figs. 3a and 3b with Table 1 shows that all combinations of T_{eff} and $\log g$ listed in Table 1 lie near one of the ridges. It is evident that some additional criterion is required if we wish to determine the parameters more confidently.

The Z axis in Fig. 3c gives the inverse of sN for iron as derived from the lines of neutral iron. This function is more monotonic that the previous two and reaches its only maximum at $T_{eff} = 4500$ K, $\log g = 1.1$. These values are close to the mean effective temperature and surface gravity and can be used to determine the elemental abundances. The microturbulence velocity in this case is 1.762 ± 0.016 km/s.

Thus, it is possible to determine the effective temperature, surface gravity, and microturbulence velocity by calculating sN from the lines of a single ion of the element studied. The abundance of the element considered is then obtained automatically. In the case of iron, $[\mathrm{Fe/H}] = -2.03 \pm 0.11$ at the point considered.

However, this method is not sufficiently trustworthy in the case of relatively low effective temperatures considered here. The method is not free of random and systematic errors due, e.g., to the set of spectral lines used and imperfection of the model atmospheres. We therefore adopted as our final parameters those found using Fig. 3d, which shows the simple product of the functions shown in Figs. 3a–3c. Local maxima are suppressed and only one sharp maximum remains, at the point corresponding to $T_{eff} = 4475$ K, $\log g = 1.0$, and a microturbulence velocity of 1.72 ± 0.01 m/s. The abundance of neutral iron remains unchanged within reasonable accuracy: $[\mathrm{Fe/H}] = -2.03 \pm 0.11$.

To study abundances using the synthetic-spectrum method, we must also know the values of parameters characterizing the broadening of the spectral lines used: rotation, the macroturbulence velocity, and the magnetic field. We determined the microturbulence velocity from iron lines with accurately known oscillator strengths and found it to be $V_{macro} = 4$ km/s. This macroturbulence velocity is also used to model the line broadening due to the rotation of the star ($v \sin i = 7.4$ km/s [36]) and the magnetic field.

We approximated the instrumental profile by a Gaussian with the halfwidth corresponding to a spectral resolution of 60 000 or 35 000.

4. SYNTHETIC-SPECTRUM ANALYSIS OF THE ATMOSPHERIC CHEMICAL COMPOSITION OF HD 221170

We used our earlier results [8] and those of other authors on the chemical composition of HD 221170 to calculate the synthetic spectrum of the star, interpolating and extrapolating the abundances for elements that had not been studied earlier. We used a model atmosphere with $T_{eff} = 4475$ K and $\log g = 1.0$, obtained by interpolating Kurucz's grid of models with metallicity -2.0 dex. We set the microturbulence velocity equal to $V_{micro} = 1.72$ km/s.

We adopted the atomic and molecular data from Kurucz [34], the VALD database [37], the list of spectral lines presented by Morton [38], and the DREAM database [39]. The calculations for manganese, copper, barium, and europium took into account the hyperfine and isotopic splitting of the spectral lines.

We used the SYNTHE program of Kurucz [35] to calculate the synthetic spectrum throughout the wavelength interval studied, then compared the synthetic and observed spectra to obtain lists of unblended and weakly blended lines, which we subsequently used to determine the elemental abundances in both the atmosphere of the star and in the Sun. We used the Liège atlas of solar spectra [40] as the observational data for the solar spectrum. We used the model of the solar photosphere of Grevesse and Sauval [41] and set the microturbulence and macroturbulence velocities equal to $V_{micro} = 0.8$ km/s and $V_{macro} = 1.8$ km/s. We corrected the continuum level in the Liège atlas in accordance with the results of [42, 43].

The spectrum of HD 221170 abounds in weak lines, which were fitted well by the theoretical spectrum even in the first run. The lines of iron-group elements that are weakened by two orders of magnitude, which are often represented in the spectra of solar-composition stars of the same temperature (or lines that are just slightly weakened, as in the spectrum of Arcturus, which is often used as a comparison spectrum), facilitate the cleaning of the spectrum of complex blends, which are difficult to analyze quantitatively.

We used the lines selected as a result of this identification to determine the chemical composition using the differential synthetic-spectrum method. We used the SYNTHE [35] and URAN [15] codes to calculate the synthetic spectrum in a semiautomated regime. Figure 2 presents an example of corresponding observed and synthetic spectra in the vicinity of the neodymium and praseodymium lines. The complete line lists can be found at http://yushchenko.netfirms.com.

Table 2 gives the mean atmospheric elemental abundances for HD 221170. The columns of this table give for each element a running number, its atomic number, its name, the degree of ionization, the abundance relative to that in the solar atmosphere (the last digits of the error for a single determination are given in parentheses), and the number of spectral lines used for the analysis. The results based on the spectra taken at the Observatoire de Haute Provence and Terskol Peak Observatory are shown separately.

Table 3 compares our results (marked by asterisks) with those obtained in earlier studies. We averaged the data for the two spectra with weights proportional

Table 2. Atmospheric elemental abundances in HD 221170 relative to those for the Sun based on spectra taken at the Observatoire de Haute Provence and Terskol Peak Observatory

No.	Z	Ion	Haute Provence		Terskol		No.	Z	Ion	Haute Provence		Terskol	
			$[N/N_{\mathrm{H}}]$	n	$[N/N_{\mathrm{H}}]$	n				$[N/N_{\mathrm{H}}]$	n	$[N/N_{\mathrm{H}}]$	n
1	8	OI	−1.86	1			17	30	ZnI	−1.83	1		
2	11	NaI	−2.43(00)	2	−2.22(05)	2	18	38	SrI	−2.23	1	−2.02	1
3	12	MgI	−1.69(08)	2	−1.89(05)	2			SrII			−2.15	1
4	13	AlI	<−1.73	2			19	39	YII	−2.12(10)	10	−2.22(15)	5
5	14	SiI	−1.63(08)	6	−1.60(05)	3	20	40	ZrI	−2.23	1	−2.12	1
6	20	CaI	−1.86(07)	21	−1.84(15)	10			ZrII			−2.01	1
7	21	ScII	−1.93(08)	9	−1.92(00)	2	21	42	MoI			−2.22	1
8	22	TiI	−2.00(09)	43	−1.97(07)	8	22	56	BaII	−1.86(04)	2	−2.10	1
9	22	TiII	−1.77(10)	19	−1.86(14)	9	23	57	LaII	−1.89(05)	6	−1.94(03)	3
10	23	VI	−2.20(09)	11	−2.10	1	24	58	CeII	−1.93(12)	13	−1.95(15)	14
11	24	CrI	−2.26(09)	10	−2.20(01)	2	25	59	PrII	−1.51(13)	5	−1.56(08)	3
		CrII	−2.03(12)	3	−2.12(14)	3	26	60	NdII	−1.60(08)	25	−1.62(11)	12
12	25	MnI	−2.57(08)	8	−2.81	1	27	62	SmII	−1.54(11)	6	−1.64(05)	3
13	26	FeI	−2.03(11)	187	−2.04(16)	58	28	63	EuII	−1.58	1	−1.57(09)	2
		FeII	−2.04(11)	23	−1.99(07)	5	29	64	GdII			−1.55(09)	3
14	27	CoI	−1.76(11)	8	−1.77(11)	3	30	66	DyII	−1.55	1	−1.25(11)	6
15	28	NiI	−2.07(08)	50	−2.12(11)	15	31	68	ErII	−1.35	1	−1.38	1
16	29	CuI	−2.87(05)	2	−2.88(01)	2							

to the number of lines used in the calculations. The results of other authors are given in inverse chronological order, i.e., the earliest results are at the end of the list.

We and other authors have analyzed the atmospheric abundances of a total of 35 elements in the metal-poor star HD 221170. Figure 4 shows the chemical composition of HD 221170 relative to the Sun.

The lithium abundance, $\log\epsilon(\mathrm{Li}) \leq -0.10$, indicates this element to be deficient, in agreement with the mean lithium abundance for stars on the upper giant branch derived by Gratton *et al.* [25]. We determined the oxygen abundance using the λ 6363.776 Å line; this element is slightly overabundant, in agreement with the measurements of other authors for this star and for metal-poor giants as a whole.

The abundances of carbon and nitrogen reported by Kraft *et al.* [20] suggest considerable mixing and dredge-up. The abundances of lithium and CNO elements are consistent with the star being on one of the evolutionary tracks of [46] on the ascending giant branch (Fig. 5). The position of HD 221170 is shown in accordance with the range of effective temperatures determined by various authors and the absolute magnitude found by Eggen [5], together with the quoted errors.

Sodium is underabundant relative to the solar ratio [Na/Fe], in good agreement with the results of other studies. The alpha-process elements (Mg, Si, Ca) are overabundant by up to 0.3–0.5 dex in halo stars. Our results for these elements also show them to be overabundant relative to iron and to be in good consistency with the results of other authors. The strong overabundance of potassium reported by Gratton and Sneden [19] requires confirmation.

The abundances of most iron-group elements are close to those obtained in previous studies. The only exceptions are manganese and cobalt. We find the former to be underabundant and the latter overabundant relative to iron and compared to the results of Gratton and Ortolani [18] and Gilroy *et al.* [7]. The nearly order-of-magnitude underabundance of copper agrees well with the results of Mishenina

Table 3. Atmospheric elemental abundances for HD 221170 from this paper and previous studies

Ion	Ref.	$[N/N_{\rm H}]$	Ion	Ref.	$[N/N_{\rm H}]$	Ion	Ref.	$[N/N_{\rm H}]$	Ion	Ref.	$[N/N_{\rm H}]$	Ion	Ref.	$[N/N_{\rm H}]$
LiI	[21]	<−1.2	SiI	*	−1.62	VI	*	−2.19	CoI	*	−1.76		[18]	−2.2
CI	[20]	−2.7		[12]	−1.70		[7]	−2.51		[7]	−2.09		[1]	−2.87
NI	[20]	−2.10		[23]	−1.85		[17]	−2.36	NiI	*	−2.09		[6]	−2.2
	[17]	−1.80		[19]	−1.55	CrI	*	−2.23		[23]	−2.31	LaII	*	−1.92
OI	*	−1.86		[1]	−1.52		[7]	−2.10		[7]	−2.01		[12]	−1.85
	[30]	−1.79	KI	[19]	−0.94		[1]	−2.73		[19]	−1.94		[26]	−1.65
	[12]	−1.75	CaI	*	−1.85	CrII	*	−2.08		[18]	−2.0		[7]	−1.27
	[29]	−1.71		[12]	−1.62		[7]	−2.32		[6]	−2.0	CeII	*	−1.94
	[17]	−1.88		[23]	−1.85	MnI	*	−2.60	CuI	*	−2.87		[12]	−2.20
	[24]	−1.80		[21]	−1.74		[18]	−2.1		[45]	−2.75		[7]	−1.66
	[6]	−2.0		[7]	−1.65		[1]	−2.41		[18]	−1.9	PrII	*	−1.53
NaI	*	−2.32		[19]	−1.52	FeI	*	−2.03	ZnI	*	−1.83		[7]	−1.47
	[12]	−2.12		[18]	−1.6		[12]	−2.05		[45]	−2.00	NdII	*	−1.61
	[44]	−2.40		[1]	−2.08		[29]	−1.95	SrI	*	−2.13		[12]	−1.73
	[24]	−2.30		[6]	−1.3		[26]	−2.15		[12]	−2.16		[26]	−1.40
	[21]	−2.40	ScII	*	−1.93		[44]	−2.15		[7]	−2.10		[7]	−1.48
	[19]	−2.04		[23]	−2.10		[24]	−2.10	SrII	*	−2.15	SmII	*	−1.57
	[18]	−2.5		[7]	−2.06		[21]	−1.96	YII	*	−2.15		[7]	−1.60
	[1]	−1.71		[17]	−2.18		[20]	−2.40		[26]	−2.29	EuII	*	−1.57
MgI	*	−1.79		[1]	−2.52		[7]	−2.02		[12]	−2.11		[26]	−1.35
	[12]	−1.67		[6]	−1.6		[19]	−1.96		[7]	−2.14		[24]	−1.44
	[44]	−1.83	TiI	*	−2.00		[18]	−1.8	ZrI	*	−2.18		[7]	−1.19
	[24]	−2.30		[7]	−1.89		[17]	−2.13	ZrII	*	−2.01	GdII	*	−1.55
	[23]	−1.83		[19]	−1.72		[1]	−2.59		[26]	−1.80		[7]	−1.40
	[19]	−1.58		[18]	−1.7		[6]	−1.9		[7]	−1.54	DyII	*	−1.32
	[1]	−1.77	TiII	*	−1.80	FeII	*	−2.03	MoI	*	−2.22		[26]	−1.30
AlI	*	<−1.73		[7]	−1.87		[7]	−2.17	BaII	*	−1.94		[7]	−1.08
	[24]	<−2.21		[1]	−2.29		[30]	−2.00		[12]	−1.70	ErII	*	−1.36
	[19]	−1.80					[17]	−2.07		[26]	−1.65			

*This paper.

et al. [45], who analyzed copper abundances for a large sample of halo stars.

Elements that form during neutron-capture processes represent a mix of nuclides produced by the s and r processes. For the first peak of neutron-capture elements (Sr, Y, Zr), the fraction of nuclides produced by the s process is higher than that produced by the r process. The underabundances of these three elements in the atmosphere of HD 221170 differ little from the underabundance of iron.

However, the second peak of neutron-capture elements is dominated by isotopes produced by the r process. For example, europium is often considered

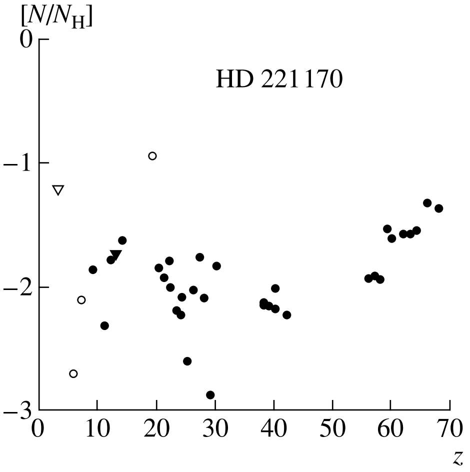

Fig. 4. Atmospheric elemental abundances for HD 221170 relative to the corresponding solar abundances. Triangles show upper limits. Filled and hollow symbols show the results of this paper and of previous studies for the abundances of lithium, carbon, nitrogen, and potassium.

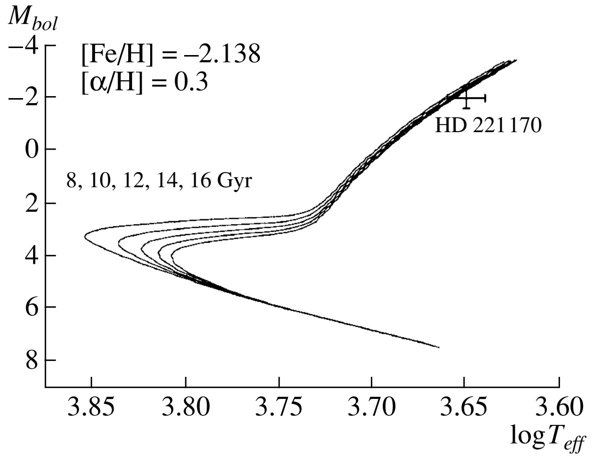

Fig. 5. Position of HD 221170 in the spectral type–luminosity diagram. Evolutionary tracks adopted from [46] for stellar models with the parameters indicated in the figure and ages spanning from 8 to 16 Gyr are also shown.

to be an r-process element, since 97% of europium nuclei in the solar system were formed via fast neutron capture.

The underabundances in the atmosphere of HD 221170 decrease beginning with atomic number 59 (praseodymium). A similar result was obtained by Gilroy *et al.* [7]. The heaviest elements we analyzed—dysprosium and erbium—are overabundant relative to iron by about 0.7 dex.

These results suggest that the protostellar cloud from which the star formed was enriched in r-process elements.

5. CONCLUSIONS

We have analyzed the atmospheric parameters of HD 221170. The effective temperature, surface gravity, microturbulence velocity, and iron abundance were determined by analyzing the rms variations in the iron abundances derived from calculations using a model-atmosphere grid. It is sufficient to use the lines of neutral iron alone. Data for lines of ionized iron can be used to decrease the errors and possible ambiguity of the results.

We calculated the atmospheric abundances of 30 elements for HD 221170 using the differential synthetic-spectrum method.

A compilation of data reported in earlier studies of this star was presented and used to check the trustworthiness of our results and to supplement the atmospheric abundance curve of HD 221170 with results for lithium, carbon, nitrogen, and potassium obtained in other studies.

As a result, we obtained an atmospheric abundance curve for this metal-poor star that spans 35 elements, including the first and second peaks of the neutron-capture elements. On the whole, the abundances of light elements, iron-group elements, and heavy elements up to cerium are similar to the corresponding abundances in most halo stars with similar iron abundances.

One property of the abundance curve for the metal-poor star considered here is that the relative abundances of elements heavier than cerium increase with atomic number, indicating that HD 221170 belongs to the small class of halo stars that are overabundant in heavy elements.

This is usually explained by suggesting that the star formed from material enriched in the products of supernova explosions in an early stage of the Milky Way's evolution. Such inhomogeneities in chemical composition were more likely in the past, when mixing of material in the Milky Way had only begun, suggesting that HD 221170 may be a fairly old star. We tried to estimate its age using evolutionary tracks computed by Bergbusch and VandenBerg [46]. HD 221170 is located off the tracks in Fig. 5, in the region corresponding to masses lower than $0.74M_{\odot}$ and ages greater than 16 Gyr. HD 221170 is thus one of the oldest objects in the Galaxy. There is no doubt that further analysis of this interesting star is required, especially studies of the abundances of elements heavier than erbium.

ACKNOWLEDGMENTS

We are grateful to L. Dellbouille and G. Rolland for providing the Liège atlas of solar spectrum.

We are also grateful to the teams maintaining the NASA ADS, SIMBAD, CADC, VALD, DREAM, and NIST databases, without whose data this work would not have been possible. V.F. Gopka acknowledges partial support from a Fundamental Research Grant from Chonbuk National University of the city of Chonju (South Korea). A.V. Yushchenko acknowledges partial support from the Astrophysical Research Center for the Structure and Evolution of the Cosmos (ARCSEC) of the Korean Science and Engineering Foundation (KOSEF) within the framework of the program of Scientific Research Centers (SRC).

REFERENCES

1. R. E. Luck and H. Bond, Astrophys. J. **244**, 919 (1981).
2. D. Gullberg and L. Lindegren, Astron. Astrophys. **390**, 383 (2002).
3. Masashi Chiba and Yuzuru Yoshii, Astron. J. **115**, 168 (1998).
4. H. E. Bond, Astrophys. J., Suppl. Ser. **44**, 517 (1980).
5. O. J. Eggen, Astron. J. **114**, 825 (1997).
6. G. Wallerstein, J. L. Greenstein, and R. Parker, Astrophys. J. **137**, 280 (1963).
7. K. K. Gilroy, C. Sneden, C. Pilachowski, *et al.*, Astrophys. J. **327**, 298 (1988).
8. V. F. Gopka, A. V. Yushchenko, T. V. Mishenina, *et al.*, Odessa Astron. Publ. **14**, 237 (2001).
9. A. Yushchenko, V. Gopka, Chulhee Kim, *et al.*, J. Korean Astron. Soc. **35**, 209 (2002).
10. C. Soubiran, D. Katz, and R. Cayrel, Astron. Astrophys. **133**, 221 (1998).
11. D. Katz, C. Soubiran, R. Cayrel, *et al.*, Astron. Astrophys., Suppl. Ser. **338**, 151 (1998).
12. T. V. Mishenina and V. V. Kovtyukh, Astron. Astrophys. **370**, 951 (2001).
13. F. Musaev, G. Galazutdinov, A. Sergeev, *et al.*, Kinemat. Phys. Select. Bodies **15**, 282 (1999).
14. G. A. Galazutdinov, Preprint No. 92, SAO RAN (Spets. Astrofiz. Obs. Ross. Akad. Nauk, Nizhniĭ Arkhyz, 1992).
15. A. V. Yushchenko, in *Proceedings of the 20th Stellar Conference of the Czech and Slovak Astronomical Institutes*, Ed. by J. Dusek (ISBN 80-85882-08-6, Brno, 1998), p. 201.
16. E. M. Leep and G. Wallerstein, Mon. Not. R. Astron. Soc. **196**, 543 (1981).
17. R. P. Kraft, N. B. Suntzeff, and G. E. Langer, *et al.*, Publ. Astron. Soc. Pac. **94**, 55 (1982).
18. R. G. Gratton and S. Ortolani, Astron. Astrophys. **137**, 6 (1984).
19. R. G. Gratton and C. Sneden, Astron. Astrophys. **178**, 179 (1987).
20. R. P. Kraft, C. Sneden, G. E. Langer, *et al.*, Astron. J. **104** (2), 645 (1992).
21. C. A. Pilachowski, C. Sneden, and J. Booth, Astrophys. J. **407**, 699 (1993).
22. R. G. Gratton, E. Garretta, and F. Castelli, Astron. Asrophys. **314**, 191 (1996).
23. C. A. Pilachowski, C. Sneden, and R. P. Kraft, Astron. J. **111** (4), 1689 (1996).
24. M. D. Shetrone, Astron. J. **112** (4), 1517 (1996).
25. R. G. Gratton, C. Sneden, E. Carretta, *et al.*, Astron. Astrophys. **354**, 169 (2000).
26. D. L. Burris, C. A. Pilachowski, T. E. Armandroff, *et al.*, Astrophys. J. **544**, 302 (2000).
27. J. P. Fulbright, Astron. J. **120**, 1841 (2000).
28. S. Snider, P. C. Allende, T. von Hippel, *et al.*, Astrophys. J. **562**, 528 (2001).
29. J. Melendez, B. Barbuy, and F. Spite, Astrophys. J. **556**, 858 (2001).
30. J. Melendez and B. Barbuy, Astrophys. J. **575**, 474 (2002).
31. E. A. Gurtovenko and R. I. Kostyk, *The Fraunhofer Spectrum and System of Solar Oscillator Strengths* (Kiev, 1989), p. 198 [in Russian].
32. A. V. Yushchenko, V. F. Gopka, V. L. Khokhlova, *et al.*, Astron. Lett. **25**, 453 (1999).
33. A. A. Boyarchuk, L. I. Antipova, M. E. Boyarchuk, and I. S. Savanov, Astron. Rep. **45**, 301 (2001).
34. R. L. Kurucz, CD-ROM No. 1-23 (Cambridge, MA, Smithsonian Astrophys. Obs., 1993).
35. R. L. Kurucz, Rev. Mex. Astron. Astrofis. **23**, 45 (1992).
36. B. W. Carney, D. W. Latham, R. P. Stefanik, *et al.*, Astron. J. **125**, 293 (2003).
37. N. E. Piskunov, F. Kupka, T. A. Ryabchikova, *et al.*, Astron. Astrophys. **112**, 525 (1995).
38. D. C. Morton, Astrophys. J., Suppl. Ser. **130**, 403 (2000).
39. J. Biemont, P. Palmeri, and P. Quinet, *Database of Rare Earths at Mons University* (2002); http://www.umh.ac.be/~astro/dream.html.
40. L. Dellbouille, G. Rolland, and L. Neven, *Photometric Atlas of the Solar Spectrum from λ 3000 to λ 10 000* (Institute de d'Astrophisique de l'Universitete de Liège, 1973).
41. N. Grevesse and A. J. Sauval, Astron. Astrophys. **347**, 348 (1999).
42. A. Arderberg and B. Virdeforce, Astron. Astrophys., Suppl. Ser. **36**, 317 (1979).
43. R. J. Rutten and E. B. J. van der Zalm, Astron. Astrophys., Suppl. Ser. **55**, 143 (1984).
44. R. B. Hanson, C. Sneden, R. P. Kraft, *et al.*, Astron. J. **116**, 1286 (1998).
45. T. V. Mishenina, V. V. Kovtyukh, C. Soubiran, *et al.*, Astron. Astrophys. **396**, 189 (2002).
46. P. A. Bergbusch and D. A. VandenBerg, Astrophys. J. **556**, 322 (2001).

Translated by A. Dambis

Astronomy Reports, Vol. 48, No. 7, 2004, pp. 588–596. Translated from Astronomicheskiĭ Zhurnal, Vol. 81, No. 7, 2004, pp. 648–657.
Original Russian Text Copyright © 2004 by Bisikalo, Boyarchuk, Kaĭgorodov, Kuznetsov, Matsuda.

A Model for Superoutbursts in SU UMa-type Binaries

D. V. Bisikalo[1], **A. A. Boyarchuk**[1], **P. V. Kaĭgorodov**[1], **O. A. Kuznetsov**[1,2], **and T. Matsuda**[3]

[1]*Institute of Astronomy, Moscow, Russia*
[2]*Keldysh Institute of Applied Mathematics, Moscow, Russia*
[3]*Kobe University, Kobe, Japan*

Received January 5, 2004; in final form, January 9, 2004

Abstract—We suggest a new mechanism for the superoutbursts in SU UMa binaries, in which the increase in the accretion rate resulting in a superoutburst is associated with the formation of a spiral "precessional" wave in the inner parts of the disk, where gas-dynamical perturbations are negligible. The existence of such waves was suggested by us previously. The results of three-dimensional gas-dynamical simulations have shown that a considerable increase in the accretion rate (by up to an order of magnitude) is associated with the formation of the precessional wave. The features of the precessional spiral wave can explain both the energy release in the superoutburst and all its observational manifestations. One distinguishing feature of superoutbursts in SU UMa-type stars is the formation of a "superhump" in the light curve. Our model reproduces well both the formation of a superhump and its observational features, including its period, which is up to 3–7% longer than the orbital period, and the detectability of the superhump independent of the orbital inclination of the binary. © *2004 MAIK "Nauka/Interperiodica"*.

1. INTRODUCTION

SU UMa-type variables are dwarf novas with orbital periods shorter than three hours that display "superoutbursts." This traditional definition of SU UMa stars has been extended to require the presence of a "superhump" during the superoutburst [1]. The normal outbursts in binaries of this type are fairly short and irregular and are well explained by standard models of dwarf novas (see, e.g., [1]). Superoutbursts are longer, rarer, and periodic. For instance, OY Car displays normal outbursts with amplitudes up to $\sim 3^m$ and durations of about three days every 25–50 days. The recurrence period of the superoutbursts is ~ 300 days, their amplitudes reach 4^m, and they can last up to two weeks. The observational data show that most superoutbursts have very similar profiles: the brightness rises sharply in a time that is $\sim 1/10$ of the superoutburst duration, after which the brightness very slowly declines over ~ 0.8 of the superoutburst duration, and the system then rapidly returns to the quiescent state. Superhumps with periods P_s that are a few percent longer than the orbital periods P_{orb} have been observed in all SU UMa stars for which high-speed photometric data have been obtained during a superoutburst. The superhumps typically have amplitudes of $\sim 0.3–0.4^m$ and are observed in all SU UMa stars, independent of orbital inclination.

The presence of periodic superoutbursts accompanied by superhumps place SU UMa dwarf novas among the most enigmatic phenomena in astronomy. Despite an abundance of observational data and theoretical models, our understanding of the nature of the SU UMa phenomenon is far from complete. We suggest here a new mechanism for the superoutbursts in SU UMa stars, whose essence is the following. (1) Between superoutbursts, an accretion disk is formed in the system and, as its mass grows, it becomes denser compared to the matter flowing from the inner Lagrange point L_1, and its inner regions become impervious to gas-dynamical perturbations. (2) A "precessional" spiral wave is generated in the inner parts of the disk after the gas-dynamical perturbations become negligible [2]. (3) The formation of this spiral density wave is accompanied by a substantial (up to an order of magnitude) increase in the accretion rate and, consequently, by the development of a superoutburst. (4) The retrograde precession of the spiral density wave and the compact size of the inner zone of energy release can explain the appearance of the superhump and its features, such as the facts that the superhump period is longer than the orbital period and that the superhump is detectable irrespective of the orbital inclination of the binary. The formation of a region that is not disturbed by gas-dynamical perturbations, along with the accumulation of a certain mass in the disk, can easily explain the high degree of regularity of the superoutbursts as a consequence of a constant mass-transfer rate in the system. This substantially simplifies the model, since we do not need to invoke variations in the conditions on the donor star in order to explain the periodic superoutbursts.

We present this new mechanism to explain the superoutbursts in SU UMa stars as follows. Section 2 contains a brief review of the observational data and previous theoretical models for superoutbursts. Section 3 presents the results of three-dimensional gas-dynamical simulations of the morphology of the gaseous flows in semidetached binaries and a description of the basic features of the precessional spiral density wave that forms in the inner parts of the cool disk. A comparison of the observational manifestations of superoutbursts and superhumps and computational results follows in Section 4. This comparison confirms the consistency of the new model.

2. OBSERVATIONS OF SUPEROUTBURSTS AND THEORETICAL MODELS

Following Warner (see his monograph [1]), the main features of superoutbursts and superhumps in SU UMa variables can be summarized as follows.

A superoutburst has the following typical features:

A.1. It is $\sim 0.5{-}1^m$ brighter than a normal outburst. The total energy release in a superoutburst is $E \simeq 10^{40}$ erg, about an order of magnitude larger than that in a normal outburst.

A.2. Superoutbursts last appreciably longer than normal outbursts and can have durations as long as several weeks.

A.3. The intervals between superoutbursts are very long, as a rule, hundreds of days, but even exceeding several thousand days for some systems. The intervals between superoutbursts in a given system are approximately equal.

A.4. All superoutbursts have the same type of profile: a rapid rise followed by a long, sloping plateau and rapid decline.

A.5. The slope of the brightness plateau is almost invariant: $\sim 9 \pm 1$ day/mag; i.e., the brightness declines by one magnitude in approximately nine days. Since superoutbursts last for ~ 10 to ~ 30 days, the brightness varies by $\sim 1{-}3^m$ along the plateau.

A.6. During the rise of the superoutburst, the brightness and color change in the same way as for normal outbursts in the same system; i.e., the superoutbursts begin like normal outbursts.

A.7. No normal outbursts have been detected during or immediately after superoutbursts. This suggests that normal outbursts and superoutbursts are not independent phenomena.

A.8. The superhump appears some time after the superoutburst maximum, as a rule, 1/20–1/2 of the plateau duration.

A.9. The light curves of eclipsing SU UMa systems have dips at phases ~ 0.25 and 0.75, which are usually interpreted as being associated with an increase in the vertical thickness of the disk at these phases. The UV fluxes also show minima at phases ~ 0.2 and 0.8.

A.10. Line profiles show that a substantial fraction of the disk is in noncircular motion during a superoutburst and that the noncircular component rotates with the superhump period P_s; hence, noncircular motion is closely linked to the superhump phenomenon.

A.11. In some SU UMa stars, both normal orbital humps and a modulation with the superhump period shifted in phase by $\sim 180°$ are observed after the end of a superoutburst. This phenomenon is known as the "late superhump."

Superhumps have the following features.

B.1. Superhumps have been detected in all SU UMa stars for which high-speed photometric data have been obtained during superoutbursts.

B.2. As is mentioned above, analyses of line profiles show that the superhump phenomenon is related to noncircular motion of some disk components.

B.3. The superhump period is 3–7% longer than the orbital period.

B.4. In many cases, a continuous decrease in the superhump period is observed during a superoutburst (by $\approx 1.25\%$).

B.5. Superhumps are detected in all SU UMa stars, independent of orbital inclination.

B.6. Typical amplitudes of the superhumps are $\sim 0.3{-}0.4^m$.

B.7. The superhump amplitude decreases faster than the system brightness; therefore, as a rule, the superhump has already disappeared by the end of the sloping plateau of the superoutburst.

B.8. Multicolor photometry of superhumps shows reddening at their maxima, so that there is an inverse correlation between the color temperature and the brightness of a superhump.

B.9. The technique of eclipse mapping has made it possible to identify sources of the superhump light and to distinguish three regions in the accretion disk from which this light is emitted.

A number of models have been suggested to explain these features of superoutbursts and superhumps. The first models were based on possible asynchronous rotation of the donor [3], a weak magnetic field of the accretor [4], eccentricity of the binary orbit [5], mass-transfer variations [6, 7], and instability of the accretion disk [8], as well as a combination of the last two phenomena [9]. A review and critique of early models can be found in the monograph by Warner [1].

In 1982, Vogt [10] suggested that the accretion disk becomes eccentric during a superoutburst. Later, Osaki [8] and Mineshigi [11] put forward the idea of a precessing eccentric disk. In 1988, Whitehurst [12] numerically confirmed the possibility of disk precession for sufficiently small component-mass ratios, q. Currently, models with a precessing, eccentric accretion disk are most commonly applied to superoutbursts in SU UMa stars. In these models, the precession results from instability in the disk due to the eccentric $3:1$ Lindblad resonance [13]. This resonance[1] is located inside the disk only if the component-mass ratio is sufficiently small: $q \lesssim 0.22$ (the radius of the disk can be determined by applying, for example, the formula of Paczyński [14]). These values of q are in a good agreement with the typical q values for SU UMa stars.

Thus, according to [8, 13], the onset of a superoutburst can be explained as follows. In the course of accretion, matter is accumulated in the disk and the disk radius increases. Short, normal outbursts occur until the disk radius grows to a size that corresponds to the eccentric $3:1$ Lindblad resonance. The outbursts may be triggered by thermal instability [16, 17]. When the resonance is reached, both thermal and tidal instabilities can set in, the rate of accretion sharply increases, and a superoutburst occurs. During the superoutburst, the disk becomes eccentric and begins to precess; this precession results in the formation of the superhump.

However, this model cannot explain all the observational manifestations of SU UMa stars. Most importantly, it cannot explain the formation of superhumps in binaries that do not display normal humps in their light curves in quiescence, i.e., in systems with small inclination angles (e.g., V436 Cen, WX Hyi, SU UMa [1]).

The precessing, eccentric accretion-disk model also fails to explain the origin of superoutbursts and superhumps in systems with relatively large component-mass ratios ($q > 0.22$, as for VY Scl [15]).

It is especially important to note the failure of this model to explain late superhumps. Osaki [7] and Whitehurst [12] suggested that the eccentric accretion disk survives for several days after the end of the superoutburst and that the modulation of the brightness of a hot spot produces the late superhumps (see also [18, 19]). However, an independent determination of the disk eccentricity for OY Car does not agree with this model [20, 21].

Given these inconsistencies with the observations, it is fair to say that no fully realistic model for superoutbursts and superhumps in SU UMa binaries has been formulated previously.

3. THREE-DIMENSIONAL GAS-DYNAMICAL SIMULATIONS OF COOL ACCRETION DISKS: FEATURES OF THE PRECESSIONAL SPIRAL DENSITY WAVE

Our qualitative analysis and three-dimensional gas-dynamical simulations of the morphology of gaseous flows in semidetached binaries for low gas temperatures ($\sim 10^4$ K) enabled us to identify characteristic features of the structure of cool accretion disks [2, 22]. In general, the flow structure is qualitatively the same as for the case of high gas temperatures [23–25]. The gas-dynamical structure of the flow is governed by the stream of matter from L_1, the accretion disk, the circumdisk halo, and the circumbinary envelope. The interaction between the stream and disk is shockless, and the interaction of the matter of the circumdisk halo and circumbinary envelope with the stream leads to the formation of a shock with the form of a "hot line" along the edge of the stream. However, reduction of the gas temperature leads to several differences as well. A cool accretion disk becomes considerably denser (compared to the matter in the stream) and thinner, and its shape is nearly circular rather than quasi-elliptical. A second arm of the tidal spiral shock (see [26–28]) is formed; neither arm of the shock approaches the accretor, and both are located in the outer parts of the disk. The absence of appreciable action of the stream on the dense inner regions of the disk and the fact that all the shocks (the hot line and two arms of the tidal shock) are located in the outer part of the disk result in a new element of the flow structure in the low-temperature case: there is an inner region of the accretion disk where the influence of the gas-dynamical perturbations noted above is negligible.

The formation of a region in the inner parts of the disk that is free from gas-dynamical perturbations enables us to treat this region simply as a slightly eccentric disk immersed in the gravitational field of the binary; the typical size of this region is ~ 0.2–$0.3A$, where A is the binary separation. It is known (see, e.g., [1, 29]) that particles revolving around one of the binary components will precess due to the influence of the companion. This precession is retrograde, and the rate of precession is proportional to the orbit

---

[1] Nonaxisymmetric perturbations in the disk can be expressed as $\exp[i(k\varphi - l\Omega t)]$, where the integers (k, l) specify a particular mode. Lubow [13] has shown that coupling between the density perturbations produced by a tidal perturbation with a (3,3) mode and an eccentric perturbation with a (1,0) mode excites two-armed spiral density waves with a (2,3) mode at the eccentric inner Lindblad resonance; the location of this resonance is determined by the condition $\omega = m\Omega/(m-2)$ for $m = 3$.

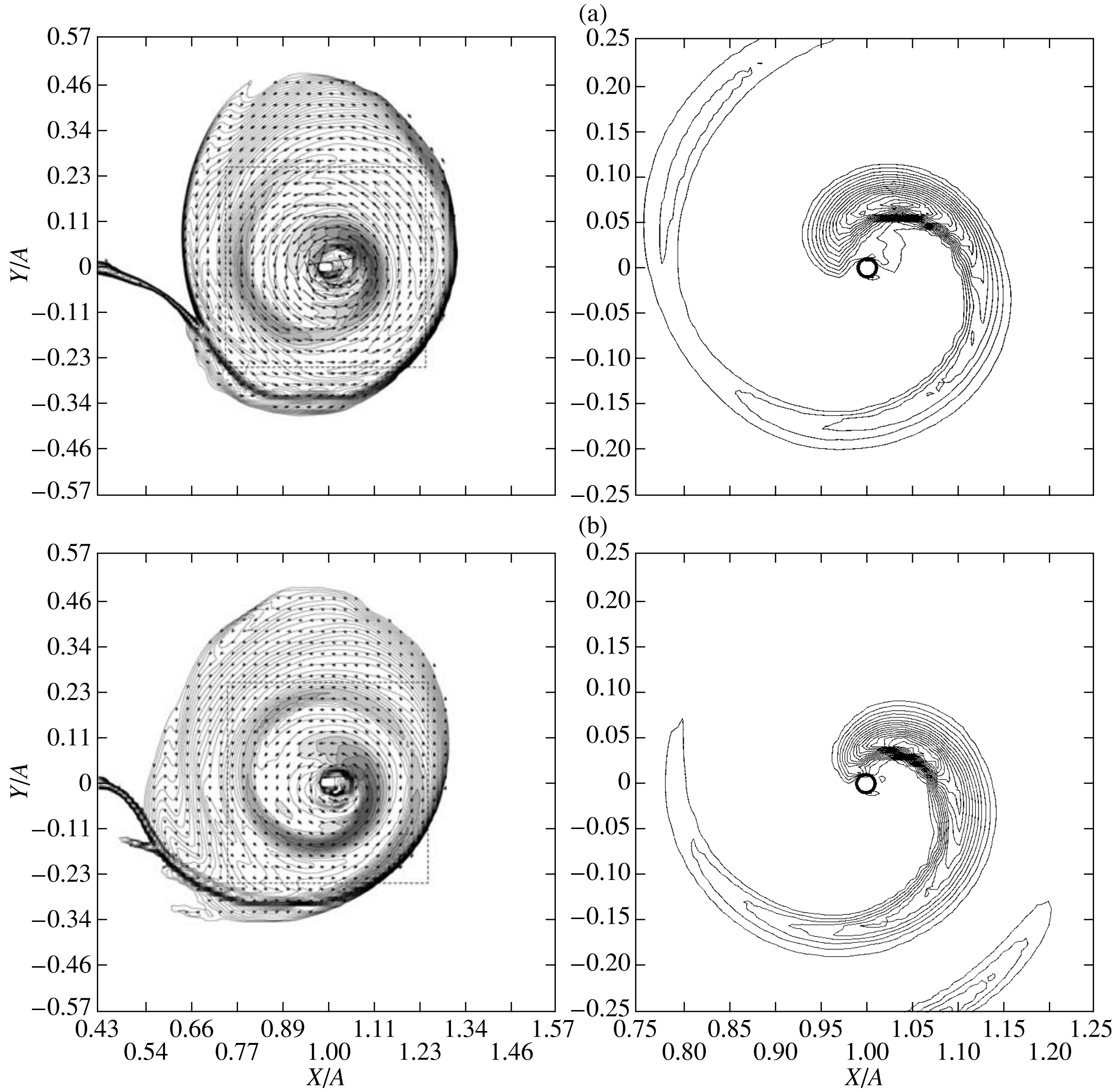

Fig. 1. (a) Left: contours of density and velocity vectors in the equatorial plane of the binary; right: contours of the radial flux of matter in the central parts of the disk. (b–d) Same as (a) for $t = P_{orb}, 2P_{orb}$, and $3P_{orb}$.

radius; i.e., it decreases with approach to the accretor. Retrograde precession obeying this precession-rate law results in the formation of a "precessional" spiral density wave in the inner part of the disk [2]. This wave is formed by the locus of the apastrons of the stream lines. The presence of the density wave together with the fact that the velocity of the particles increases after passing apastron leads to an increase in the radial component of the mass flux $F_{rad} = nv_r$ due to the increase of both the density n and the radial velocity component v_r directed toward the accretor. The increase in the radial component of the mass flux behind the wave increases the accretion rate in the region where the precessional wave approaches the accretor.

The left panels of Fig. 1 show the density distribution and velocity vectors in the equatorial plane for four times, starting from an arbitrary time and then following with times separated by one orbital period, i.e., for $t = t_0$, $t_0 + P_{orb}$, $t_0 + 2P_{orb}$, and $t_0 + 3P_{orb}$. The right panels show the distribution of the radial flux of matter in the central regions of the disk for the same times. These distributions show the formation of a dense, circular accretion disk and a compact circumdisk halo in the binary. The interaction of the circumdisk halo and circumbinary envelope with the stream results in the formation of a hot line located outside the disk. A two-armed tidal spiral shock is formed in the disk, with both of its arms located in the outer part of the disk, so that they do not reach

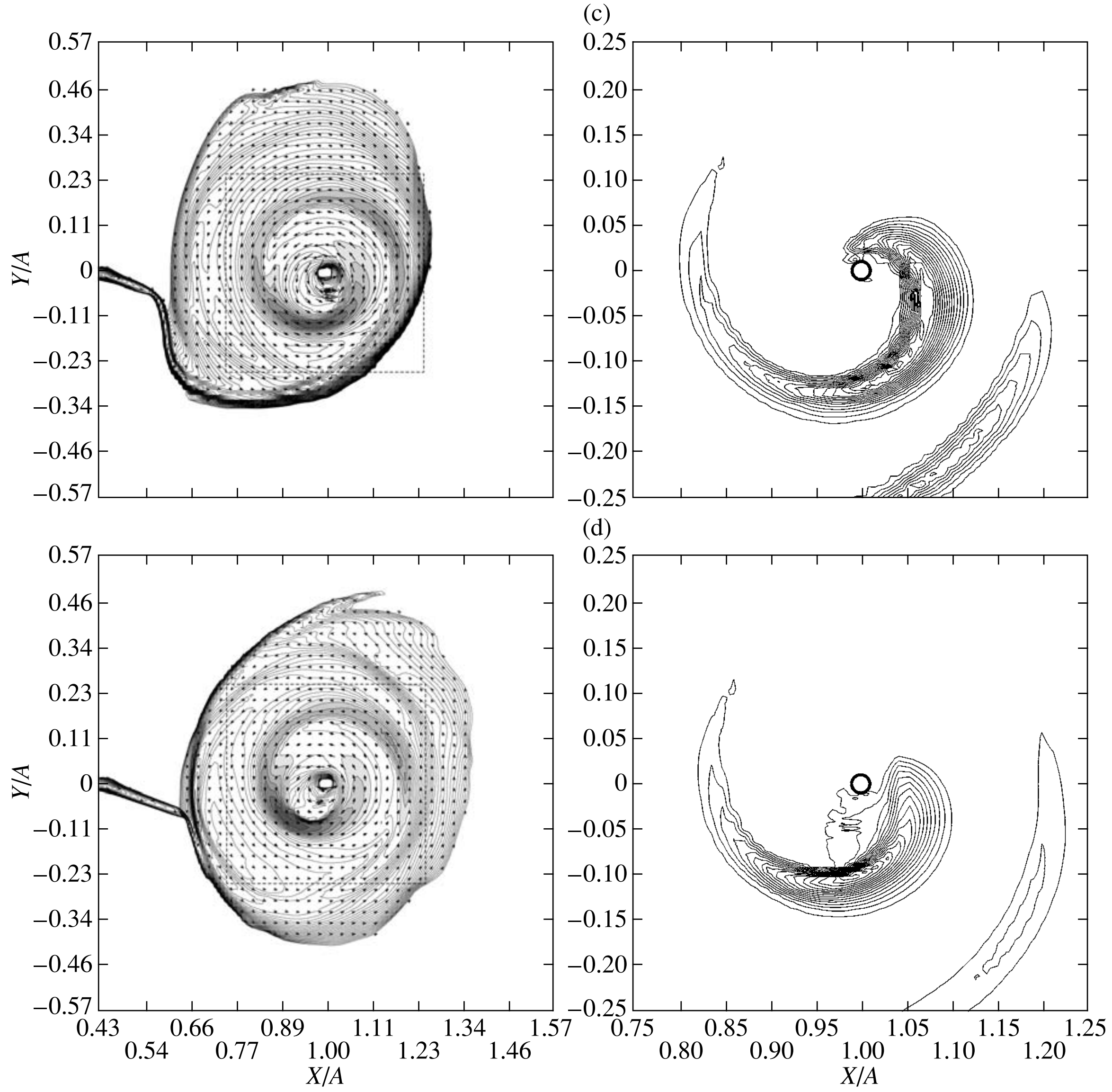

Fig. 1. (Contd.)

the accretor. Another spiral wave in the inner part of the disk is also clearly visible.

These simulations were made for a binary with characteristics close to those of the dwarf nova IP Peg: $M_1 = 1.02M_\odot$, $M_2 = 0.5M_\odot$, and $A = 1.42R_\odot$. The computation results for the four times show that the precession of the inner spiral wave is retrograde and the velocity of its revolution in the inertial frame (i.e., the observer's frame) is ≈ -0.13 of a revolution per binary orbital period. The distribution of the radial flux of matter in the disk shows that, starting from the outer radius of the wave, this flux increases as it approaches the accretor and reaches a maximum that is more than an order of magnitude higher than the flux in regions of the disk outside the wave. Thus, the accretion rate will be enhanced by more than a factor of ten due to the formation of this wave.

The outbursts in IP Peg differ from the superoutbursts of SU UMa stars. This may be due to the relatively small size of the disk and, accordingly, the small size of the region that is free of gas-dynamical perturbations. However, a typical SU UMa binary has a component-mass ratio of $q = M_2/M_1 \approx 0.1$, which is substantially lower than the q for IP Peg. A decrease in q implies an increase in the size of the accretor's Roche lobe ($x_{\mathrm{L}_1} \to A$ as $q \to 0$, where x_{L_1} is the distance between the accretor and the inner Lagrange point L_1), so that the system can harbor a larger accretion disk. According to Paczyński [14], the relative size of the accretion disk depends on q as

$R_d/A = \dfrac{0.6}{1+q}$; i.e., it can reach values of $0.54A$ in SU UMa stars. In turn, this means that the size of the region that is free of gas-dynamical perturbations can be large in these systems, making the precessional spiral-wave mechanism efficient.

To test these ideas, we carried out a gas-dynamical simulation for a binary with the parameters of OY Car ($q = 0.147$): $M_1 = 0.95M_\odot$, $M_2 = 0.14M_\odot$, and $A = 0.69R_\odot$. The results of this simulation show that the precessional wave originates $\approx 0.25A$ from the accretor, its velocity in the inertial coordinate system is ≈ -0.03–0.04 of a revolution per binary orbital period, and the accretion rate behind the wave increases by more than an order of magnitude.

The kinematic properties of the precessional wave and the substantial increase in the accretion rate due to this wave suggest that it can provide an explanation for superoutbursts and superhumps in SU UMa stars.

4. BASIS OF THE NEW MECHANISM FOR SUPEROUTBURSTS

Let us briefly summarize the basis of the proposed mechanism for superoutbursts and superhumps in SU UMa binaries. The mechanism assumes that an accretion disk forms between superoutbursts, which becomes denser compared to the matter flowing from L_1 as matter accumulates onto it. Hence, the inner parts of the disk cease to undergo gas-dynamical perturbations. A precessional spiral density wave forms in the unperturbed part of the disk, accompanied by a substantial (by up to an order of magnitude) increase in the accretion rate. The growth of the accretion rate leads to a brightening of the star, i.e., to the development of a superoutburst. The retrograde precession of the density wave at a rate of a few hundredths of a revolution per binary orbital period and the compact size of the central region of energy release can explain the formation of the superhump, as well as its observational features.

The observational features of superoutbursts and superhumps in SU UMa stars are listed in Section 2. To be sure that the precessional spiral wave can explain these features, let us compare each of the computed and observed features of superoutbursts and superhumps in turn.

Energy release, recurrence time, and duration of superoutbursts (features A.1–A.3). Our mechanism proposes that the energy released in superoutbursts and their periodicity are determined by the mass and accumulation time of the accretion disk. About 50% of the disk mass is accreted during a superoutburst (see, e.g., [1]), resulting in an energy release of $E \simeq 10^{40}$ erg. Hence, assuming that about half of the energy is radiated away, we can estimate the mass of the accreted part of the disk $\left(\dfrac{1}{2}m_d\right)$ via the formula $E \simeq \dfrac{1}{2}\dfrac{GM_1}{R_1}\dfrac{1}{2}m_d$. Adopting values typical for SU UMa stars, $M_1 \simeq 1M_\odot$ and $R_1 \simeq 10^9$ cm, we obtain for the mass of the disk $m_d \simeq 1.5\times10^{-10}M_\odot$. Since the outburst recurrence time (i.e., the time for the accumulation of the mass $\dfrac{1}{2}m_d$) is close to one year, the average mass-transfer rate is close to $10^{-10}M_\odot$/year. This estimate is consistent with estimates for the mass-transfer rates in cataclysmic variables. Differences in the recurrence times for different systems are easily explained by differences in the mass-transfer rate. The implied range in the mass-transfer rate is reasonable—the mass-transfer rate for a superoutburst recurrence time of $\sim 100^{\rm d}$ is $\dot{M} \simeq 3\times10^{-10}M_\odot$/yr and decreases to $\simeq 3\times10^{-11}M_\odot$/yr for a recurrence time of $\sim 1000^{\rm d}$. The high regularity of superoutbursts is determined by the constancy of the mass-transfer rate within a given binary (any evolutionary changes occur on much longer time scales and can be neglected). The duration of a superoutburst is determined by the ratio of the mass of accreted matter and the accretion rate. In a steady-state regime, the accretion rate is approximately equal to the mass-transfer rate, so that an increase in the accretion rate by an order of magnitude or more during a superoutburst implies ratios of the recurrence time and superoutburst time of 10–20, in good agreement with observations.

The superoutburst profile (features A.4 and A.5). The rapid growth of the brightness at the onset of a superoutburst is due to the increased accretion rate after the formation of the precessional spiral wave in the disk. The formation of this wave is due to the enhanced efficiency of the outward transport of angular momentum in the disk. It is natural to suppose that the angular-momentum transfer rate is constant in quiescence (a quasi-steady state). In the proposed mechanism, the innermost regions of the disk are accreted first, followed by more distant ones. Since the angular momentum in the disk is distributed as $r^{1/2}$, the accretion of matter from distant orbits requires more and more time. As a consequence, the accretion rate will decrease with time, manifest as the extended sloping plateau of the light curve. It is interesting that, since the angular-momentum transport is determined by the characteristics of the wave rather than the parameters of the binary, our mechanism provides a natural explanation for the similarity of the plateau slope for different systems. The slope is $\sim 9\pm1$ days/mag; i.e., the brightness declines by one magnitude (the accretion rate decreases by a factor of 2.5) in nine days. This means that, every nine days, the radius of the disk regions that begin to accrete increases by a factor of 2.5^2, i.e., by six to seven accretor radii ($\sim 0.1A$). Based on these considerations and using the observed values of the superoutburst duration and the plateau slope, we can estimate the linear size of the wave (the distance between the outer and inner radii that correspond to the wave initialization and termination points) and, consequently, derive certain physical characteristics of the disk. If both the wave scale (the radius of the accreted part of the disk) and the energy release during the superoutburst are known, we can estimate both the mass and density of the disk. Variations in the superoutburst duration are due to variations in the wave size. Hence, for given binary parameters and known maximum disk radius, there exists an upper limit for the superoutburst duration in the system. In a typical SU UMa star, $q \simeq 0.1$, so that the maximum radius of the disk and the maximum possible wave scale cannot exceed $0.54A$ [14]. As a consequence, the maximum brightness variations of a typical star of this type have amplitudes less than $\sim 4.25^m$, and the maximum superoutburst duration is $\sim$40 days. If only half of the disk mass is accreted, then, assuming that the density of the disk matter is constant, we find that the wave scale is a factor of $\sqrt{2}$ smaller than the disk radius. Thus, the maximum brightness-variation amplitude is $\sim 3.9^m$, and the maximum duration of a superoutburst, $\sim$35 day. Observations to date have not revealed SU UMa stars that do not satisfy these criteria.

Relation between superoutbursts and normal outbursts (features A.6 and A.7). Our mechanism proposes that superoutbursts are related to a sharp increase in the accretion rate. Normal outbursts are likewise due to enhancements in the accretion rate. Hence, although the physical nature of the increase of the accretion rate in these two cases is different (the formation of the precessional spiral wave in the former case and instability in the disk in the latter case), the observational manifestations of both types of outbursts could be similar, especially in their early stages. This may explain the fact that the superoutbursts begin in the same way as normal outbursts (feature A.6). The absence of normal outbursts during or immediately after superoutbursts (feature A.7) does not prove that there is a connection between the two types of outbursts. In our mechanism, normal outbursts and superoutbursts have different origins, but we can explain this feature as follows. The superoutburst consumes the entire inner region of the disk, making any kind of outburst impossible before this region is refilled with new material. The rate of filling is determined by the efficiency of the outward transport of angular momentum (for instance, due to turbulent viscosity), but even if the efficiency is high, the refilling time is considerable and, in general, comparable to the duration of an outburst.

Formation of the superhump (feature A.8). The formation of a superhump may also be a consequence of the development of the precessional spiral wave in the disk. The increase in the accretion rate behind the wave is spatially localized in azimuth, so that matter approaches the surface of the accretor within a fairly compact zone. As the outburst develops, both heating of the gas and the difference of the rotational velocities of the accretor and wave will increase this impact zone, forming a closed belt. However, in any case, the system will have a “core” in the region of energy release, where the accretion rate will be enhanced. This core is fairly compact and is located at the accretor surface, so that it will be eclipsed at some orbital phases. The detection (“formation”) of the superhump occurs when the core emerges from eclipse and is oriented toward the observer. The core is associated with the precessional spiral wave, and its rotational velocity is determined by the velocity of the wave. The amplitude of the core is determined relative to the energy release over the entire surface of the accretor and, therefore, depends on the properties of the accretor and disk, not the properties of the wave. The fact that the superhump is generally detected some time after the beginning of the superoutburst is a consequence of the compact size of the core region. If the wave location (position of the superhump) has a uniform probability distribution in azimuth at the onset of the outburst, then, on average, a time equal to about half of the precession period should pass before the core emerges from eclipse (i.e., is oriented toward the observer) and is manifest as a superhump.

Details of the disk structure obtained from observations of superhumps (features A.9 and A.10). Observations of superoutbursts in eclipsing SU UMa systems display dips in the light curves at phases $\sim$0.2–0.25 and 0.75–0.8 in both the optical and UV. In our model, the two arms of the tidal shock wave are located at these phases. Heating of the gas in the shocks increases the disk thickness at these phases, which can explain the observed dips. The noncircular motion of the part of the disk rotating with the superhump period P_s (feature A.10) is a natural property of our model, since the precessional spiral wave forms in the region of noncircular motion and moves with the superhump period. The detection of these regions is a direct confirmation of our model.

Formation of the “late superhump” (feature A.11). In some SU UMa stars, both the normal orbital humps and a brightness modulation with the superhump period but shifted in phase by $\sim$180° are observed for several days after completion of the superoutburst. This is known as the “late superhump.”

Our model can explain the formation of the late superhump as follows. (1) The precessional spiral wave forms in the region of the apastrons of the eccentric flow lines. (2) During the superoutburst, the accretion of matter forms an empty zone in the inner part of the disk (or, more precisely, a zone of reduced density), which is noncircular in shape—it is elongated where the wave passed and closer to the accretor on the opposite side (in the region of the flow-line periastrons). (3) After the disappearance of the wave and the completion of the superoutburst, the accretion disk has been replaced by an elliptical ring of matter, with the periastron of the ellipse shifted in phase by ~180° compared to the former location of the wave (or, in other words, compared to the superhump phase). (4) After the completion of the superoutburst, the transport of angular momentum and, consequently, accretion are due to viscosity, i.e., processes with uniform azimuthal distributions. Therefore, matter that loses angular momentum axially symmetrically will reach the surface of the accretor more readily if it was initially closer to the accretor, i.e., in the region of the periastron of the elliptical ring. This results in the formation of the late superhump, which will be manifest as a brightness modulation with the superhump period but shifted in phase by $\sim$180°. The lifetime of the late superhump is determined by the time scale for circularization of the flow lines in the disk.

Superhump characteristics (features B.1–B.5). The detection of superhumps in all SU UMa stars for which high-speed photometric data have been obtained during superoutbursts provides evidence for a common origin for superhumps and superoutbursts. In our model, both the superhump and superoutburst are associated with the development of the precessional spiral wave in the disk. Since this wave forms in a region of noncircular flow lines and the velocity of its rotation is determined by the rate of retrograde precession of the flow lines (of the order of several hundredths of a revolution per orbital period), the relation between the superhump and noncircular rotation of the disk (feature B.2) and the fact that the superhump period is 3–7% longer than the orbital period (feature B.3) are natural consequences of this superhump mechanism. The superhump period is defined by the period of the wave P_{wav} and the orbital period P_{orb} via the relation $P_s = \dfrac{P_{wav}P_{orb}}{P_{wav} - P_{orb}}$. The reduction of the superhump period during the superoutburst (feature B.4) is also quite natural if the superhump is a consequence of the development of the precessional spiral wave in the disk. Indeed, the precessional period of the wave is determined by both fast outer and slow inner flow lines. As the outburst develops, the linear scale of the wave will be reduced and the slow inner flow lines will exert more influence, making the rate of rotation of the wave decrease (so that P_{wav} will increase), which is observed as a reduction in the superhump period. The presence of superhumps in the light curves independent of the binary inclination (feature B.5) can be explained by the existence of a compact core of energy release that is spatially localized in azimuth. In this case, this core will not be observable at certain orbital phases and the brightness of the system will be modulated.

Superhump amplitude (features B.6 and B.7). Typical superhump amplitudes are $\sim 0.3{-}0.4^m$. This means that the energy released in the core of the region of energy generation is $\sim$10% higher than at the rest of accretor surface. This is quite natural, since the accretor will have revolved several times and the accretion zone will have acquired the shape of a belt with a small core by the time the superhump is detected (see also the comparison of the model with feature A.8). For systems where the superhump is observed immediately after the onset of the superoutburst [30], the core is visible from the very onset of the superoutburst and the belt forms later, as matter is accreted and smeared over the surface of the accretor. This effect is manifest as a variation of the superhump shape during the outburst: the shape is initially asymmetric (since the rate of energy release and the size of the region of energy release are different for phases before and after the superhump) but becomes symmetric when the belt is formed. The more rapid reduction of the superhump amplitude compared to the brightness of the system (feature B.7) is due to the accretion from more and more distant orbits as the superoutburst develops and the consequent stretching of the core in azimuth. This reduces the ratio of the energy release in the compact core and the total energy release; i.e., the superhump amplitude decreases more rapidly than the outburst amplitude.

Inverse correlation between superhump color temperature and brightness (feature B.8). A superhump is observed when the core of the zone of energy release is oriented toward the observer. At this time, the precessional spiral density wave is located between the accretor and observer. This may lead to enhanced absorption (reddening) at the superhump maximum compared to its minimum, when the wave does not affect observations of the superhump.

Superhump light sources (feature B.9). Eclipse mapping of SU UMa stars [31] has revealed three sources of superhump emission in the outer regions of the disk. Their locations coincide with the positions of three components of our model: two arms of the tidal spiral shock and the hot-line shock. Eclipse mapping has not detected the compact zone of energy release at the accretor surface, possibly because eclipse mapping has "excess azimuthal symmetry" and so stretches features in azimuth [1]. This does not prevent the use of this technique for investigations of the outer parts of the disk, where the linear scale of the flow components is large, but the method could fail to detect a bright spot in a small region on the accretor surface.

Summarizing our comparison of the computed and observed features of superoutbursts and superhumps, it is now possible for the first time to explain all the observed features, without exception (including the late superhumps, which were very difficult to interpret previously), in a natural way within a single model.

ACKNOWLEDGMENTS

This work was partially supported by the Russian Foundation for Basic Research (project nos. 02-02-16088, 02-02-17642, 03-01-00311, 03-02-16622), the Program for Support to Leading Scientific Schools (project NSh 162.2003.2), the Federal Scientific and Technological Program in Astronomy, the Programs of the Presidium of the Russian Academy of Sciences "Mathematical Modeling and Intellectual Systems" and "Nonstationary Phenomena in Astronomy," and INTAS (grant no. 00-491). O. A. Kuznetsov thanks the Russian Science Support Foundation for financial support.

REFERENCES

1. B. Warner, *Cataclysmic Variable Stars* (Cambridge Univ. Press, Cambridge, 1995).
2. D. V. Bisikalo, A. A. Boyarchuk, P. V. Kaĭgorodov, *et al.*, Astron. Zh. (2004, in press).
3. H. C. Vogt, Astron. Astrophys. **36**, 369 (1974).
4. J. Papaloizou and J. E. Pringle, Astron. Astrophys. **70**, L65 (1978).
5. J. Papaloizou and J. E. Pringle, Mon. Not. R. Astron. Soc. **189**, 293 (1979).
6. H. C. Vogt, Astron. Astrophys. **88**, 66 (1980).
7. Y. Osaki, Astron. Astrophys. **144**, 369 (1985).
8. Y. Osaki, Publ. Astron. Soc. Pac. **41**, 1005 (1989).
9. W. J. Duschl and M. Livio, Astron. Astrophys. **241**, 153 (1989).
10. H. C. Vogt, Astrophys. J. **252**, 563 (1982).
11. S. Mineshige, Astrophys. J. **355**, 881 (1988).
12. R. Whitehurst, Mon. Not. R. Astron. Soc. **232**, 35 (1988).
13. S. H. Lubow, Astrophys. J. **381**, 268 (1991).
14. B. Paczyński, Astrophys. J. **216**, 822 (1977).
15. J. R. Murray, B. Warner, and D. T. Wickramasinghe, Mon. Not. R. Astron. Soc. **315**, 707 (2000).
16. E. Meyer-Hoffmeister and H. Ritter, in *Realm of Interacting Binary Stars*, Ed. by J. Sahade, Y. Kondo, and G. McClusey, p. 143.
17. J. K. Cannizzo, in *Accretion Disks in Compact Stellar Systems*, Ed. by J. C. Wheeler, p. 6.
18. D. J. Rolfe, C. A. Haswell, and J. Patterson, Mon. Not. R. Astron. Soc. **324**, 529 (2001).
19. V. Buat-Ménard and J.-M. Hameury, Astron. Astrophys. **386**, 891 (2003).
20. H. van der Woerd, M. van der Klis, J. van Paradijs, *et al.*, Astrophys. J. **330**, 911 (1988).
21. F. V. Hessman, K. H. Mantel, H. Barvig, and R. Shoembs, Astron. Astrophys. **263**, 147 (1992).
22. D. V. Bisikalo, A. A. Boyarchuk, P. V. Kaĭgorodov, and O. A. Kuznetsov, Astron. Zh. **80**, 879 (2003) [Astron. Rep. **47**, 809 (2003)].
23. D. V. Bisikalo, A. A. Boyarchuk, O. A. Kuznetsov, and V. M. Chechetkin, Astron. Zh. **77**, 31 (2000) [Astron. Rep. **44**, 26 (2000)].
24. D. Molteni, D. V. Bisikalo, O. A. Kuznetsov, and A. A. Boyarchuk, Mon. Not. R. Astron. Soc. **327**, 1103 (2001).
25. A. A. Boyarchuk, D. V. Bisikalo, O. A. Kuznetsov, and V. M. Chechetkin, *Mass Transfer in Close Binary Stars* (Taylor & Francis, London, 2002).
26. K. Sawada, T. Matsuda, and I. Hachisu, Mon. Not. R. Astron. Soc. **219**, 75 (1986).
27. K. Sawada, T. Matsuda, and I. Hachisu, Mon. Not. R. Astron. Soc. **221**, 679 (1986).
28. K. Sawada, T. Matsuda, M. Inoue, and I. Hachisu, Mon. Not. R. Astron. Soc. **224**, 307 (1987).
29. S. Kumar, Mon. Not. R. Astron. Soc. **223**, 225 (1986).
30. W. Krzeminski and N. Vogt, Astron. Astrophys. **144**, 124 (1985).
31. D. O'Donoghue, Mon. Not. R. Astron. Soc. **246**, 29 (1990).

Translated by L. Yungel'son

Astronomy Reports, Vol. 48, No. 7, 2004, pp. 597–610. Translated from Astronomicheskiĭ Zhurnal, Vol. 81, No. 7, 2004, pp. 658–672.
Original Russian Text Copyright © 2004 by Antipova, Boyarchuk, Pakhomov, Panchuk.

Analysis of Atmospheric Abundances in Classical Barium Stars

L. I. Antipova[1], **A. A. Boyarchuk**[1], **Yu. V. Pakhomov**[1], and **V. E. Panchuk**[2]

[1]*Institute of Astronomy, ul. Pyatnitskaya 48, Moscow, 119017 Russia*
[2]*Special Astrophysical Observatory, Russian Academy of Sciences, Nizhniĭ Arkhyz, Karachaĭ-Cherkessian Republic, 357147 Russia*

Received January 5, 2004; in final form, January 9, 2004

Abstract—We present our analysis of elemental abundances in the atmospheres of 16 classical barium stars derived from high-resolution spectra and model atmospheres. Comparison of the results with analogous data for moderate barium stars and normal red giants shows that the abundance patterns for elements before the iron peak are the same for all three groups of red giants, testifying to a similar origin. For binary systems, we confirm the influence of the orbital period and, hence, the component separation, on the overabundance of s-process elements. The amount of enrichment in s-process elements is also influenced by mass, metallicity, and evolutionary phase. Any of these parameters can be important in individual objects.

1. INTRODUCTION

In our previous investigations of the atmospheric elemental abundances of red giants, we determined and analyzed the abundances of seven classical barium stars [1]. However, due to the small number of stars studied, our plots illustrating certain relations were not convincing and required verification [1]. The current study is a continuation of [1], with the aim of studying the atmospheric elemental abundances of an additional nine classical barium stars using the same techniques, analyzing the new data together with those from [1], and carrying out a comparative analysis of the atmospheric chemical compositions of three groups of red giants—normal red giants (without spectral peculiarities), moderate barium stars, and classical barium stars. We obtained abundance data for the first two groups in our earlier papers [2, 3].

2. OBSERVATIONS AND REDUCTION

As in [1], our study of classical barium stars is based on observations acquired with the 6-m telescope of the Special Astrophysical Observatory (Russian Academy of Sciences). The NES echelle spectrometer at the Nasmyth focus of the telescope [4] provided a spectral resolution of $R = 60\,000$; the detector was a 2048×2048 CCD camera [5]. The list of classical barium stars studied is presented in Table 1. Their orbital periods were taken from [6–10].

The equivalent widths selected for our abundance determinations and the corresponding oscillator strengths are presented in Table 2.[1] We determined the atmospheric parameters (T_{eff}, $\log g$, V_t) using techniques developed by us previously [2]; the results are collected in Table 3.

We determined the elemental abundances using model atmospheres and the equivalent widths of selected lines. Our computations used the ATLAS9 code of Kurucz [11]. Table 4 presents the derived atmospheric elemental abundances for the program stars, which are related to the corresponding solar abundances by the formula

$$[X] = \log\left(\frac{\epsilon(el)}{\epsilon(\mathrm{H})}\right)_{*} - \log\left(\frac{\epsilon(el)}{\epsilon(\mathrm{H})}\right)_{\odot}.$$

Table 4 also indicates for each star the number of lines, N, used to determine a given element's abundance. Figure 1 shows the abundances of elements relative to iron, [X/Fe], for each of the program stars.

We can see in Fig. 1 that the atmospheric chemical compositions of all the stars are qualitatively similar. Three main intervals can be distinguished. The first consists of the light elements (Na, Mg, Al, Si), which have positive abundances relative to iron; i.e., these elements are more abundant than Fe. The second interval consists of the iron-peak elements.

---

[1] Table 2 is available only electronically through the Center of Astronomical Data in Strasbourg (ftp://cdsweb.u-strasbg.fr/pub/cats/J).

Table 1. Program barium stars and their atmospheric parameters

HD	Coordinates (2000.0)		m_v	Spectral type	T_{eff}, K	$\log g$	V_t, km/s
	α	δ					
16 458	$02^{\text{h}}\,47^{\text{m}}\,47.7^{\text{s}}$	$+81^\circ\,26'\,54''$	5.79^{m}	G8II Ba3	4560	1.73	1.53
88 562	10 12 29.9	−15 53 23	8.52	K2III Ba4	4274	1.74	1.49
101 013	11 37 53.0	+50 37 06	6.12	K0III Ba3	5080	3.10	1.40
130 386	14 48 02.3	−05 30 24	7.80	K0III Ba1	4720	2.41	1.44
139 409	15 38 41.4	−17 39 53	7.15	G5II Ba1	4731	2.13	1.47
175 190	18 55 07.1	−22 40 17	4.99	K3II Ba1	4188	1.36	1.50
178 717	19 09 22.0	+10 14 28	7.14	K4III Ba4	4073	0.01	1.81
183 915	19 31 25.5	+11 37 41	7.29	K1II Ba3	4616	1.88	1.56
196 673	20 37 44.3	+33 21 59	6.97	K0III Ba1	4905	2.38	1.53

The abundance ratios, [X/Fe], exhibit only a small amount of scatter, indicating that the relative abundances of these elements do not differ from those in the solar atmosphere, within the uncertainties in the chemical compositions. The third interval consists of elements heavier than the iron-peak elements, which are formed predominantly in the s and r processes; all the program stars display large abundance anomalies of these elements. We are especially interested in the s-process elements, whose abundances can change in the course of a star's evolution. The elements Mo, Sm, Eu, Dy, and Hf are mainly created in the r process, and we do not consider their abundances in this paper.

The overabundances of the various s-process elements for the program stars are fairly similar. The abundances of these elements for each star can be described by the average of the abundances of the individual elements:

$$[\text{s-el/Fe}] = \frac{[\text{SrI}] + [\text{ZrII}] + [\text{YII}] + [\text{CeII}] + [\text{LaII}] + [\text{NdII}] + [\text{PrII}]}{7} - [\text{Fe}].$$

These mean abundance estimates for each star are given in Table 3. We did not use the BaII lines, because they are very strong, and we expect non-LTE effects to have a significant impact on the derived abundances of this element. Table 3 shows that the scatter in the abundances about the mean value is not large and is comparable to the scatter for any given element from the individual lines used to derive its abundance.

3. LUMINOSITIES OF THE STARS

Our further analysis of the program stars requires estimates of their luminosities, which we derived from the apparent magnitudes and distances to the program stars. The data needed for this purpose are collected in Table 5. Columns 2, 5, 6, and 3 contain, respectively, the apparent magnitudes, $B{-}V$ and $U{-}B$ color indices (taken from [12–15]), and parallaxes (from the HIPPARCOS catalog [16]). The distances to the program stars do not exceed 400 pc.

We estimated the interstellar extinction from the stars' positions in the ($B{-}V$, $U{-}B$) two-color diagram (Fig. 2). When undistorted by interstellar reddening, a star's position in this diagram depends on its effective temperature, surface gravity, and metallicity. We analyzed each star individually. Using the set of normal color-index curves of [17], we selected those whose parameters had minimal deviations from the gravity and metallicity we had determined for the star. The observed position of each star in the ($B{-}V$, $U{-}B$) plane was reduced to its normal position (($B{-}V)_0$, ($U{-}B)_0$) on the normal color-index curve along the reddening line. We then used the difference between $(B{-}V)_0$ and

Table 3. Parameters of the barium stars

HD	Spectral type	$[Fe/H]$	[s-el/Fe]	P_{orb}, days	Data on the companion
Classical barium stars in binary systems					
16 458	K1IIBa3	-0.27 ± 0.09	1.32 ± 0.27	2018.0	
46 407	K0IIIBa3	-0.14 ± 0.08	1.39 ± 0.24	457.4	
77 247	G8IIIBa2	$+0.09 \pm 0.05$	0.54 ± 0.22	80.5	
88 562	K2IIIBa4	-0.16 ± 0.07	1.05 ± 0.23	1445.05	
101 013	K0IIIBa3	$+0.00 \pm 0.07$	1.23 ± 0.25	1710.9	
178 717	K4IIBa4	-0.31 ± 0.14	1.06 ± 0.26	2866.0	
196 673	K0IIIBa1	$+0.27 \pm 0.08$	0.13 ± 0.20	6500.0	visual binary [36]
199 394	G8IIBa1	$+0.02 \pm 0.12$	0.89 ± 0.27	4382.6	
199 939	K0IIIBa4	-0.34 ± 0.11	1.49 ± 0.34	584.9	
204 075	G4IIBa3	-0.04 ± 0.11	1.00 ± 0.47	2378.2	
205 011	G9IIIBa2	-0.03 ± 0.05	0.82 ± 0.21	2836.8	
Classical barium stars with no evidence of binarity					
65 854	G8IIIBa1	-0.20 ± 0.08	0.77 ± 0.25	–	
130 386	K0IIIBa1	$+0.01 \pm 0.07$	0.24 ± 0.31	–	
139 409	G5IIBa1	-0.51 ± 0.06	0.63 ± 0.31	–	
175 190	K3IIBa0.8	-0.13 ± 0.08	0.63 ± 0.32	–	
183 915	K1IIBa3	-0.43 ± 0.10	1.13 ± 0.32	–	
Moderate barium stars					
49 293	K0 + IIIaBa0.2	+0.08	0.21	1760.9	spectroscopic binary [32]
74 739	G7.5IIIaBa0.1	−0.21	0.29	–	visual binary [32]
83 618	K2.5IIIBa0.3	−0.06	0.29	–	
133 208	G8IIIaBa0.3	+0.07	0.21	–	
158 899	K3.5IIIBa0.1	+0.00	0.24	–	
176 411	K1-IIIBa0.2	−0.05	0.03	1270.6	
202 109	G8IIIBa0.6	−0.03	0.39	–	spectroscopic binary [32], white dwarf [33]
215 665	G8IIIaCN1Ba0.3	+0.09	0.21	–	

$(B{-}V)$ to determine the V-band extinction: $A_V = 3.2((B{-}V) - (B{-}V)_0)$.

The data from [17] were also used to determine bolometric corrections, BC_V, also using our gravity and metallicity estimates. We can thus find the star's luminosity:

$$\log\left(\frac{L_*}{L_\odot}\right) = 0.4(4.69 - (m_* + 5 + 5\log\pi_* + A_V + BC_V)).$$

The $(B{-}V)_0$ color index was used to estimate the effective temperatures of the stars. Recall that, as is noted in [2, 18], the atmospheric parameters we determined (T_{eff}, $\log g$) correspond to that part of the atmosphere best describing the observed line spectrum. They do not always coincide with the real effective temperatures derived from the continuum energy distribution or with the gravities computed from estimates of the star's mass. This is probably due to imperfections in the model atmospheres.

We used the $(B{-}V)_0$ values given in column 7 of Table 5 to determine the stars' temperatures applying

Table 4. Elemental abundances in the atmospheres of barium stars

	HD 16458		HD 88562		HD 101013		HD 130386		HD 139409		HD 175190		HD 178717		HD 183915		HD 196673	
	N	$[X]$	N	$[X]$	N	$[X]$	N	$[X]$	N	$[X]$	N	$[X]$	N	$[X]$	N	$[X]$	N	$[X]$
AlI	2	−0.02	–		1	0.10	–		–		–		–		–		–	
NaI	5	−0.02 ± 0.05	3	−0.12 ± 0.05	4	−0.01 ± 0.07	3	0.21 ± 0.05	1	−0.36	2	0.06 ± 0.06	2	0.60 ± 0.04	1	−0.31	2	0.47 ± 0.08
MgI	1	−0.02	–		1	−0.01	–		–		–		–		–		–	
SiI	8	−0.32 ± 0.08	4	−0.10 ± 0.03	7	0.01 ± 0.08	4	0.00 ± 0.05	5	−0.19 ± 0.05	9	0.16 ± 0.09	4	−0.34 ± 0.08	6	−0.25 ± 0.08	4	0.19 ± 0.06
KI	2	0.79 ± 0.04	2	0.33 ± 0.07	1	0.83	1	0.59	–	–	–	–	1	0.84	1	0.36	–	
CaI	7	−0.21 ± 0.09	2	−0.21 ± 0.06	6	0.00 ± 0.09	2	−0.03	4	−0.34 ± 0.09	2	−0.16 ± 0.22	2	−0.30 ± 0.07	3	−0.35 ± 0.06	2	0.32
ScI	6	−0.22 ± 0.02	3	−0.06 ± 0.09	4	0.02 ± 0.04	3	−0.02 ± 0.05	2	−0.51 ± 0.10	5	−0.42 ± 0.10	2	−0.12 ± 0.02	6	−0.49 ± 0.07	2	0.28 ± 0.05
ScII	5	−0.22 ± 0.08	5	−0.03 ± 0.06	4	0.12 ± 0.03	4	−0.02 ± 0.09	6	−0.24 ± 0.04	4	−0.14 ± 0.08	3	−0.64 ± 0.02	4	−0.39 ± 0.05	2	0.22 ± 0.01
TiI	24	−0.29 ± 0.09	14	−0.19 ± 0.06	37	0.05 ± 0.08	33	−0.08 ± 0.08	18	−0.42 ± 0.06	23	−0.16 ± 0.10	25	−0.01 ± 0.10	40	−0.50 ± 0.11	9	0.23 ± 0.08
TiII	6	−0.28 ± 0.08	6	−0.01 ± 0.08	7	0.25 ± 0.08	7	0.04 ± 0.10	7	−0.16 ± 0.05	4	−0.09 ± 0.08	8	−0.46 ± 0.11	7	−0.32 ± 0.11	3	0.26 ± 0.07
VI	10	−0.32 ± 0.05	6	−0.16 ± 0.08	10	0.01 ± 0.06	7	0.02 ± 0.04	11	−0.53 ± 0.05	9	−0.14 ± 0.07	4	−0.07 ± 0.15	12	−0.55 ± 0.08	7	0.16 ± 0.07
CrI	13	−0.39 ± 0.07	17	−0.36 ± 0.09	15	0.01 ± 0.08	18	−0.02 ± 0.09	6	−0.66 ± 0.10	19	−0.16 ± 0.09	12	−0.35 ± 0.10	14	−0.47 ± 0.17	4	0.14 ± 0.11
CrII	1	−0.10	–	–	5	0.09 ± 0.11	1	0.10	2	−0.53 ± 0.05	2	−0.15 ± 0.08	1	0.03	3	−0.32 ± 0.13	1	0.16
MnI	4	−0.60 ± 0.11	4	−0.36 ± 0.14	4	−0.31 ± 0.09	3	0.05 ± 0.15	5	−0.66 ± 0.07	5	−0.21 ± 0.13	2	−0.51 ± 0.17	3	−0.72 ± 0.12	3	0.14 ± 0.21
FeI	76	−0.27 ± 0.09	42	−0.16 ± 0.07	95	0.00 ± 0.07	83	0.01 ± 0.07	49	−0.51 ± 0.06	60	−0.13 ± 0.08	64	−0.31 ± 0.14	93	−0.42 ± 0.10	25	0.27 ± 0.08
FeII	5	−0.34 ± 0.08	5	−0.17 ± 0.09	9	−0.02 ± 0.04	11	−0.02 ± 0.08	4	−0.47 ± 0.04	5	−0.15 ± 0.07	5	−0.30 ± 0.09	9	−0.46 ± 0.07	4	0.22 ± 0.08
CoI	5	−0.13 ± 0.12	8	0.02 ± 0.07	14	0.06 ± 0.10	7	0.09 ± 0.09	5	−0.31 ± 0.06	12	0.05 ± 0.10	7	−0.15 ± 0.11	12	−0.40 ± 0.07	3	0.25 ± 0.11
NiI	22	−0.42 ± 0.08	14	−0.24 ± 0.07	43	−0.07 ± 0.09	33	−0.03 ± 0.08	24	−0.49 ± 0.07	26	−0.13 ± 0.09	18	−0.59 ± 0.15	37	−0.46 ± 0.12	13	0.15 ± 0.05
CuI	2	1.12 ± 0.74	1	0.72	3	1.66 ± 0.08	1	0.98	2	1.11 ± 0.05	1	0.83	1	0.63	–	–	2	1.69 ± 0.04
ZnI	1	−0.61	–	–	1	−0.15	1	−0.15	1	−0.31	1	−0.32	1	−0.65	1	−0.59	1	0.20
SrI	1	0.93	1	0.74	2	1.10 ± 0.01	1	0.55	–	–	1	0.70	1	1.24	1	0.64	–	
YI	2	0.55 ± 0.08	1	−0.54	–	–	1	1.01	–	–	1	0.58	1	0.84	1	−0.69	–	
YII	6	0.74 ± 0.08	5	0.69 ± 0.04	6	1.14 ± 0.09	5	0.60 ± 0.10	6	0.18 ± 0.10	5	0.71 ± 0.11	3	0.64 ± 0.06	4	0.44 ± 0.01	5	0.31 ± 0.06
ZrI	12	0.43 ± 0.13	8	0.35 ± 0.11	11	0.77 ± 0.09	8	0.14 ± 0.08	4	−0.20 ± 0.08	8	0.27 ± 0.04	3	0.76 ± 0.18	9	−0.05 ± 0.21	1	0.04
ZrII	3	0.99 ± 0.06	2	0.92 ± 0.01	5	1.36 ± 0.10	2	0.56 ± 0.06	2	0.32 ± 0.03	3	0.83 ± 0.07	2	0.83 ± 0.06	3	0.81 ± 0.14	–	
MoI	5	0.51 ± 0.09	3	0.27 ± 0.03	4	0.82 ± 0.08	2	0.22 ± 0.04	2	−0.33 ± 0.01	5	0.29 ± 0.16	4	0.60 ± 0.18	4	0.13 ± 0.06	–	
RuI	5	0.78 ± 0.14	4	0.63 ± 0.19	3	1.47 ± 0.12	2	1.29 ± 0.01	–	–	3	0.58 ± 0.33	3	0.96	3	0.75 ± 0.22	–	
CdI	1	0.63	–	–	–	–	–	–	–	–	–	–	–	–	–	–	–	
BaII	1	1.21	1	0.90	1	1.37	1	0.51	2	0.19 ± 0.01	2	0.51 ± 0.09	1	0.92	1	0.68	1	0.78
LaII	4	1.25 ± 0.11	4	0.99 ± 0.10	5	1.23 ± 0.06	4	0.19 ± 0.04	2	0.16 ± 0.21	3	0.55 ± 0.07	2	0.63 ± 0.03	3	0.71 ± 0.04	4	0.40 ± 0.05
CeII	11	1.09 ± 0.07	9	0.83 ± 0.11	14	1.26 ± 0.10	5	0.02 ± 0.11	2	−0.16 ± 0.09	12	0.30 ± 0.09	7	0.66 ± 0.12	12	0.77 ± 0.14	3	0.23 ± 0.11
PrII	8	1.07 ± 0.09	5	0.97 ± 0.09	7	1.14 ± 0.11	3	−0.06 ± 0.06	–	–	6	0.26 ± 0.11	5	0.89 ± 0.07	11	0.74 ± 0.15	2	0.41 ± 0.07
NdII	31	1.17 ± 0.11	13	0.94 ± 0.10	28	1.24 ± 0.12	7	0.21 ± 0.06	9	0.24 ± 0.06	21	0.32 ± 0.10	11	0.83 ± 0.17	26	0.79 ± 0.15	2	0.63 ± 0.01
SmII	5	0.50 ± 0.05	1	0.72	3	1.03 ± 0.27	2	0.14 ± 0.02	–	–	2	0.05 ± 0.12	3	0.03 ± 0.34	2	0.12 ± 0.01	2	0.88 ± 0.07
EuII	1	0.55	1	0.50	1	0.40	–	–	–	–	2	0.11	–	–	1	0.14	–	
GdII	–	–	–	–	–	–	–	–	–	–	–	–	–	–	1	−0.13	–	
DyII	1	0.72	1	0.67	1	1.10	1	1.18	–	–	1	0.62	1	0.33	1	0.47	–	
HfI	1	0.93	1	0.51	–	–	1	0.53	–	–	1	0.08	1	0.74	1	0.45	–	
WI	1	0.52	–	–	–	–	–	–	–	–	–	–	1	0.49	1	0.14	–	

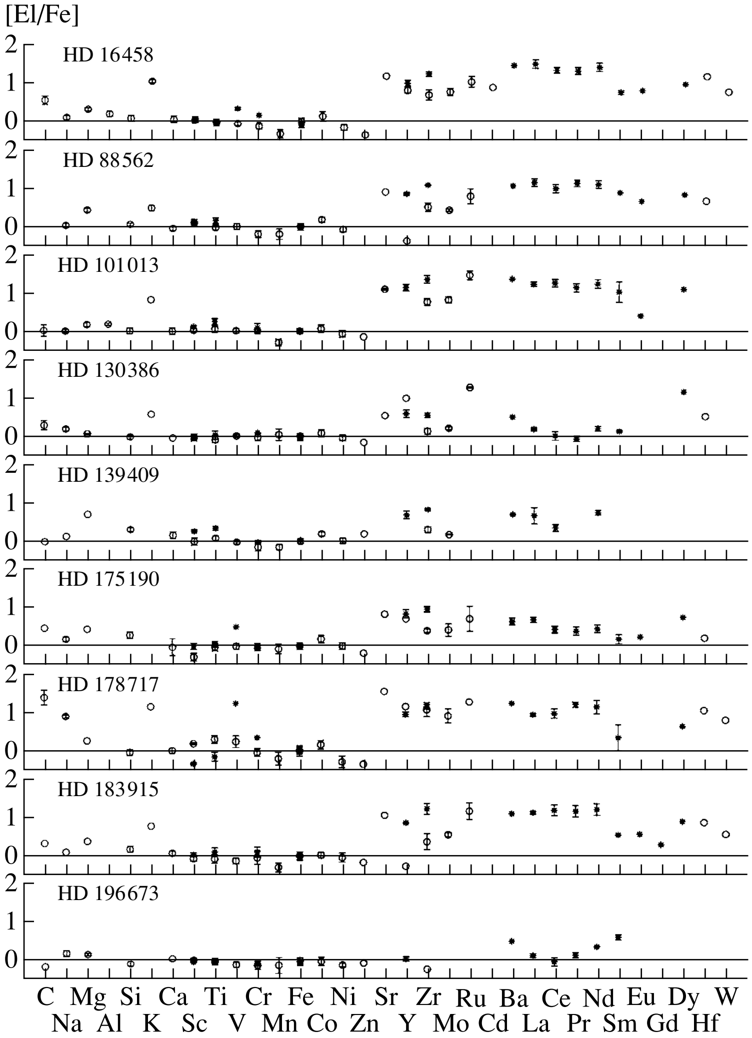

Fig. 1. Elemental abundances of the studied barium stars relative to those in the solar atmosphere. The circles show abundances determined from lines of neutral atoms, and asterisks, abundances derived from lines of ions. Each abundance is accompanied by an error bar derived from the dispersion of the individual lines. The absence of a bar means that the abundance was determined from a single line.

the calibration we derived using the data from [17] and taking into account the gravities and metallicities. The resulting temperatures are presented in column 12 of Table 5. These values were subsequently used to analyze the stars' positions in the $\log T - \log(L_*/L_\odot)$ diagrams. The masses (given in Table 3) were estimated using evolutionary tracks from [19, 20]. We determined the mass of each star using the tracks for the corresponding metallicity.

The $\log g$ values given in column 13 of Table 4 were calculated using the formula

$$\log g = -10.607 + \log\left(\frac{M_*}{M_\odot}\right)$$
$$+4 * \log T_{eff} - \log\left(\frac{L_*}{L_\odot}\right).$$

4. ANALYSIS AND DISCUSSION

As is noted in [1], evolution in a binary system remains the main hypothesis explaining the appearance of the barium-star phenomenon on the giant branch. However, binarity can be established for far from all classical barium stars [21]. With this in mind, we will subdivide all our program stars (those from this paper and from [1]) into two groups: binaries and stars for which no evidence of binarity has been detected.

Our papers on the atmospheric chemical compositions of red giants (normal giants and moderate barium stars) indicate the presence of overabundances of Na, Al, and Si, which are correlated with the star's luminosity [2, 3]. The classical barium stars are no exception [1].

We will analyze the abundance determinations presented here and in [1] and compare them to similar

Table 5. Luminosities and masses of the program stars

HD	m_v	π, mas (Hip)	r, pc (Hip)	$B-V$	$U-B$	$(B-V)_0$	A_v	BC	M_{bol}	$\log\left(\frac{L_*}{L_\odot}\right)$	T_{B-V}, K	$\log g$	$\frac{M_*}{M_\odot}$
1	2	3	4	5	6	7	8	9	10	11	12	13	14
16 458	5.790	6.54	152	+1.332	+1.29	+1.258	0.24	−0.64	−1.01	2.278	4351	1.95	1.9
46 407	6.266	8.25	121	+1.123	+0.710	+0.915	0.67	−0.25	−0.07	1.904	5077	2.78	2.9
65 854	8.41	6.34	157	+0.976	+0.604	+0.927	0.16	−0.27	2.00	1.077	5006	3.32	1.6
77 247	6.860	2.86	349	+1.001	+0.657	+0.918	0.27	−0.24	−1.36	2.420	5124	2.39	3.8
88 562	8.52	3.13	319	+1.451	+1.484	+1.322	0.41	−0.80	−0.21	1.960	4166	1.91	1.0
101 013	6.124	7.07	141	+1.071	+0.730	+0.944	0.41	−0.26	−0.30	1.995	5019	2.69	3.1
130 386	7.80	3.42	292	+1.105	+0.907	+1.065	0.13	−0.34	0.01	1.874	4827	2.65	2.5
139 409	7.15	5.51	181	+1.078	+0.734	+1.017	0.20	−0.34	0.33	1.746	4820	2.66	1.9
175 190	4.99	12.07	82	+1.345	+1.478	+1.345	0.00	−0.75	−0.36	2.018	4223	1.96	1.2
178 717	7.14	2.90	344	+1.918	+2.025	+1.450	1.50	−0.81	−2.85	3.016	4177	1.41	3.5
183 915	7.29	3.48	287	+1.363	+1.083	+1.102	0.84	−0.38	−1.22	2.363	4768	2.25	3.2
196 673	6.97	2.76	362	+1.143	+0.928	+1.060	0.27	−0.33	−1.42	2.443	4842	2.28	3.9
199 394	6.999	6.33	157	+1.022	+0.635	+0.894	0.41	−0.24	0.36	1.733	5133	2.93	2.7
199 939	7.424	3.16	316	+1.293	+0.995	+1.083	0.67	−0.37	−1.12	2.323	4746	2.27	3.1
204 075	3.754	8.19	122	+0.986	+0.596	+0.868	0.38	−0.21	−2.27	2.784	5209	2.14	4.6
205 011	6.426	6.31	158	+1.079	+0.774	+0.982	0.31	−0.27	−0.16	1.939	4980	2.70	2.9

results obtained for normal red giants and moderate barium stars [2, 3].

All our program stars are field giants and cover a fairly wide metallicity range ($-0.51 <$ [Fe/H] $< +0.27$). Thus, in addition to the abundance anomalies for some elements that are characteristic of red giants (i.e., due to pronounced convection and the dredge-up to surface layers of the products of nuclear burning during the main-sequence stage), we expect that some of the observed overabundances could be due to the chemical evolution of the Universe, i.e., to the ages of the program stars. These effects can overlap, and to help elucidate to what extent the observed anomalies are a result of evolutionary processes in the star, we compared the abundance of a given element in the red giants to the corresponding abundance for dwarf stars of the same metallicity (i.e., of the same age), whose chemical compositions reflect that of the material from which the stars were formed. We used [22] as the source of data on the elemental abundances of dwarfs.

4.1. Sodium

Figure 3 displays the sodium abundances relative to iron ([Na/Fe]) for the program stars as a function of the iron abundance, [Fe/H], and gravity, $\log g$ (Figs. 3a, 3b).

The analysis of the atmospheric abundances of about 200 Galactic-disk F and G dwarfs with metallicities $-0.8 <$ [Fe/H] $< +0.2$ carried out in [22] shows these dwarfs do not display any of the Na abundance anomalies that are characteristic of the Galaxy's chemical evolution (e.g., the relation between [Na/Fe] and [Fe/H] in Fig. 9 in [22]); on average, the [Na/Fe] values are close to zero, with a small scatter. Comparing this diagram with the corresponding diagram for the giants (Fig. 3a), we see that the [Na/Fe] values for the studied giants likewise do not show appreciable abundance variations with [Fe/H], but the abundances are systematically higher than those for the dwarfs (on average, by 0.2 dex). The scatter about the mean is also much larger than for the dwarfs (we discuss the reasons for this scatter below). It is known (see, for example, [23–25]) that the observed Na excesses in the atmospheres of red giants are determined by evolutionary processes in these stars: the dredge-up of products of nuclear burning in the stellar interior during the main-sequence stage to its surface by convection that develops during the red-giant stage.

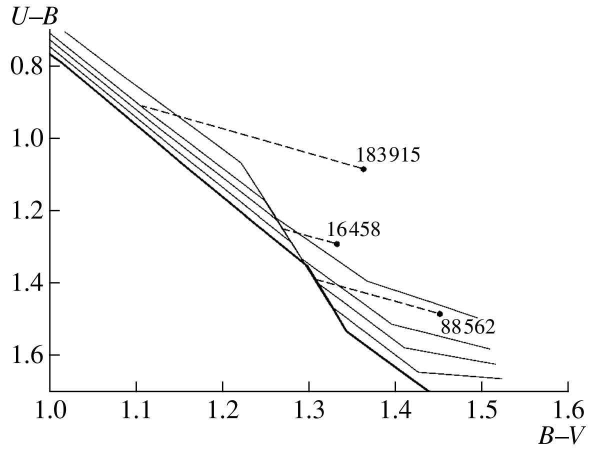

Fig. 2. Example of determining $(B-V)_0$ using the two-color diagram. The unreddened color curves are shown for $\log g = 1.5$ and [Fe/H] = 0 (thick curve) and then for [Fe/H] = −0.1, −0.2, −0.3, −0.5 (thin curves).

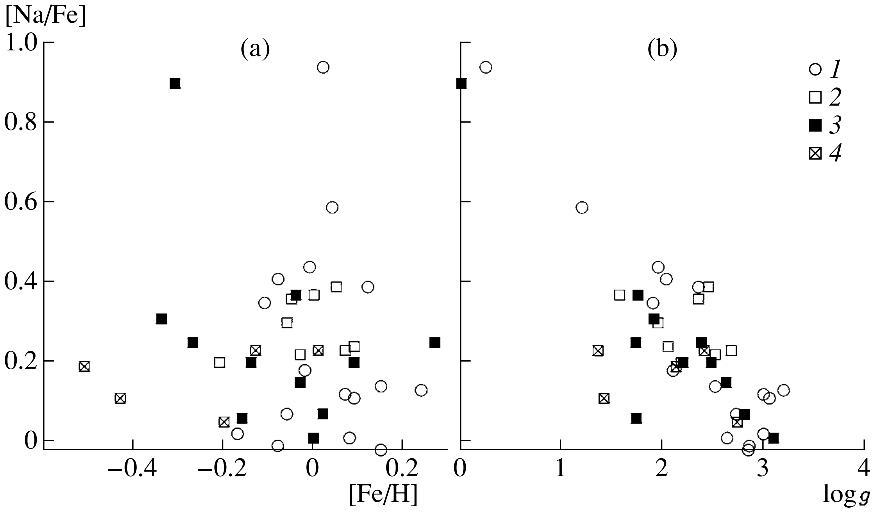

Fig. 3. Excess of the ratio of the sodium and the iron abundances, compared to the analogous ratio for the Sun for (*1*) normal giants and supergiants, (*2*) moderate barium stars, (*3*, this paper) classical barium stars in binary systems, and (*4*, this paper) classical barium stars with no evidence for binarity.

Figure 3a also shows that, on average, the moderate barium stars lie somewhat above the normal giants.

As was noted above, the scatter in Fig. 3a (for giants) is much larger than in the analogous diagram for dwarfs (Fig. 9 from [22]). This scatter exceeds the observational uncertainties. We can see from Fig. 3a and Table 3 that, for the same [Fe/H], stars that are located higher have lower gravity, i.e., higher luminosity. This suggests that the scatter is determined by the luminosity range occupied by the studied stars. In addition, on average, the moderate barium stars have higher luminosities than normal red giants, i.e., they are more evolved. This conclusion agrees with that made in [3] based on an analysis of the atmospheric abundances of s-process elements in moderate barium stars. The range of gravities covered by the dwarfs is much narrower than for the giants, giving rise to the smaller scatter in Fig. 9 in [22].

Figure 3b shows the relation between the Na excess and gravity, $\log g$, well known for supergiants and giants (see, for instance, Fig. 3 in [1]), with the data for the newly studied classical barium stars added. It is clear that the position occupied by the moderate barium stars is intermediate between those occupied by the giants and supergiants, confirming that they have somewhat higher luminosities compared to normal giants and are, hence, more evolved. Note that the moderate barium stars and normal red giants satisfy the same relation in this diagram.

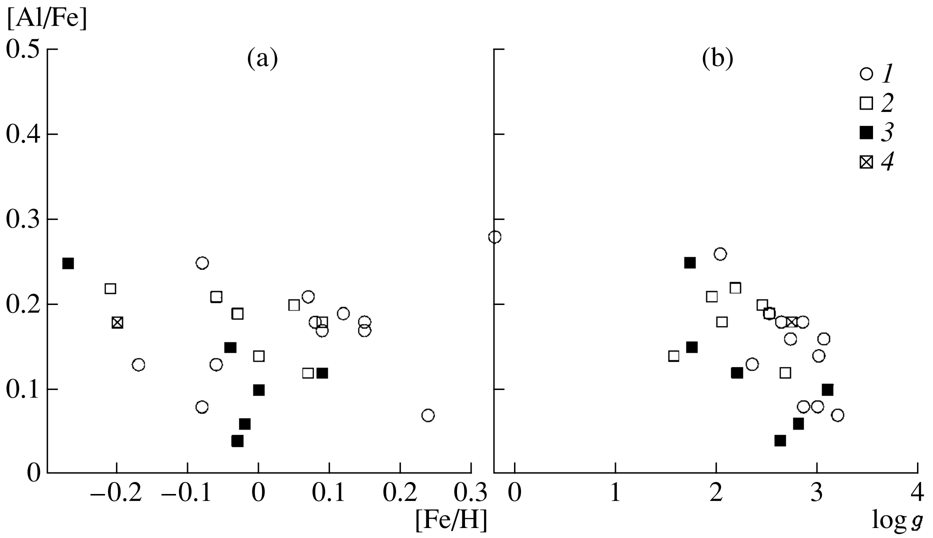

Fig. 4. Excess of the ratio of the aluminum and iron abundances in the atmospheres of red giants compared to the analogous ratio for the Sun. The meaning of the symbols is the same as in Fig. 3.

4.2. Aluminum

Unfortunately, due to the limited spectral range studied, we were able to measure the Al abundances for only seven classical barium stars (Table 4). Nevertheless, it is interesting to compare the results with data for other groups of red giants and dwarfs.

According to Fig 9 in [22], the [Al/Fe] ratios are virtually constant and equal to 0.05–0.1 dex for dwarfs with the metallicities of our program stars. We noted earlier [2, 3] the existence of a slight [Al/Fe] excess in the atmospheres of field red giants, which is correlated with luminosity (i.e., the excess increases with decreasing $\log g$), similar to the situation with Na. We suggested that aluminum is produced in the MgAl cycle during the main-sequence stage and that the nuclear products are dredged-up to the stellar surface by convection developing during the red-giant stage.

Figure 4, whose structure is analogous to that of Fig. 3, displays estimates of [Al/Fe] for the atmospheres of the studied stars. Figure 4a shows that [Al/Fe] does not vary with metallicity. As in the case of Na, the large scatter in the diagram exceeds the observational errors and depends on the star's gravity (compare Table 4 and Fig. 4a). The mean of this ratio is about 0.2 dex, somewhat higher than for the dwarfs. Together with the fact that the Al overabundances increase with decreasing $\log g$ (Fig. 4b), this provides evidence of the correctness of the earlier conclusion about the origin of the Al excesses in field red giants. Note that red giants of all three groups satisfy the same relation.

4.3. Magnesium

Magnesium is one of the even elements, whose formation is usually associated with helium burning during type II supernova outbursts. This type of supernova was more common in the early stages of the Galaxy's evolution, and overabundances of even elements, including Mg, are characteristic of the atmospheres of old (low-metallicity) stars. The younger stars making up the majority of the Galactic-disk population do not display overabundances of even elements. Returning to Fig. 9 in [22], we see that the Mg abundances in dwarfs with metallicities in the range of interest are virtually constant and close to zero; we can see only a slight increase of [Mg/Fe] at metallicities $[Fe/H] > -0.4$. Reddy *et al.* [22] suggest that this is due to the contribution of Population II stars in this region.

Along with aluminum, magnesium participates in the MgAl cycle for hydrogen burning in stellar cores, and it is of interest to analyze the atmospheric abundance of this element for our program stars, as was done above for Na and Al (Fig. 5). Unfortunately, we were able to estimate Mg abundances for only a few of the classical barium stars due to the limited spectral range observed. For this reason, our abundance plots for Mg analogous to those for the elements discussed above are less trustworthy, and our conclusions concerning the Mg abundances in the red giants should be considered preliminary and requiring verification. In particular, it appears that the overabundance of Mg exhibits a dependence on gravity similar to that for the elements discussed above (Figs. 3b, 4b). This means that some Mg is present in the stellar interiors,

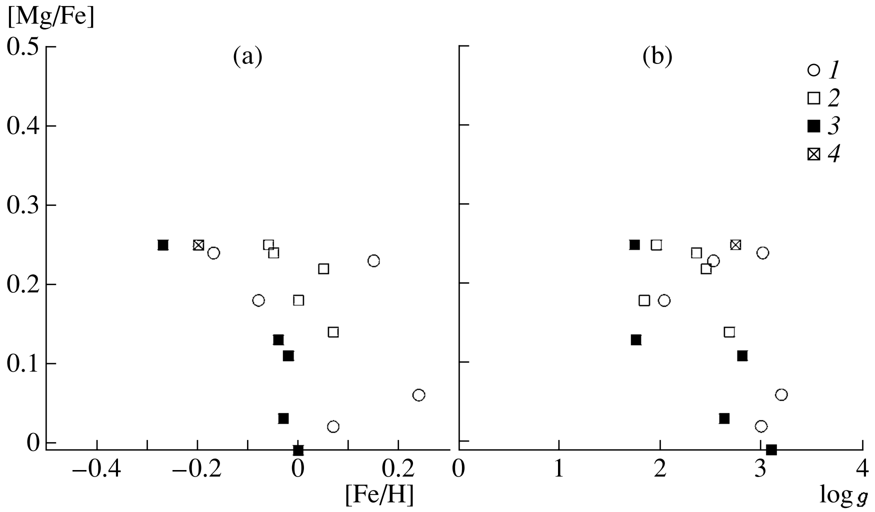

Fig. 5. Excess of the ratio of the magnesium and iron abundances in the atmospheres of red giants compared to the analogous ratio for the Sun. The meaning of the symbols is the same as in Fig. 3.

in excess of its abundance in the material from which the star was formed. (In fact, the Mg overabundances are higher than those in dwarfs; see Fig. 9 in [22].) Due to convection, this magnesium is dredged up to the star's surface during the red giant stage.

Three stable isotopes of Mg are known, whose abundances have the ratios ^{24}Mg : ^{25}Mg : ^{26}Mg = 79 : 10 : 11, which are the same on the Earth and the Sun. It is also known that the neutron-rich isotopes ^{25}Mg and ^{26}Mg can be burned in stellar interiors via the capture of a proton, forming ^{27}Al (the MgAl cycle). This is precisely how many investigators have explained the anticorrelation between the abundances of Mg and Al for stars in globular clusters. However, the abundance of Mg is mainly determined by its most abundant isotope, ^{24}Mg. Thus, to explain the fairly large Mg overabundances observed in a number of globular clusters (up to 0.6 dex), it is necessary to consider mechanisms producing specifically the isotope ^{24}Mg. Note that disk red giants also display Mg excesses of up to 0.3 dex.

The theoretical papers [27, 28], which consider the abundances of isotopes of elements from C to Al in the hydrogen-burning regions of stars during the red-giant stage (from the star's entry to this stage to the tip of the giant branch, when helium begins to burn), are of interest in this respect. These studies take into account a large number of nuclear reactions, including proton-capture reactions (the CNO, NeNa, and MgAl cycles for hydrogen burning). The computations cover a wide range of metallicities and make use of modern data on reaction rates. It was demonstrated that the Al abundance first increases due to proton capture by nuclei of ^{25}Mg and ^{26}Mg, then by nuclei of ^{24}Mg in the MgAl cycle. The use of a refined rate for the reaction $^{23}\mathrm{Na}(p,\gamma)^{24}\mathrm{Mg}$, representing leakage from the NeNa cycle, increased the Mg abundance by an amount that was larger than the decrease via the transformation of Mg into ^{27}Al in the MgAl cycle. In addition, the lower a star's metallicity, the higher the activity of the above nuclear reactions. This is probably the reason that the observed anomalies are lower for field than for globular-cluster red giants. In addition, according to [27, 28], the observed abundance anomalies depend on several additional parameters, such as the temperature, burning time, thickness of envelopes, etc.; this means, for example, that either an anticorrelation or a correlation can be observed between the Mg and Al abundances under various conditions, providing a possible explanation for the diversity of these elements' behavior in stars of different globular clusters. At any rate, this process is determined by several parameters, and it is clear that this increases the scatter about any of the analyzed relations, as is also clear from a comparison of Figs. 4 and 5 with Fig. 3. According to [27, 28], the yield of Na does not depend on the metallicity, in contrast to the other elements considered.

4.4. Silicon

Silicon is another even element, so that everything we said above concerning the origin of Mg and its abundance in old stars is also fully valid for Si. Earlier, in our analysis of the spectra of red giants (normal giants and moderate barium stars), we noted that they displayed slight anomalies in their Si abundances [2, 3]. Note, however, that these giants are Galactic-disk stars and their metallicities are close to the solar value, so that they are not old stars whose Si excesses can be considered "normal."

We revisit this question here using a larger amount of data (see Figs. 6a and 6b, analogous to the corresponding figures for the considered elements above). Figure 6a shows that the mean [Si/Fe] level remains unchanged when the metallicity, [Fe/H], is varied and stays approximately +0.15 dex above the corresponding [Si/Fe] abundances for Galactic-disk dwarfs [22]. As in previous cases, this suggests that the Si overabundances were produced in the stellar interiors and dredged up by convection. This is supported by the relation between [Si/Fe] and the gravity, $\log g$ (Fig. 6b): the lower $\log g$ (the higher the star's luminosity), the stronger the convection that develops and the deeper the stellar layers to which it can penetrate. We suggested in [2] that the Si abundance anomalies could be due to the leakage reaction from the MgAl cycle, $^{27}\mathrm{Al}(p,\gamma)^{28}\mathrm{Si}$. In light of the conclusions of [27, 28], we expect that, since the leakage reaction from the NeNa cycle, $^{23}\mathrm{Na}(p,\gamma)^{24}\mathrm{Mg}$, increases the number of atoms involved in the MgAl cycle, the number of atoms leaving the MgAl cycle can also increase, i.e., the abundance of Si can grow.

The above conclusions are valid for normal giants and supergiants, as well as for moderate barium stars and stars classified as classical barium stars but for which evidence of binarity has not been detected (Figs. 6a, 6b). Classical barium stars with known orbital periods have lower Si excesses and do not satisfy the dependence on $\log g$. The reason for this is not understood. At present, we can only suppose that classical binary barium stars and stars whose binarity has not been established may have different origins.

We have thus analyzed the data we obtained on the Na, Al, Mg, and Si abundances in the atmospheres of red giants in the Galactic disk, which represent three groups of stars displaying different abundance anomalies: normal giants, moderate barium stars, and classical barium stars. The following conclusions can be drawn based on Figs. 3–6.

—In the metallicity range considered, no correction to the abundances of the analyzed elements to reflect the chemical evolution of the Galaxy is needed.

—The ratio of the abundance of each of the analyzed elements to that of iron, [El/Fe], is systematically higher than for Galactic-disk dwarfs [26]. The observed overabundances are produced in the stellar interiors during hydrogen burning in the NeNa and MgAl cycles, with subsequent dredge-up to the stellar surface by convection in the red-giant stage.

—The anomalies of each of the analyzed elements are correlated with the luminosity, with the relation for each element being the same for all the considered groups of stars. This provides evidence that the origins of the Na, Al, Mg, and Si overabundances is the same for both the normal red giants and the moderate and classical barium stars (with the exception of the Si abundances for binary classical barium stars, whose behavior requires further study).

4.5. s-Process Elements

Barium stars are characterized by large anomalies of the abundances of s-process elements (Table 3). In to the binary hypothesis, the overabundance of s-process elements should decrease with increasing orbital period, i.e., with increasing size of the binary system. Indeed, such a dependence was found earlier [29], and our results (Fig. 7) confirm it. The scatter of the data in Fig. 7 is due to the range of metallicities of the program stars.

In the studied stars, these anomalies in the abundances of the s-process elements (relative to Fe) are within 0.5 to 1.5 dex in the classical barium stars (with the exception of HD 196 673 and HD 130 386; see below for possible reasons for these deviations) and do not exceed 0.3 dex for the moderate barium stars and normal red giants (with the exception of HD 202 109, also discussed below). In the interest of the uniformity of our analysis for all the elements, we first plotted the mean (averaged over all s-process elements, Table 3) ratio of the abundances of s-process elements and Fe ([s-el/Fe]) for each star as a function of [Fe/H] (Fig. 8). Figure 8 shows that, on average, [s-el/Fe] is about 0.2 dex for the normal red giants and moderate barium stars, whereas the classical barium stars exhibit a rapid increase of the s-element abundance with decreasing metallicity. An analogous plot for Galactic-disk dwarfs [22; Fig. 11] demonstrates essentially the same behavior for all the s-process elements: in the metallicity range under consideration, [s-el/Fe] is nearly equal to zero. This means that no correction to the observed abundances of s-process elements in the studied stars for the chemical evolution of the Galaxy is needed.

As we noted above, the anomalous abundances of s-process elements increase with decreasing metallicity. According to the binary-star hypothesis for barium stars, toward the end of the system's evolution, one of the binary components ejects an envelope enriched in s-process elements produced during the asymptotic giant-branch (AGB) stage; some of the matter from this envelope falls onto the companion and is then partially or fully mixed with its atmosphere, so that it becomes the barium star we observe now. Theoretical studies of the production of s-process elements during the AGB stage, such as [30], indicate that s-process elements are more easily

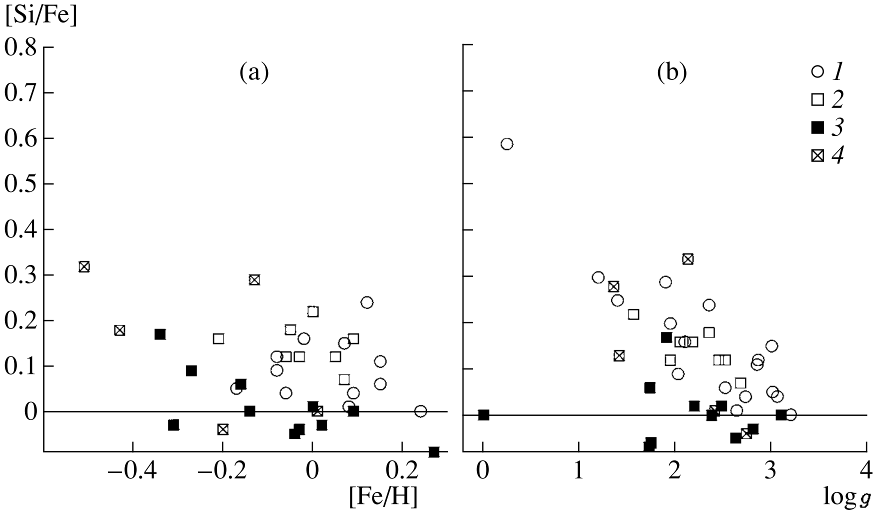

Fig. 6. Excess of the ratio of the silicon and iron abundances in the atmospheres of red giants compared to the analogous ratio for the Sun. The meaning of the symbols is the same as in Fig. 3.

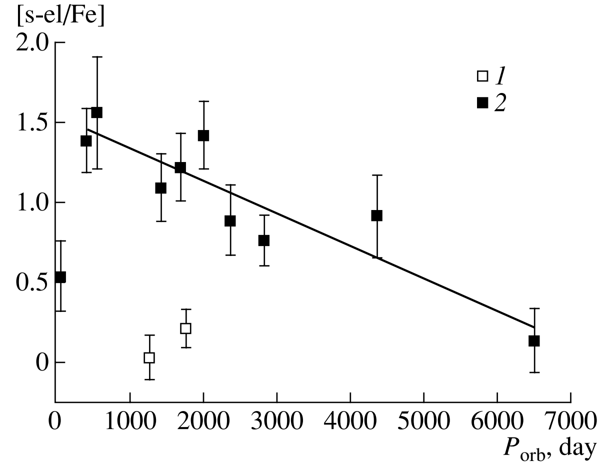

Fig. 7. Relation between the overabundance of s-process elements and orbital period in binary systems for (*1*) moderate barium stars and (*2*) classical barium stars.

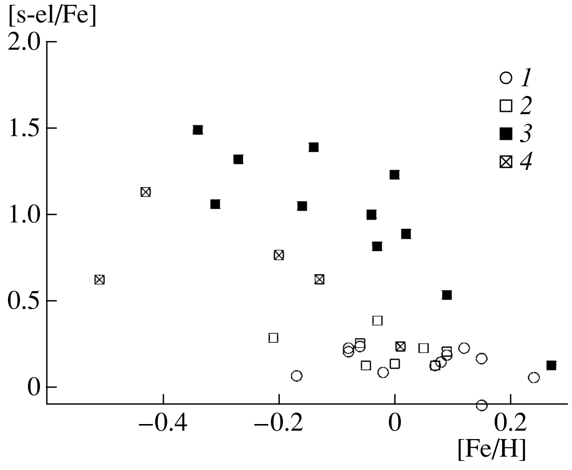

Fig. 8. Relation between the overabundance of s-process elements and metallicity. Notation is the same as in Fig. 3.

produced in metal-poor stars. This is precisely the phenomenon reflected by Fig. 8.

In [2, 3], we estimated the elemental abundances in the atmospheres of eight moderate barium stars. We now reexamine the results as part of our comparative analysis of normal red giants and moderate and classical barium stars. We can clearly see from Fig. 8 that the moderate barium stars show no obvious relation to the sequence of classical barium stars; the area they occupy in the diagram coincides completely with the region occupied by the normal red giants. This indicates that binarity of these stars, if established, is not the origin of the observed overabundances of the s-process elements, as is the case for classical barium stars.

There is, however, evidence for binarity for about half of the analyzed moderate barium stars (Table 3). Let us consider this evidence in more detail. In the case of HD 176411, it was possible to determine its orbital period, $P = 1270.6$ days [31], which is typical of the periods of classical barium stars. The estimate of the companion's mass, $\approx 0.5 M_\odot$ [31], is also the correct value for the mass of the companion (white dwarf) of a classical barium star. However, it is currently generally accepted that the overabundance of s-process elements depends on the system's orbital period and, if the companion were a white dwarf, we would have expected, in accordance with [29] or Fig. 8 of this paper, an excess of s-process elements in the atmosphere of this barium star of about 1.0 dex, and it would have been classified as a classical barium star. Since this is not observed, Boffin *et al.* [31] concluded that the companion was an ordinary low-mass star evolving more slowly than the star that we observe as the moderate barium star.

According to [32], HD 74 739 is a member of a binary system whose second, visible, member is an A3V star that is not capable of "contaminating" its neighbor's atmosphere with s-process elements. HD 49 293 is a spectroscopic binary with an orbital period of $P = 1760.9$ days [31]. Unfortunately, nothing is known about its companion, but, since this orbital period is typical of the periods of classical barium stars and the abundance of s-process elements is not high (it should exceed the normal abundance by an order of magnitude), we conclude, as we did for HD 176411, that the companion is not a white dwarf but instead an ordinary low-mass star that is not capable of adding s-process elements to its companion's atmosphere.

Binarity has not been established for the four other objects in the group of moderate barium stars, and they are probably single. For only one of the moderate barium stars, HD 202 109, is the companion a white dwarf [33]. It is interesting that this particular star has the highest abundance of s-process elements among all the moderate barium stars considered here. Thus, for this star only, the origin of the overabundance of s-process elements could be its binarity, and the relatively low values of the overabundance compared to the values for classical barium stars could be a consequence of the star's long orbital period, which has not been determined thus far. We conclude that, with the exception of HD 202109, the origin of the s-process abundance anomalies in the atmospheres of the moderate barium stars is not associated with binarity.

This group of stars should probably include HD 196 673, which is listed here among the classical barium stars. This is a well-known visual binary (ADS 14 078) consisting of two giants: a barium K0III star (component A) and its G5III companion (component B), which is one magnitude fainter. The components are separated by about 3″. This system was classified as a barium star in 1962 [34], based on the observation of abnormally strong SrII and BaII lines and CN bands. Subsequent spectroscopic studies confirmed the presence of an overabundance of heavy elements [35]. The star is currently classified as K0IIIBa1, so we included it into the group of classical barium stars. A search for the orbital period based on an analysis of data on the component separation accumulated over one hundred years [7] did not lead to conclusive proof that the components formed a physical pair. Analysis of radial velocities acquired at the Dominion Astrophysical Observatory and the corresponding monitoring results from the CORAVEL spectrometer yielded a 6500-day period in the radial-velocity variations [8], making HD 196673 one of the widest binary systems containing barium stars. Note that we found no large anomalies in the abundances of the s-process elements. There is no evidence for the presence of a white dwarf in the system. In Fig. 8, the star lies in the area occupied by the normal giants and moderate barium stars. Thus, the existing data suggest it should be included in the group of moderate barium stars.

For HD 130 386, which is classified as K0IIIBa1, there are likewise no data demonstrating the existence of an orbital period. This star also displays a moderate abundance of s-process elements, and it lies in Fig. 8 in the area occupied by normal giants and moderate barium stars. Accordingly, we should probably also include it among the moderate barium stars.

We concluded earlier [3] that moderate barium stars are normal red giants at a somewhat more advanced evolutionary stage. This was based on the relations we established between the abundance anomalies for s-process elements for both moderate barium stars and normal red giants and the stars' masses and evolutionary phase, as well as the fact that the moderate barium stars have somewhat higher luminosities than the normal red giants. Our analysis of Fig. 8 supports this conclusion.

As we noted above, the area in Fig. 8 occupied by the classical barium stars lies considerably above that occupied by the normal giants and moderate barium stars. In addition, the enrichment of the barium-star atmospheres in s-process elements increases with decreasing metallicity, as is predicted by the theory. For a fixed metallicity, the scatter in the abundances of the s-process elements is large and depends on the orbital period (Table 3).

We subdivided the stars classified as classical barium ones into two groups: stars with known orbital periods and those for which orbital periods have not been established. Note that, with the exception of HD 183 915, the second group contains stars with low barium levels (Table 1).

The group of stars classified as classical barium stars but without orbital periods deserves a special discussion. Such stars lie below the classical barium stars in Fig. 8, although they repeat the latter group's trend with metallicity (an exception is HD 139 409, considered below). As we noted above, the scatter in this figure is determined by the orbital period, and the excess of s-process elements decreases with increasing period; we can therefore assume that these stars are wide pairs, making it difficult to determine their periods (as was noted above for HD 196 673).

We cannot rule out the possibility that this group should also include HD 202 109, which is classified as a moderate barium star and for which observations in the ultraviolet indicate the presence of a white-dwarf companion. The star is known to be a spectroscopic binary, but its period has not been determined. Thus, this star is also a probable wide pair. HD 139 409, mentioned above, has a much lower abundance of s-process elements and does not fit the general relation for the classical barium stars without orbital-period information. Keeping in mind that this star has the lowest metallicity among the analyzed stars and that, according to theoretical considerations, the production of s-process elements in stellar interiors is facilitated by conditions of lower metallicity, we suggest that this star may be single and more evolved, as was the case for the normal red giants and moderate barium stars, and its higher abundance of s-process elements (compared to these last two groups) could be due to its age and low metallicity. Therefore, we conclude that the stars classified as classical barium stars for which no orbital periods have been determined are probably a heterogeneous group, containing both wide binary systems with white-dwarf companions (i.e., genuine classical barium stars) and some low-metallicity single stars (i.e., which actually belong to the group of normal and moderate barium stars, whose overabundances of s-process elements are due to their evolutionary phase and metallicity).

Thus, we should probably conclude more generally that several factors must be taken into account to explain the phenomenon of classical barium stars and the overabundances of s-process elements in their atmospheres: their evolutionary phase, binarity, and metallicity. Each of these factors can make either a large or a small contribution in individual stars.

5. CONCLUSIONS

Our comparison of the atmospheric elemental abundances of normal red giants, moderate barium stars, and classical barium stars has shown the following.

(1) The overabundances of Na, Al, Mg, and Si found in classical barium stars are in a good agreement with the relation between overabundance and metallicity derived earlier for normal giants, supergiants, and moderate barium stars (Figs. 3–6). This testifies to a common nature for the abundance excesses, independent of whether the stars are single or binary. Namely, the overabundances are due to hydrogen burning in the stellar cores via the NeNa and MgAl cycles during the main-sequence stage, with the burning products subsequently dredged up to the star's atmosphere as a result of convection developing when the star becomes a red giant.

(2) The moderate and classical barium stars have different natures.

—Binarity is not a necessary condition for a star to display the signatures of a moderate barium star. We confirm that the enrichment of the stellar atmospheres with rare earth elements can already occur in the red-giant stage. Normal red giants and moderate barium stars are essentially the same type of object: single red giants at different stages of their evolution. We demonstrated that they all display relatively small (up to 0.3 dex) overabundances of s-process element. In addition, the abundance excesses depend, to some extent, on the evolutionary phase and the star's metallicity and mass. The fact that some of these stars have been shown to be binary does not affect our conclusion about the origin of their overabundances of s-process elements, since their companions are normal low-mass stars that are not capable of donating s-process elements to the giant's atmosphere.

—A necessary condition for the manifestation of the barium-star phenomenon is the presence of a fairly wide binary system whose components have considerably different masses, so that the rates of evolution of the components are very different. The more massive star evolves rapidly, enters the AGB phase, and ejects its envelope, "contaminating" its companion's atmosphere with matter rich in s-process elements. Binaries whose components have more similar masses will evolve at similar rates, and the barium-star phenomenon will not occur. An example is provided by the two moderate barium stars with long orbital periods studied in this paper. Stars with various metallicities (i.e., various ages) can become classical barium stars, provided the two components have sufficiently different masses. We confirm the dependence of the overabundance of s-process elements on the orbital period in binary systems.

(3) The overabundances of the s-process elements are determined by several parameters: binarity, mass, metallicity, and evolutionary phase. Any of these can be important for individual objects. However, a considerable influence by other parameters is also not excluded.

ACKNOWLEDGMENTS

This study was partially supported by the Russian Foundation for Basic Research (project no. 03-02-17336), the Program of Support for Leading Scientific Schools (grant NSh-162.2003.02), the Program "Nonstationary Processes in Astrophysics" of the Presidium of the Russian Academy of Sciences, and the Federal Scientific and Technological Program "Astronomy" (section 1102).

REFERENCES

1. L. I. Antipova, A. A. Boyarchuk, Yu. V. Pakhomov, and V. E. Panchyuk, Astron. Zh. **80**, 704 (2003) [Astron. Rep. **47**, 648 (2003)].
2. A. A. Boyarchyuk, L. I. Antipova, M. E. Boyarchuk, and I. S. Savanov, Astron. Zh. **78**, 349 (2001) [Astron. Rep. **45**, 301 (2001)].
3. A. A. Boyarchyuk, Yu. V. Pakhomov, L. I. Antipova, and M. E. Boyarchyuk, Astron. Zh. **79**, 909 (2002) [Astron. Rep. **46**, 819 (2002)].
4. V. E. Panchyuk, V. G. Klochkova, and I. D. Najdenov, Preprint Spets. Astrofiz. Obs. **135** (1999).
5. V. E. Panchyuk, N. E. Piskunov, and V. G. Klochkova, Preprint Spets. Astrofiz. Obs. **169** (2002).
6. R. D. McClure, Astrophys. J. **268**, 264 (1983).
7. R. D. McClure and A. W. Woodsworth, Astrophys. J. **352**, 709 (1990).
8. S. Udry, A. Jorissen, M. Mayor, and S. Van Eck, Astron. Astrophys., Suppl. Ser. **131**, 25 (1998).
9. S. Udry, M. Mayor, S. Van Eck, *et al.*, Astron. Astrophys., Suppl. Ser. **131**, 43 (1998).
10. A. Jorissen, S. Van Eck, M. Mayor, and S. Udry, Astron. Astrophys. **332**, 877 (1998).
11. R. L. Kurucz, Rev. Mex. Astron. Astrofis. **23**, 181 (1992).
12. E. Watanabe, M. Yutani, and Yamashita, Publ. Natl. Astron. Obs. Jpn. **3**, 1 (1993).
13. J.-C. Mermilliod, *Catalogue of Eggen's UBV Data* (1986).
14. E. J. Mannery and G. Wallerstein, Astron. J. **75**, 169 (1970).
15. P. A. Jennens and H. L. Helfer, Mon. Not. R. Astron. Soc. **172**, 667 (1975).
16. *The Hipparcos and Tycho Catalogues,* ESA SP-1200 (1997).
17. T. Lejeune, F. Cuisinier, and R. Buser, Astron. Astrophys., Suppl. Ser. **130**, 65 (1998).
18. A. A. Boyarchuk, L. I. Antipova, M. E. Boyarchuk, and I. S. Savanov, Astron. Zh. **75**, 586 (1998).
19. G. Schaller, D. Schaerer, G. Meynet, and A. Maeder, Astron. Astrophys., Suppl. Ser. **96**, 269 (1992).
20. D. Schaerer, G. Meynet, A. Maeder, and G. Schaller, Astron. Astrophys., Suppl. Ser. **98**, 523 (1993).
21. P. K. Lu, Astron. J. **101**, 2229 (1991).
22. B. E. Reddy, J. Tomkin, D. L. Lambert, and C. Allende Prieto, Mon. Not. R. Astron. Soc. **340**, 304 (2003).
23. A. A. Boyarchuk and L. S. Lyubimkov, Izv. Krym. Astrofiz. Obs. **64**, 3 (1981).
24. A. A. Boyarchuk and L. S. Lyubimkov, Izv. Krym. Astrofiz. Obs. **66**, 130 (1983).
25. P. A. Denisenkov and V. V. Ivanov, Pis'ma Astron. Zh. **13**, 520 (1987) [Sov. Astron. Lett. **13**, 214 (1987)].
26. R. D. McClure, *Cool Stars with Excesses of Heavy Elements* (Reidel, Dordrecht, 1985), p. 315.
27. R. M. Cavallo, A. V. Sweigart, and R. A. Bell, Astrophys. J. Lett. **464**, L79 (1996).
28. R. M. Cavallo, A. V. Sweigart, and R. A. Bell, Astrophys. J. **492**, 575 (1998).
29. L. Zacs, Astron. Astrophys. **283**, 937 (1994).
30. M. Busso, R. Gallino, D. L. Lambert, *et al.*, Astrophys. J. **557**, 802 (2001).
31. H. M. J. Boffin, N. Cerf, and G. Paulus, Astron. Astrophys. **271**, 125 (1993).
32. D. Hoffleit, *The Bright Star Catalogue* (1964).
33. E. Boehm-Vitense, Astrophys. J. Lett. **239**, L79 (1980).
34. A. P. Cowley and C. R. Cowley, Publ. Astron. Soc. Pac. **74**, 79 (1962).
35. A. M. Boesgaard, Astrophys. J. **161**, 163 (1970).
36. R. B. Culver and P. A. Ianna, Publ. Astron. Soc. Pac. **88**, 41 (1976).

Translated by N. Samus'